Understanding the coronary vasculature after myocardial infarction and engineering thick vascularized patches towards cardiac repair

Nicole Ashley Zeinstra

A dissertation

submitted in partial fulfillment of the

requirements for the degree of:

Doctor of Philosophy

University of Washington

2022

Reading Committee:

Ying Zheng, Chair

Charles Murry

Michael Regnier

Program Authorized to Offer Degree:

Bioengineering

University of Washington

Abstract

Understanding the coronary vasculature after myocardial infarction and engineering thick vascularized patches towards cardiac repair

Nicole Ashley Zeinstra

Chair of the Supervisory Committee:
Ying Zheng, Ph.D., Associate Professor
Department of Bioengineering

Implantable engineered cardiac patches have emerged as a promising approach to improve heart function after myocardial infarction. However, inadequate vascularization has prevented the generation and application of large-scale cardiac tissues. Improved methods for engineering perfusable, three-dimensional vasculature are therefore needed to support tissue survival prior to implantation as well as promote rapid host vascular integration post-implantation. The following dissertation reports advances in vascularization of implantable tissues and tools for assessing perfusion in the coronary vasculature. Here, we first established non-invasive, depth-resolved optical coherence tomography-based imaging tools to assess vascular structure and perfusion dynamics of the coronary vasculature and to visualize the fiber orientation of the heart, comparing

healthy and infarcted *ex vivo* fixed rat hearts to demonstrate the capabilities of this imaging platform. We utilized optical microangiography (OMAG) to create three-dimensional maps of the microvasculature and developed an automated processing framework to quantify differences between the vascular morphology of healthy and infarcted hearts. We further utilized OMAG-based velocimetry (OMAG-V) to characterize perfusion and polarization sensitive optical coherence tomography (PSOCT) to visualized fiber orientation within healthy and infarcted tissue. These studies demonstrate the ability of optical coherence tomography-based tools to quantitatively assess remodeling in the heart after infarction without need for tissue processing. The established platform can further be utilized to aid in development of cardiac therapies, including assessing perfusion of implanted cardiac patches. Next, we generated engineered tissues containing perfusable, endothelialized microvessels in a collagen matrix for application in cardiac repair. We created stem cell-derived endothelial cell-lined microvessels with planar geometry and found that these tissues are angiogenic, minimally thrombogenic when perfused with blood, and have gene expression associated with vascular and tissue development. We additionally generated cardiac tissues with perfusable microvessels and showed that when implanted onto infarcted rat hearts, the perfusable microvessel grafts integrate with the coronary vasculature to a greater degree and have higher cardiomyocyte density than non-perfusable self-assembled constructs at 5 days post-implantation. Towards generation of large-scale tissues, we further adapted this platform to engineer thick, perfusable, highly vascularized constructs by stacking multiple layers of patterned collagen membranes, creating a three-dimensional vascular network within the collagen matrix. We combined confocal microscopy, scanning electron microscopy,

optical microangiography, and transcriptional profiling to present the *in vitro* structure and perfusion of the thick vascularized networks. We then implanted these tissues onto infarcted rat hearts and found that multilayer grafts had greater *in vivo* perfusion and perfused vascular density than non-perfusable self-assembled controls at 5-days post-implantation as indicated by optical microangiography and histological analysis. Together, these data suggest the feasibility of generating large-scale cardiac tissues that achieve timely perfusion upon implantation. This work introduces critical advances in vascular imaging and tissue vascularization, facilitating progress towards therapeutics for cardiac repair.

Table of Contents

List of Figures

Acknowledgements

This dissertation, like all others, was a team effort. Thank you to my boyfriend Benji, our dog Curie, my family, my friends, my labmates, and my advisors for supporting me throughout this six year journey.

Chapter 1. Motivation and Specific Aims

1.1 Research Motivation

Coronary heart disease is the most common type of heart disease and leading cause of death in the United States. Heart attacks, or myocardial infarctions, occur when there is a blockage in the coronary vasculature and cause death of millions of cardiomyocytes due to lack of blood flow. Although most people survive the initial insult of a myocardial infarction, the myocardial infarction triggers a deleterious remodeling process. Tissue engineering has emerged as a promising approach for generating implantable cardiac patches that could regenerate the heart. The goal of this work is to establish tools for understanding vascular and structural remodeling after myocardial infarction and to engineer thick vascularized patches towards cardiac repair. This will be achieved through the following aims:

1.2 Specific Aims

1.2.1 Aim 1: Establish optical coherence tomography-based tools to understand differences between healthy and infarcted hearts

Significance: The ability to assess vascular and structural remodeling is key to understanding the effects of myocardial infarction and developing potential therapies. Yet current imaging techniques are limited in their ability to study the heart at high resolution without need for extensive tissue processing. Further, current tools for imaging the coronary vasculature only provide structural information for small vessels and cannot assess perfusion dynamics for a large

range of vessel sizes. Non-invasive imaging tools are therefore needed to better study vascular and structural remodeling in the heart.

Hypothesis: Non-invasive optical coherence tomography (OCT)-based tools, specifically optical microangiography (OMAG), optical microangiography-based velocimetry (OMAG-V), and polarization sensitive OCT (PSOCT), can be used to detect differences in vascular and fibrous structure between healthy and infarcted hearts.

Approach: Hearts from rats that underwent an ischemia/reperfusion surgery to create a myocardial infarction will be harvested at 28 days post-infarction and fixed with retrograde perfusion to preserve vasculature. Additionally, healthy hearts will be similarly harvested and fixed. Hearts will be imaged using OMAG to compare vascular structure, OMAG-V to compare perfusion dynamics, and PS-OCT to compare fiber orientation.

1.2.2 Aim 2: Investigate the role of patterned, perfusable vascular networks for engineering implantable cardiac tissues

Significance: Adequate vascularization and tissue perfusion are necessary for engineering thick cardiac patches for treatment of myocardial infarction. However, most cardiac patch platforms generate tissues that are not perfusable and heavily rely on self-assembly of endothelial networks when vessels are present. Our group has previously demonstrated that perfusable patterning improves host vascular integration of tissues containing only endothelial cells when implanted onto infarcted rat hearts. It remains unclear how these tissues promote host vascular

integration and whether the perfusable patterning could support cardiomyocyte engraftment.

Hypothesis: Patterned, perfusable vasculature can be engineered to enhance survival of cardiac tissues implanted onto infarcted rat hearts.

Approach: Patterned, perfusable microvessels will be constructed using a soft lithography approach then seeded with stem cell derived endothelial cells (hPSC-ECs) to create a perfusable network for patent endothelialized lumens. Perfusability, thrombogenicity, bulk cell viability, gene expression and endothelial cell flow sensitivity will be assessed. Cardiomyocytes will be incorporated into tissues with and without perfusable vasculature and implanted onto infarcted rat hearts. Host vascular integration and cardiomyocyte engraftment will be compared between perfusable and non-perfusable cardiac grafts.

1.2.3 Aim 3: Engineer thick tissues with multilayer, perfusable vasculature

Significance: Generation of large-scale, highly cellularized tissues will depend on the ability to construct three-dimensional networks of perfusable vasculature. While many fabrication techniques have emerged for generating perfusable vasculatures, there is still difficulty in balancing complexity, scale, stiffness, and cell compatibility. As a result, perfusable tissues with high vascular density have not been achieved in a material suitable for cardiac engineering.

Hypothesis: A multilayer stacking approach can be used to generated highly vascularized, perfusable tissues within a matrix that allows for both structural integrity and tissue remodeling.

Approach: Thick, perfusable, highly vascularized tissues will be engineered by stacking multiple layers of patterned collagen pieces to create a large network of perfusable lumens. Following endothelialization and culture, the stability, ability to remodel, and perfusability of these tissues will be demonstrated. Tissues with perfusable, multilayer vasculature will be implanted onto infarcted rat hearts and host vascular integration and perfusion will be assessed by optical microangiography, lectin perfusion and histology.

Chapter 2. Introduction

2.1 Coronary Vasculature

The main function of the heart is to act as a pump, driving blood flow through the vasculature to transport oxygen, nutrients, and waste throughout the body. The heart performs this pumping function through simultaneous contraction of billions of contractile cells called cardiomyocytes[1]. To provide sufficient blood flow to support the body's needs, the heart beats at least once per second in a normal human[2]. Because of the frequency of this energy intensive activity, the heart is the most metabolically active organ in the body and requires its own vascular network called the coronary vasculature[3].

Blood enters the coronary vasculature through two main arteries, the left and right coronary arteries, which begin at the base of the aorta directly above the aortic valve[4]. These arteries run along the surface of the heart near the epicardium, branching multiple times to distribute the blood flow to different regions of the heart before branching into smaller arteries and arterioles that penetrate into the myocardium. The vascular network further branches into capillaries, with the vascularization being so extensive that nearly every cardiomyocyte is directly contacting a capillary[5]. The capillary network drains into venules then cardiac veins, which reenter the right atrium via the coronary sinus[4].

Perfusion through the vasculature is driven by the pressure gradient of cardiac contraction. During systole, the aortic pressure climbs from 80 mmHg to 120 mmHg, causing blood to eject from the heart[6]. The blood travels down a pressure gradient through the vasculature to the vena cava which has a pressure of <10 mmHg[7]. In most of the body, the blood flow in the arteries is greatest during systole with much of the

pulsatile perfusion dampened before reaching the capillaries[8]. However, flow rate in the coronary vasculature does not follow the same paradigm as the rest of the vasculature because the intramyocardial vasculature is compressed by the contracting myocardium[9]. During systole, the blood in the capillaries is rapidly forced into the coronary sinus or back into the epicardial vessels, preventing further blood flow. As a result, the flow rate in the coronary arteries is greatest at the beginning of diastole with a majority of the coronary perfusion occurring throughout diastole[10].

The main cell type of the coronary vasculature is endothelial cells, which form a thin, continuous layer on the inside of blood vessels. Interestingly, endothelial cells are the most abundant cell type in the heart, having ~50% more endothelial cells than cardiomyocytes[11]. Endothelial cells form a continuous layer by adhering to one another through junctional proteins including VE-cadherin[12]. This membrane acts as the critical, selectively permeable barrier between circulating blood and the rest of the tissue. Additionally, endothelial cells play critical roles in blood pressure control, blood clotting, and inflammation[13,14]. In the heart, cross talk between endothelial cells and cardiomyocytes is necessary for maintaining regular cardiac function[5]. Endothelial derived factors such as nitric oxide (NO), endothelin, neuregulin, and PDGF have been shown promote cardiomyocyte development, proliferation, survival, maturation, and force generation[15–19].

The coronary vasculature is formed during embryonic and neonatal development in mammals[20]. The first step in this process is origination of a vascular plexus comprising endothelial cells[21]. While the origins of endothelial cells have undergone much debate, recent lineage tracing studies provide critical evidence. The proepicardium was originally

thought to be a main contributor to the coronary vasculature, however, genetic fate mapping of inducible and constitutive epicardial markers indicated minimal contribution[22,23]. More recently, work by Red-Horse and others have indicated that cardiac endothelial cells arise from both the sinus venosus and the endocardium in mice[24–27]. Coronary arterial and venous endothelial cells are formed when endothelial cells from the sinus venosus sprout over then penetrate into the myocardium[24]. Additional endothelial cells near the inner wall of the myocardium arise through endocardial sprouting and when trabeculation and subsequent compaction of the myocardium cause entrapment of endocardial cells[25–27]. The newly formed endothelial cells remodel to create a connected endothelial network known as the vascular plexus under absence of flow[21]. The vessels near the aorta soon fuse with the aorta to create arteries while veins are formed by connecting to the coronary sinus[28,29]. This establishes flow through the early coronary vasculature, driving remodeling towards the hierarchical vasculature of the mature heart[30,31].

2.2 Myocardial Infarction

Causing the death of more than 17 million people every year, cardiovascular disease is the leading cause of death worldwide and is only projected to grow[32]. Coronary artery disease is the most common form of cardiovascular disease, causing approximately 60% of cardiovascular related death[33]. In coronary artery disease, a buildup of plaque forms in the arteries, restricting blood flow through the vasculature. These plaques can rupture, causing a thrombus to form at the site of rupture, subsequently blocking all blood flow to the downstream vasculature[34]. When this occurs

in a blood vessel in the heart, it is a myocardial infarction (MI), or heart attack. During a MI, up to 25% of the left ventricle's cardiomyocytes may be lost due to lack of nutrients and oxygen as well as buildup of metabolic waste like H^+ [35,36]. While the massive cardiomyocyte death is detrimental to cardiac function, the initial insult is greatly exacerbated by the heart's inability to regenerate and replace the lost cardiomyocytes. In the adult human heart, average cardiomyocyte renewal is approximately 0.5% per year[37]. Instead of regenerating, the heart undergoes fibrosis to create a rigid scar where the infarct occurred, increasing the stiffness of the heart wall, and further inhibiting contractile function[38,39]. Additional compensatory remodeling places increased stress on the heart, often leading to functional decline and eventually heart failure[38,40]. Besides whole heart transplantation, available treatment options can only slow the progression of disease and provide palliative care.

In addition to the structural and fibrotic remodeling, myocardial infarctions also cause microvascular injury and vascular remodeling. During prolonged ischemic events, endothelial cell will die due to lack of blood flow. But even when ischemia is brief, reperfusion of the vasculature causes irreversible damage including loss of vascular integrity, intramyocardial hemorrhage and even endothelial cell death[41]. This leads to near complete loss of the microvasculature in the infarcted region. The dying cardiomyocytes and endothelial cell secrete hypoxia-induced HIF1α and subsequently the proangiogenic molecule VEGF[42,43]. Additionally, inflammatory cells that migrate into the infarct produce proangiogenic CXCL12[44,45]. This causes new microvessels to form in the border zone through proliferation and to sprout into the infarcted region through angiogenesis[46]. Recent studies indicate that coronary endothelial cells, not epicardial

cells or endocardial cells, are the main contributor to this new vasculature[47]. As the angiogenic activity subsides, some of capillaries within the infarct will enlarge and undergo arterialization[46]. In mice, both angiogenesis and stabilization occur within 2-7 days of the ischemic event[46]. Fibroblasts upregulate antiangiogenic genes by day 7, which may partially explain the decrease in vascularization[48]. In humans, vascular ingrowth is most prominent between 1-2 weeks after myocardial infarction[49]. While a vascular network is then present within the scar, it is highly disorganized with tortuous vessels and less extensive compared to healthy myocardium[50]. In animal models, stimulation of additional angiogenesis has been shown to reduce scarring and adverse remodeling, suggesting a potential target for future therapeutics[51,52].

2.3 Regenerative Medicine and Cell Therapies for Cardiac Repair

The great need for treatment of myocardial infarction has created much interest in regenerating the heart. Many different potential approaches are being investigated to reduce the scar, remuscularize the heart, and promote positive remodeling[53]. Amongst these strategies, cell-based therapies have emerged as promising approach. As cell-based therapies are the focus of the work in this dissertation, progress in this field will be described after a brief review of other approaches.

There are currently four main areas of acellular cardiac regeneration research: stimulation of cardiomyocyte proliferation, nonmyocyte reprogramming, delivery of paracrine factors and modulation of the innate immune response. The first of these, cardiomyocyte proliferation, offers the potential to remuscularize the heart, replacing cardiomyocytes that were lost during infarction. Strategies in this area include

overexpression of cyclins or and modulation of Hippo signaling[54,55]. Gene therapies that induce cardiomyocyte proliferation *in vivo* have been shown to improve left ventricular function and reduce scar size in pigs[56,57]. However, inducing proliferation inherently introduces risk and will require finetuning of geographic and temporal control that may differ greatly from patient to patient. In fact, a study that used miRNA-199 to stimulate cardiomyocyte proliferation in pigs resulted in sudden cardiac death due to sarcoma formation[56]. Nonmyocyte reprogramming can similarly target remuscularization, but this approach focuses on converting resident nonmyocytes into cardiomyocytes instead of generating new cells. Fibroblasts have been commonly used as a target nonmyocyte population[53]. In 2010, Ieda et al. successfully demonstrated that neonatal murine cardiac fibroblasts could be transdifferentiated into cardiomyocytes by viral overexpression of Gata4, Mef2c and Tbx5[58]. Additionally, reprogramming or modulation of fibroblast phenotype can reduce scar formation and may provide benefit to the healing process[59]. However, it should be noted that reprogramming is highly inefficient, limiting its potential application. While reprogramming has proven to have some benefit in mice and other small mammals, this approach will likely be more challenging in the aged adult human heart as it has been demonstrated that adult human fibroblasts are significantly more difficult to reprogram[60].

In comparison to remuscularization, other approaches seek to promote positive remodeling and healing within the infarct. Researchers have demonstrated the ability of numerous cytokines, such as vascular endothelial growth factor (VEGF) and basic fibroblast growth factor (bFGF), to induce angiogenesis and promote cardiac repair after myocardial infarction[51,52]. Addition studies show that exosome that package many

important molecules may stimulate cardiac repair[61–63]. A study by Liu et al. demonstrated that exosomes from stem cell derived cardiomyocytes improve cardiac function and reduce scar size in mice[61]. Despite these promising preclinical results, early clinical trials using paracrine factors did not yield positive results[64,65]. Instead of indicating that paracrine factors are ineffective, this may highlight the importance of appropriate dosing and the need for sustained infusion. In response, a large field has emerged, focusing on approaches for sustained release through engineering of biomaterials for hydrogel and nanoparticle applications[66]. As an alternative approach, a recent study has revealed the innate immune response may play a critical role in productive remodeling. In this study, Vagnozzi et al. showed that recruitment of CCR2+ and CX3CR1+ macrophages to the site of injury caused functional improvement and reduced fibrosis via acute inflammatory-based wound healing response, shedding light on a potential new approach for stimulating cardiac regeneration[67].

In addition to acellular approaches, cell-based therapies have emerged as a promising treatment for myocardial infarction. Endogenous cells including bone marrow-derived cell, mesenchymal stem cells, cardiac progenitor cells (populations of resident adult cells that do not form cardiomyocytes), and endothelial progenitor cells have been investigated as therapeutics in clinical trials[68–70]. While results largely demonstrated the feasibility and safety of cell-based approaches, these cells only act through paracrine mechanisms[68–70]. Recently, developments in the field of stem cell research have greatly advanced the potential for cell-based therapies. In 2006, Shinya Yamanaka created the first induced pluripotent stem cells from somatic cells by introducing four transcription factors: Oct4, Sox2, Klf4, and cMyc[71]. Researchers have since developed many

strategies for guiding efficient differentiation of these stem cells into many different cell types including cardiomyocytes, epicardial cells, and endothelial cells[72–77]. It is worth noting that stem cell-derived cardiomyocytes are functionally immature compared to adult cardiomyocytes, and many efforts toward maturation are being pursued[78]. Yet with the potential to create cells with pluripotent capacity from individual patients, induced pluripotent stem cells have moved to the forefront of cell-based therapies and regenerative research. More recent efforts in genetic engineering have resulted in stealthy stem cells that can evade immune detection, making transplantation of "off the shelf" cellular therapies feasible[79]. For cardiac regeneration, stem cell-derived cardiomyocytes have the potential to directly remuscularize the heart after myocardial infarction. Researchers in the Murry lab at University of Washington used intramyocardial injection of stem cell-derived cardiomyocytes to remuscularize infarcted non-human primate hearts, leading to significant functional recovery[80,81]. Despite clear efficacy, direct cell injection currently has limitations related to immaturity of stem cell-derived cardiomyocytes, arrhythmia, and poor engraftment of implanted cells[82]. As an alternative approach, tissue engineered constructs containing stem cell-derived cardiomyocytes have been applied to the surface of the heart as a cardiac patch with promising results[83]. Despite remaining challenges in the application of cardiac patches including lack of electrical integration with the host myocardium, this method has the advantages allowing maturation and potentially improved cell engraftment[82].

2.4 Cardiac Tissue Engineering

Cardiac tissue engineering seeks to create three dimensional cardiac tissues through combination of cells, materials, engineering techniques and physical stimulus. By allowing for control of cell composition, matrix, and architecture, engineered tissues can be designed to mimic properties of the native myocardium[84]. Additional culture enables *in vitro* remodeling and tissue maturation, further allowing the tissues to more accurately resemble the heart[84]. To suit the function and demands of the tissue, many different biomaterials can be used in fabrication including natural materials like collagen, alginate, and fibrin or synthetic materials like poly(ethylene glycol)[85]. Consequently, engineered cardiac tissues have shown great promise in both *in vitro* applications in drug development and disease modeling as well as *in vivo* applications as a cardiac patch for heart regeneration.

The field of cardiac tissue engineering became well established with the advent of engineered heart tissues by Wolfram Zimmermann and Thomas Eschenhagen in 2001[86]. They created the first contracting engineered heart muscle by casting a ring of collagen matrix containing neonatal rat cardiomyocytes around two pillars. Since then, two-post engineered heart tissue systems using stem cell-derived cardiomyocytes have become a mainstay as they enable easy assessment of calcium handling, contractility, and force generation, making them well suited for disease modeling and drug development[87–89]. Using similar models, functional maturation of cardiomyocytes has been achieved within cardiac tissues. Compared to two-dimensional culture of cardiomyocytes, cardiomyocytes within three-dimensional engineered tissues have more mature electrical and metabolic function[90,91]. Additionally, incorporation of physical stimulus including

extended electrical stimulation and mechanical forces, have been shown to increase sarcomere length, positive force-frequency relationships, calcium storage and release capacity, T-tubulation and gene expression indicative of maturation[92–94]. Together, this demonstrates the benefit of replicating features of the native environment.

In addition to *in vitro* modeling, engineered heart tissues can be used as a therapeutic for myocardial infarction when implanted onto the epicardial surface of the heart. In 1999, Li et al. achieved the first successful implantation of engineered tissues containing cardiomyocytes[95]. They implanted collagen sponges seed with fetal rat cardiomyocytes onto cryoinjured hearts and found that cardiomyocytes survived 5 weeks after implantation. A decade later, Stevens et al. demonstrated the first macroscale scaffold-free cardiac tissues composed of stem cell-derived cardiomyocytes, showing both synchronous calcium activity indicative of proper electromechanical coupling *in vitro* and engraftment onto infarcted rat hearts[96,97]. Beyond engraftment, recent studies have demonstrated that implanted cardiac tissues can maintain their electrical coupling *in vivo*[98,99]. In Gerbin et al., scaffold-free cardiac tissues were implanted onto infarcted rat hearts and were found to maintain electrical function but were not electrically coupled to the host myocardium at 4-weeks post-implantation[100]. Similarly in Shadrin et al., the Bursac lab at Duke created cardiac tissues by encapsulating stem cell-derived cardiomyocytes in a fibrin matrix, and 3 weeks after implantation onto healthy rat hearts, patches were shown to have clear calcium transients propagating through the entire patch when stimulated[99]. Perhaps most importantly, numerous studies have demonstrated the functional benefit of cardiac patches[83]. Recently, Gao et al. implanted large scale cardiac patches onto infarcted pig hearts and demonstrated significant improvement in left

ventricular function, reduction in infarct size and reduced apoptosis without arrhythmia[83]. Additionally, they found that exosomes secreted form the patches promote cardiomyocyte proliferation, promote angiogenesis, and enhance cell survival both *in vitro* and *in vivo*. These data suggest paracrine signaling as a mechanism of action and demonstrate that electrical coupling to the host myocardium is not necessary for functional benefit and *in vivo* tissue maturation.

Despite great achievements in this area, the therapeutic potential of cardiac patches is hindered by one key element: inadequate vascularization. As discovered in Stevens et al., endothelial cells greatly enhance survival of implanted cardiac tissues[97]. Yet without perfusable vasculature, tissues must remain thin enough to be supported only by diffusion for *in vitro* culture and after *in vivo* implantation[101]. As such, it is critical that advances be made towards both *in vitro* and *in vivo* vascularization of implantable cardiac tissues.

2.5 Vascularizing Engineered Tissues

Adequate vascularization remains a critical challenge in engineering thick, large-scale cardiac tissues. Prior effects towards vascularization of implantable cardiac tissues have heavily relied on self-assembly of endothelial networks[83,97,102,103]. As discussed in Section 2.4, Stevens et al. demonstrated that endothelial cells will form vessel structures when randomly incorporated into a tissue with cardiomyocytes[97]. And upon implantation onto healthy rat hearts, human endothelial cells from the graft with anastomose with the host vasculature and become perfusable. Although the addition of endothelial cells provides important cues to improve maturation, tissue function, and engraftment, self-

assembled endothelial cell networks slowly and incompletely integrate with host vasculature, which is insufficient for supporting large tissues[102,104–106].

While random assembly of endothelial cells is still being utilized in implantable cardiac patches, additional approaches are being developed to improve vascular integration of grafted tissues. Many research groups have successfully incorporated growth factors into their engineered tissues to promote host vascular ingrowth upon implantation, but alternative methods for increasing vascularization also exist. In a seminal study by Baranski et al., *in vitro* vascular patterning was achieved by formation of collagen cords containing endothelial cells and subsequent encapsulation into a fibrin gel[107]. After implantation onto the parametrial fat pad, grafts with vascular cords were shown integrated with the host vasculature while maintaining their initial geometry, indicating that patterned endothelial cells can guide the host vascularization. Although these tissues have since been shown to transiently guide vasculature when implanted onto rat hearts with the initial patterned geometry entirely remodeled by 7 days, this approach may still provide important cues that result in increased vascular integration of cardiac patches[108]. Instead of patterning, another approach is the allow self-assembled endothelial networks to mature through prolonged *in vitro* culture prior to implantation or transient implantation onto a highly vascularized organ, such as the omentum[109,110]. Studies have indicated that these approaches increase graft-host vessel anastomosis, host vessel ingrowth into the graft, and graft perfusion[109,110]. Despite improving the outlook for vascular integration, these tissues share a common limiting feature: lack of perfusability. As a result, tissues that rely on these types of vascularization methods are constrained by diffusion limits, and *in vitro* culture of thick tissues cannot be supported.

To overcome this issue, recent efforts in vascular engineering have been made towards incorporating perfusable vasculatures into engineered tissues. Many of the first attempts heavily depended on remodeling of endothelial networks through angiogenesis and vasculogenesis[111–113]. For example, by simply perfusing media through a device that contained collagen matrix with randomly mixed endothelial cells, Hsu et al. created a perfusable network of endothelial cells that connected to the inlet and outlet by vascular remodeling[113]. Additional work showed that this system can be used to generate perfusable tissues containing human stem cell-derived cardiomyocytes[114]. Perfusion enabled self-assembly has further been used to vascularize stacked sheets of cardiomyocytes. In Sekine et al., perfusable cell sheets containing cardiomyocytes and endothelial cells were created by placing them on top of a perfusable vascular bed and allowing perfusion to drive anastomosis and vascular remodeling[115]. While these techniques result in perfusable vasculature, they require time to become perfusable and are therefore not well suited for generation of large tissues. Other approaches including sacrificial scaffolds and lithography have been used to create immediately perfusable tissues with controlled geometries[116,117]. In 2014, Vollert et al. demonstrated that perfusable engineered heart tissues could be made by embedding alginate fibers during fabrication[116]. Once the alginate fibers were dissolved, open lumens remained which were used to continuously perfuse the engineered heart tissues for three weeks. To generate a more complex vascular structure, Zhang et al. used lithography to fabricate the AngioChip, a stiff biodegradable scaffold with branching interconnected lumens[117]. The AngioChip can be seeded with endothelial cells and surrounded by matrix and parenchymal cells to create perfusable engineered tissues. Furthermore, the chips can

be stacked together to create a three-dimensional vascular network. Zhang et al. utilized this platform to create cardiac tissues that electrically coupled and survived implantation with direct anastomosis to a rat femoral vein. Despite the great accomplishments of the AngioChip, its clinical relevance is limited by its slow degradation and the inability of the vasculature to directly interact with the parenchymal cells.

More recently, 3D printing has become the focal point of tissue vascularization, and numerous 3D printing strategies have been employed to generate cardiac tissues. Skylar-Scott et al. used subtractive sacrificial writing into functional tissue (SWIFT) to generate vascularized cardiac tissues that beat synchronously after 7 days of culture[118]. In this technique, a sacrificial gelatin ink was 3D printed into a viscoelastic slurry of stem cell-derived cardiomyocyte organoids, collagen, and Matrigel. At physiological temperatures, the slurry crosslinks and the gelatin melts, resulting in the pattern that was once filled with gelatin becoming open, perfusable lumen. Another technique, freeform reversible embedding of suspended hydrogels (FRESH) has been used to generate heart models[119]. In this technique, chilled collagen containing cells is printing into an easily deformable gelatin support bath. Lee et al. used FRESH to print contractile models of a ventricle containing stem cell-derived cardiomyocytes as well as heart models that contained major blood vessels with lumens as small as 100 μm. Other methods including stereolithographic apparatus for tissue engineering (SLATE) and subtractive printing with selective laser sintering have been used to generate tissues with entangled vasculature, although not cardiac tissues to date[120,121]. Although 3D printing shows great promise for creating vascularized engineered tissues, a majority of the methods assemble tissues voxel by voxel, and perfusion through the tissue cannot occur until the entire tissue is

printed. Even tissues with simple vasculatures can be time consuming to create, leaving cells in a nutrient-deprived state for extended periods of time[122]. As a result, high vascular complexity and resolution, which inherently increase printing time, may be limited. Subtractive printing with selective laser sintering overcomes this challenge by printing a sacrificial material then encapsulating it in a cell-laden biomaterial[121]. However, this technique currently can only print vessels with diameters down to 300 μm, and further vascular complexity and lumen size reduction may be limited by the fragility of printed constructs[121]. These limitations of 3D printing warrant further investigation into other vascularization strategies.

Towards this end, the Zheng lab at University of Washington developed a technique using a combination of soft lithography and injection molding to create patterned microvessels with perfusable, endothelialized lumens surrounded in collagen[123,124]. In this approach, two pieces of collagen are sandwiched together within a housing device that contains an inlet and outlet for perfusion. One of the collagen pieces is patterned using soft lithography to create a negative grid pattern, leaving an open lumen network that connects to the inlet and outlet once assembled. Endothelial cells are subsequently perfused through the lumen network to form a patent endothelium. By using a collagen matrix, this platform can provide an appropriate biophysical, cellular, and biochemical microenvironment for cardiac tissues. The vasculature can remodel and the extraluminal space can be populated with cardiomyocytes and stromal cells that can directly contact the vasculature. Additionally, the simple fabrication does not require long wait times without media access to the center of the tissue, unlike many 3D printing methods. Using the microvessel platform, the Zheng lab has previously created

electrically coupled cardiac tissues with stem cell-derived cardiomyocytes and a perfusable vasculature of HUVECs[125]. They also engineered microvessels with stem cell-derived endothelial cells and found them to be an ideal cell source for tissue vascularization due to their stem cell origin and angiogenic nature[74,126]. They implanted these tissues onto infarcted rat hearts and found them to have better host vascular integration than similar tissues containing only self-assembled stem cell-derived endothelial cells after 5 days of implantation[126]. While this work demonstrates that perfusable patterning improve graft vascularization, it remains unknown unclear how this approach promotes host vascular integration and whether the perfusable patterning could support cardiomyocyte engraftment. Additionally, current methods of fabrication only produce a single layer of vasculature, yet a large, three-dimensional vascular network will be needed to support large scale cardiac tissues.

2.6 Heart Imaging Techniques

In parallel with developing therapies for myocardial infarction, it is crucial that tools for accurate assessment of structural and vascular remodeling and repair be established. In the clinic, imaging modalities including ultrasound, magnetic resonance imaging, x-rays, single-photon emission tomography, and positron emission tomography are used to assess perfusion within the myocardium[127]. While non-invasive, these techniques are limited by millimeter-scale resolution and therefore can only be used to study gross perfusion[128]. In the lab, post-mortem histological assessment is most commonly used to study the vasculature in the heart. Although histology is simple and can provide valuable information about tissue morphology, it is not an ideal technique for understanding

complex vascular networks because it is limited to 2D cross sections. Recently, researchers have been using light-based imaging techniques to study the coronary vasculature at higher resolution. Confocal microscopy and light sheet microscopy have been used to study collateral artery formation and capillary structure after myocardial infarction in mice. However, imaging penetration depth is severely limited without extensive tissue clearing, limiting these techniques to *ex vivo* applications[129–131]. Multiphoton microscopy has been used to visualize the coronary vasculature in live mice, however, extremely slow scanning speeds restrict the achievable field of view[132,133]. As such, acquiring large images of microvascular structure and perfusion can be challenging using traditional techniques.

As an alternative to these imaging techniques, optical coherence tomography-based angiography (OCTA) has emerged as a non-invasive tool for imaging blood flow down to the capillary level with millisecond-scale temporal resolution[134,135]. OCTA has achieved great success for diagnosis of ophthalmic diseases and is more recently being applied to study other tissues including the brain and the skin[136–140]. Methods like Eigen decomposition-based optical microangiography (ED-OMAG), which utilizes the optical backscattering of moving red-blood cells, have been used to produce depth-resolved maps of the microvascular [141–145]. Additional advances in processing algorithms now allow for collection of velocity data alongside structural data[146]. Recently, Qin et al. used OMAG to visualize the structure of the microvasculature of *ex vivo*, fixed rat hearts[126,147]. This technique has further been applied to assess host vascular integration of implanted tissues, revealing information about both vascular density and perfusion dynamics within tissue grafts. Yet to date, OCTA and OMAG have not been used to quantitatively detect

structural changes in the microvasculature of infarcted hearts, demonstrating the unfulfilled potential of OCT-based imaging tools to study myocardial infarction and methods for cardiac repair.

2.7 Summary

The coronary vasculature plays the critical role of transporting blood through the highly metabolic myocardium. During a myocardial infarction, a branch of the coronary vasculature becomes occluded, resulting in massive cardiomyocyte death followed by negative remodeling that can lead to heart failure. To address this clinical need, multiple approaches are being investigated to regenerate the heart after myocardial infarction. Amongst them, stem cell therapy has great potential. Implantable engineered cardiac tissues containing stem cell-derived cardiomyocytes have been shown to provide regenerative benefit after myocardial infarction, however, their size is limited by inadequate vascularization. Random incorporation or non-perfusable patterning of endothelial cells can improve graft vascular integration with the host after implantation, but tissues created using these techniques lack perfusion and are therefore still restricted by diffusion limits. While many approaches to generate thick tissues with perfusable vasculature have recently been developed, challenges remain in balancing appropriate material selection, length of fabrication time without perfusion, and potential for vascular complexity. In addition to current gaps in tissue fabrication, there is also a need for imaging techniques that can be used to assess microvascular structure and perfusion dynamics within the infarcted myocardium and implanted cardiac tissues. This

dissertation seeks to address these challenges in vascularization of implantable tissues and assessment of perfusion in the coronary vasculature.

Chapter 3. Establish optical coherence tomography-based tools to understand differences between healthy and infarcted hearts

Parts of this chapter have been published in the following manuscript:

> Peijun Tang… **Nicole Zeinstra**, et al. "Polarization sensitive optical coherence tomography with single input for imaging depth-resolved collagen organizations." *Nature Light: Science & Applications*, 2021[148].

3.1 Abstract

The ability to assess vascular and structural remodeling is key to understanding the effects of myocardial infarction and developing potential therapies. Optical coherency tomography has emerged as a powerful, noninvasive tool for imaging both vasculature morphology and perfusion dynamics as well as fiber orientation. Here, we utilize both optical microangiography, a depth-resolved, high-resolution angiographic imaging tool for visualizing microvascular structure and perfusion dynamics, and polarization-sensitive optical coherence tomography (PSOCT), a three-dimensional imaging tool for mapping fiber organization. First, we use a flexible probe-based swept-source optical coherence tomography (SS-OCT) system to image wide-field coronary microcirculation in *ex vivo* fixed healthy and infarcted rat hearts during retrograde perfusion through the coronary vasculature. An automated framework is presented for quantifying vessel morphologies from *en face* OMAG images, and differences in the disrupted microcirculation are shown

in infarcted hearts compared to the healthy ones. Various angiographic metrics are presented to quantify vascular patterns, including a Vessel Area Density (VAD) of capillary or arteriole/venule networks, Vessel Complexity Index (VCI), Vessel Tortuosity Index (VTI), and Flow Absent Zone (FAZ). These metrics provide insight into the disruption in local microvasculature morphology after infarction and have demonstrated consistency with the histological analysis. We further use OMAG-based velocimetry to assess average velocity and perfusion within the microvasculature. Additionally, we utilize PSOCT to visualize depth-resolved myocardial architecture via fiber orientation in both healthy and infarcted rat hearts. Overall, this work demonstrates that optical coherence tomography can be used as a robust tool to identify and study injury caused by myocardial infarction, providing new insights for cardiac research.

3.2 Introduction

Heart disease remains the leading cause of death worldwide[149,150]. A single myocardial infarction can lead to extensive remodeling in which the heart wall becomes thin and scarred, inhibiting contractile function[38,39]. Additional compensatory remodeling places increased stress on the heart, often leading to functional decline and eventually heart failure[38,40]. Because of the vascular disruption and capillary rarefication following myocardial infarction, post-ischemic recovery requires re-establishing coronary blood flow to restore nutrients and oxygen to the myocardium[151]. As a result of this great clinical need, efforts have been made to understand and enhance vascular remodeling of the coronary microcirculation after ischemic injury[130,131,151]. This revascularization process is known to include angiogenesis and arteriogenesis, which can cause significant structural

changes to vascular architecture and the surrounding myocardium[152,153]. However, due to its complex 3D hierarchical architecture with large ranges of diameters, lengths, and curvatures, the coronary microvasculature has been challenging to study. To date, there are no proper imaging techniques that can provide vascular morphology and perfusion dynamics in micro-scale over a large region of interest. Robust imaging methods are, therefore, needed to reveal changes in vascular structure at various scales, to provide important hemodynamic and perfusion information, and to visualize scar formation after acute myocardial infarction.

Ultrasound (US), magnetic resonance imaging (MRI), single-photon emission tomography (SPECT), and positron emission tomography (PET) techniques are the foremost non-invasive imaging tools for clinical diagnosis of myocardial infarction[127]. These techniques either visualize coronary structure or measure myocardial perfusion to diagnose and detect ischemic events within the heart. However, these techniques have relatively low spatial (mm scale) and temporal (multiple seconds) resolution, which limits their utility in studies on coronary microvasculature[128]. Light-based imaging techniques such as confocal microscopy, light sheet microscopy, and multi-photon microscopy allow for 3D visualization of microvasculature with magnified resolution (0.3~1μm) yet have numerous drawbacks. Confocal microscopy and light-sheet microscopy have limited tissue penetration depth without the use of complex tissue clearing protocols, while multiphoton microscopy is limited by scanning speed[129,154,155]. Also, these methods can only be used to visualize vascular structure and provide no information on perfusion dynamics. As such, acquiring localized images of functional microvasculature in-depth can be challenging using traditional imaging techniques.

Optical coherence tomography-based angiography (OCTA) has emerged as a non-invasive, nonionizing, *in vivo* imaging tool capable of producing blood flow images with micron-scale spatial and millisecond-scale temporal resolution[134,135]. While OCTA was developed for and is primarily used in ophthalmic applications, recent efforts have shown that it could be a valuable tool to study biological processes across many types of tissue, thanks to its attributes of fast imaging speed (>200 kHz), ease of use, relatively wide field of view (centimeter scale), and high resolution (μm-order)[136–140]. Eigen decomposition-based optical microangiography (ED-OMAG) has been shown to be capable of depth-resolved mapping of microvascular patterns and coronary hemodynamics using intrinsic dynamic scattering signals, such as flowing red blood cells, at the capillary level[141–145].

Previously, we have used ED-OMAG to visualize the coronary microvasculature of *ex vivo* fixed healthy rat hearts[147,156]. In our previous study, we perfused Intralipid into the coronary vasculature via retrograde perfusion through the aorta. When imaging the heart, perfusion of Intralipid as an intravascular contrasting agent can enhance the contrast of the ED-OMAG angiogram at greater depths. Compared to blood, Intralipid can increase lumen signal and suppress tailing artifacts resulting from red blood cell orientation and multiple scattering. As demonstrated by our study with *ex vivo* fixed healthy rat hearts, non-contact OCTA provides a method to visualize and quantify vascular morphology in the heart.

Another OCT-based imaging tool, polarization-sensitive optical coherence tomography (PSOCT), has also emerged as a promising technique for noninvasive 3D mapping of birefringent material[157–160]. Since fibrous collagen is highly birefringent,

PSOCT can contrast collagen structure with a wide FOV (from a few to tens of square centimeters), relatively deep imaging depth (up to ~2 mm) and fast imaging speed (seconds per 3D scan)[161–164]. While the native myocardium has a highly aligned fiber orientation, the collagenous scar located in infarcted tissue does not, indicating that PSOCT could be a powerful tool to study differences between healthy and infarcted heart tissue[165].

In this work, we used optical coherence tomography (OCT)-based imaging techniques to assess the vascular and structural differences between healthy and infarcted *ex vivo* fixed rat hearts. First, we used depth-resolved 3D Eigen-decomposition-based optical microangiography (ED-OMAG) to visualize the coronary microvascular structure down to the capillary level during retrograde perfusion. To acquire wide-field OCT angiography images of the coronary vasculature, we utilize a flexible probe-based swept-source optical coherence tomography (SS-OCT) system. We further present an automated framework for image processing and establish several quantitative metrics related to vessel morphology and structure to provide a quantitative comparison between three distinct conditions: healthy, infarct, and remote. Specifically, we use vessel area density (VAD), vessel complexity index (VCI), vessel tortuosity index (VTI), and flow absent zone (FAZ) to quantitatively show morphological differences in microcirculation between infarcted and non-infarcted regions. We next apply OMAG-based velocimetry to reveal differences in perfusion dynamics in both the capillary bed and the whole vasculature. Further, we demonstrated consistency between OMAG imaging and histological analysis. Additionally, we utilize polarization sensitive OCT (PS-OCT) to visualize fiber disorganization in the scar of infarcted rat hearts from birefringent

properties. To date, no other OCT studies have researched changes in micro-scale morphological and perfusion changes in the coronary microvasculature or architectural fiber disarray induced by infarction. Thus, our work demonstrates the practicality of using non-invasive OCT-based imaging study differences in coronary microvasculature and architecture in healthy and diseased hearts.

3.3 Scientific Methods

3.3.1 Heart preparation

All animal procedures were approved by the University of Washington Institutional Animal Care and Use Committee (IACUC, protocol #2225-04) and performed in accordance with US NIH Policy on Humane Care and Use of Laboratory Animals.

In this study, 8-week old male Sprague-Dawley rats (approximately 250-300 g, n=6) were randomly chosen to undergo a surgery to induce a myocardial infarction as previousl[126]y described. Briefly, rats were anesthetized, intubated, and mechanically ventilated. The heart was exposed via a thoracotomy, then the left anterior descending coronary artery (LAD) was temporarily occluded for 60 minutes to cause ischemia by throwing a suture around the LAD and tying the suture around flexible tubing. At 60 minutes, the artery was reperfused by cutting the suture. For anesthesia, two intraperitoneal injections of 68.2 mg/kg ketamine and 4.4 mg/kg xylazine were given, one before the surgery and another after ischemia is induced. To provide analgesia following the surgery, 1 mg/kg sustained-release burprenorphine was used.

The group of infarcted hearts was harvested four weeks after the ischemia/reperfusion surgery, along with n=6 hearts from an age-matched control group

that did not undergo surgery prior to tissue harvest. For euthanasia, an intraperitoneal injection of 1.5 mL Euthasol was administered. Once the rats were no longer breathing and were not responsive to a toe pinch, the heart was exposed by opening the chest. Before removing the heart, two solutions were circulated through the heart by injecting the solutions into the inferior vena cava while the heart was still beating. First, 50 U heparin was injected to prevent thrombosis then supersaturated potassium chloride was injected to arrest the heart in diastole. After excision, a blunt tip needle was used to cannulate the aorta and allow for retrograde perfusion. Then, the heart was perfused with PBS containing 4 mg/L Papaverin and 1 g/L adenosine to dilute the vasculature. Immediately following, the heart was perfused with 4% paraformaldehyde at a constant pressure of 100 mm Hg for 10 minutes. The hearts were further fixed in 4% paraformaldehyde overnight before being rinse with and stored in PBS until imaging.

During imaging, 10% Intralipid (by volume, diluted in PBS) was perfused through the coronary vasculature via retrograde perfusion through the cannulated aorta to provide a light-scattering contrast mechanism[147]. The Intralipid in the heart was allowed to flow under a stable pressure (100 mmHg) for 10 minutes prior to imaging to ensure microvascular perfusion and the pressure was maintained at 100 mmHg throughout the imaging process. A 50 µL drop of glycerol was applied to the surface of the tissue 10 minutes prior to imaging as an optical clearing agent[166,167]. During imaging, each sample was fixed in the center of a Petri dish using a 3-D printed mount to prevent sample motion (**Figure 3.1A**).

3.3.2 Swept-source coherence tomography imaging for OMAG

A handheld probe-based swept-source OCT (SS-OCT) imaging system that provided flexible focus alignment was used in this study and has been described in detail elsewhere[168]. Briefly, the system used a vertical-cavity surface-emitting (VCSEL) swept laser source (SL1310V1-10048, Thorlabs Inc., Newton, NJ) with an A-scan speed of 200 kHz, the central wavelength of 1310 nm, and a spectral bandwidth of 100 nm, providing an axial resolution of ~10 μm. The imaging probe utilized a 5x objective lens (LSM03, Thorlabs Inc., NJ, USA) delivering a lateral resolution of ~20 μm and a focal depth of ~130 μm (defined by the Rayleigh length). The sample arm included a handheld probe with a built-in camera to provide a concurrent white-light image co-aligned with the OCT field of view (FOV). The handheld probe was fixed on a stable support stand with 3-degrees of freedom to allow for crude and refined (micron-level) alignment and the sample arm's focus during imaging.

For the infarcted hearts, four regions of interest within the infarct near the left anterior descending coronary artery and four remote regions on the posterior side of the heart were selected and scanned. For the healthy hearts, four regions were selected and scanned in the same areas that correspond to the infarct and remote regions of the infarcted hearts. Each session consisted of a co-aligned wide-field (12 mm × 12 mm) white light image followed by a 4 mm × 4 mm x1mm OCT 3D scan (**Figure 3.1B**). The wide-field white-light image from each scan session provided anatomical markers used to verify regions for comparison of OCTA images between groups.

In all acquisitions, a B-M mode scanning protocol was performed where 800 A-scans were acquired along the X-direction to compose a single B-scan and then repeated

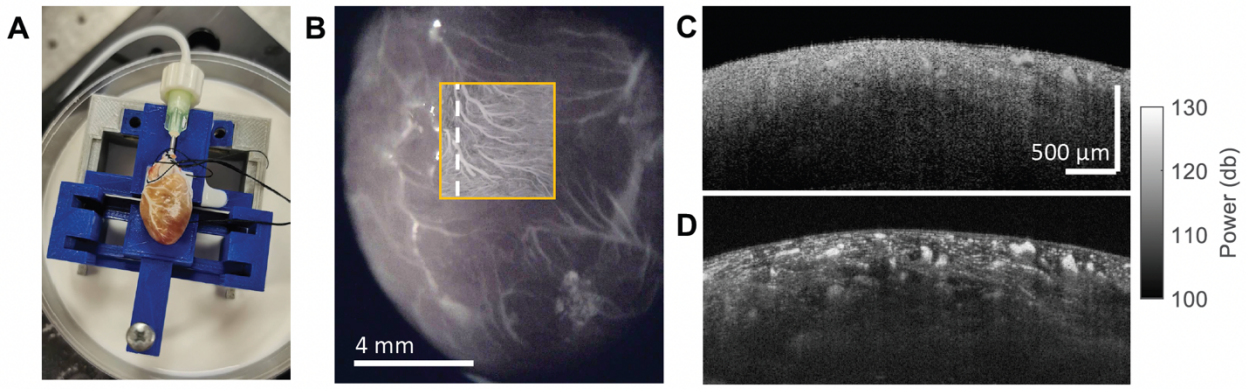

Figure 3.1 Experimental setup for OCT imaging of rat hearts. (A) Rat hearts during imaging with retrograde perfusion of Intralipid and fixed to 3D printed mount. (B) Representative white light image with embedded OMAG *en face* image. Scale bar, 4 mm. (C,D) Cross-section image of (C) OMAG blood flow and (D) OCT structure from the dotted line in (B). Scale bar, 500 µm.

at the same Y-location to create an M-scan at 200 fps. Eight repeat B-scans were taken at each location to facilitate the reconstruction of ED-OMAG microvascular and OCT structural images, 800 B-scan locations produced a C-scan along the Y-direction. Each OCT scan took ~26 seconds to acquire[135,145].

The mean OCT intensity signal was taken along the 8-repeated B-frames and then log-compressed to reconstruct tissue structure along the depth direction based on light scattering (**Figure 3.1C**). Because of scattering and absorption in the cardiac wall, the light was nearly attenuated to below the noise-floor at depths greater than 400 µm in all samples.

Temporal changes across the eight repeated B-scans were used to reconstruct vascular structures using the ED-based OMAG technique to create OCT-angiography (OCTA) intensity signals (**Figure 3.1D**)[145]. The OCTA image had a background noise of around 85 dB measured in air. Due to the uneven surface of the heart, the lens confocal function resulted in slight differences in illumination, which reduced the maximum OMAG intensity signal near the edge of each scan. To correct this, the intensity signal in the 3D

volume was normalized with the ratio of the sum of a reference signal from a saturated OMAG value (i.e., 130 dB) to the sum of the intensity signal from the whole volume.

Using another imaging protocol with the same experimental setup and imaging system, optical microangiography-based velocimetry (OMAG-V) data were collected. The data were collected by repeating each B-scan for ten times before switching to the following B-scan location until the whole volume was collected. In the fast axis, each B-scan is composed of 150 A-scans and 150 B-scans. A total of 1.5 mm x 1.5 mm will be covered with this scanning protocol. Temporal changes across the repeated B-scans were used to reconstruct vascular structures and produce velocity data using ED-based OMAG as previously described[146].

3.3.3 *Vascular quantification*

A semi-automated segmentation software was applied to the 3D OCT structural data to find the surface of the tissue[169]. The 3D vascular image was compressed to an en-face image using the maximum-intensity projection of vessels across a 50 μm (~10 pixels) slab thickness measured from the surface of the tissue. The projection image provided abundant morphological details of the microvasculature tree. Depth-resolved mapping of microvasculature is shown using a pseudo-color-coded projection image, where dense capillary networks can be seen within superficial tissue regions (colored in orange) and larger vessels penetrating the myocardium (colored in blue). A dense capillary bed could be well-resolved across different depths. Although OCT beam defocusing on vessels below this depth is possible, the relatively small axial range ensures most vessels remain within or close to the focal plane of the focusing lens and

provides consistent SNR and lateral resolution between scans[147]. To avoid vascular projection artifacts intrinsic in the OCTA, a validated projection artifact removal algorithm was used to minimize these artifacts from deeper myocardium layers[170].

This study used five structural metrics: vessel area density (VAD) of capillary or arteriole/venule networks, vessel complexity index (VCI), vessel tortuosity index (VTI), and flow absence zone (FAZ) to quantify vessel structures based on an automated processing scheme that was clinically validated in ophthalmic imaging (**Figure 3.2**)[171–173].

A binary image of the vasculature for vessels with diameters greater than 20 μm (binarized larger vessel map) was obtained using a combination of Otsu's thresholding method and hessian-based Frangi vesselness filtering[174]. The Frangi-based hessian filtering elements isolated all structures with a diameter greater than 20 μm (4 pixels). After normalization, the intensity signal in the filtered OCTA projection was scaled evenly to ten threshold values based on Otsu's method using the built-in MATLAB command (MATLAB, R2018b, Mathworks, Boston, MA). A value slightly greater than the lowest gray-scale value (i.e., filtered noise-floor) was then used to binarize the hessian gray scale image, resulting in a binary projection image of all vessels greater than 20 μm in diameter.

The vessel area density of the capillaries (VAD_C) was calculated by binarizing the original OMAG vascular projection with global thresholding (105 dB cut-off) and adaptive thresholding. Then the binarized image was masked by the binarized larger vessel map described previously. As such, pixels occupied by vessels with a diameter greater than 20 μm were subtracted from the flow binary mask to generate a capillary binary map.

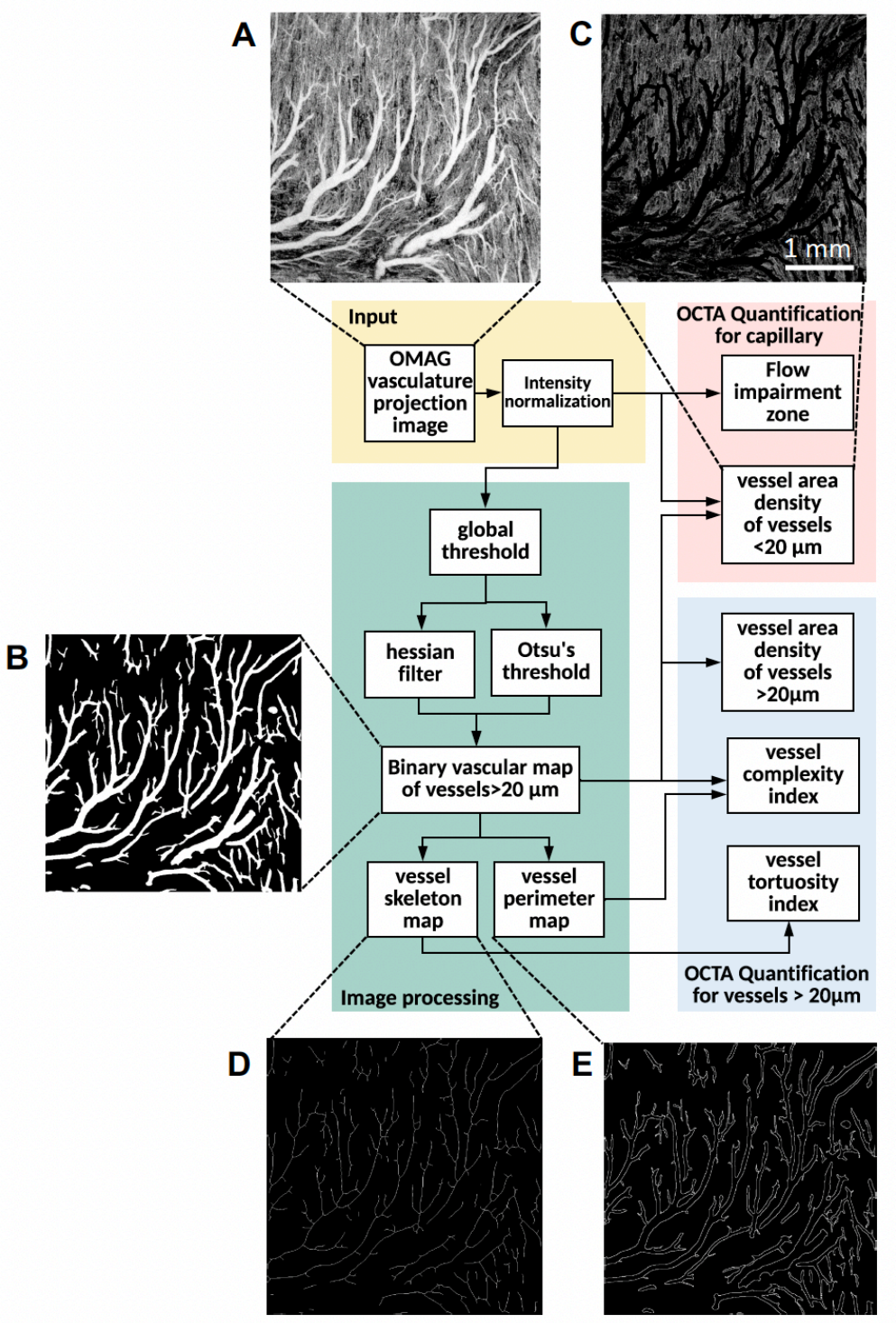

Figure 3.2 OMAG processing framework. A maximum intensity ED-OMAG projection image of each scan was used as the starting point to quantify vessel area density (VAD), vessel complexity index (VCI), vessel diameter index (VDI), vessel tortuosity index (VTI), and flow absent zone (FAZ). (A) OMAG vascular projection image. (B) Binary vascular map of vessels > 20 µm. (C) Binary vascular map of vessels < 20 µm. (D) Vessel skeleton map. (E) Vessel perimeter map. Scale bar, 1 mm.

The vessel area density was then calculated in each image for both large vessels (> 20 μm) and capillaries (< 20 μm) separately according to Eq 1.

$$\mathrm{VAD} = \frac{\sum_{ij=1}^{N} A_{ij}}{\sum_{ij=1}^{N} B_{ij}}, \qquad (1)$$

Where *i* and *j* represent the X- and Y- pixel locations, respectively, and *N* corresponds with the total number of B- and C-scans (800×800 pixels). *A* represents discrete pixels occupied by vessels in the binary image, and *B* represents all pixels in the OMAG scan.

Following VAD quantification, the vessel tortuosity index (VTI) was determined from the binary map of large vessels. First, a vessel-skeleton map was extracted from the binary vasculature image. The skeletonized vessel map was separated into multiple segments by each node and endpoints for VTI calculation. The skeletonization process and endpoints and branch point extraction were obtained with the built-in MATLAB 2019b function “bwmorph.” The VTI value was calculated using a simple arc to chord ratio method, where the length of the curve between two endpoints of vessel branches was divided by the length of the curvature of each vessel between subsequent nodes or endpoints[175]. The ‘arc’ to ‘chord’ ratio was quantified for each vessel segment separately. Finally, the global average VTI from all segments was calculated according to Eq. 2:

$$\mathrm{VTI} = \frac{\sum_{1}^{n} C_n}{\sum_{1}^{n} L_n}, \qquad (2)$$

Where *C* represents the local curve length of the n^{th} vessel segment between two endpoints (representing the arc length), and *L* represents the Euclidian distances between the ends of the n^{th} vessel branch using the discrete locations of each node or endpoint of the vessel in the X- and Y- coordinate space.

Next, the vessel complexity index (VCI) was quantified by the ratio of vessel perimeter to vessel area (Eq. 3).

$$\mathrm{VCI} = \frac{\left(\sum_{ij=1}^{N} P_{ij}\right)^2}{4\pi \sum_{ij=1}^{N} A_{ij}} \quad (3)$$

Using edge detection, vessel perimeter images were extracted from the binary vasculature image. Where *P* represents all pixels that correspond to the perimeter of each vessel greater than 20 μm. The VCI is a unitless index that provides an estimate of the perimetric complexity of the vessel organizations[176]. This method has been demonstrated to show complexity characteristics visually in retinal vasculatures[171].

Lastly, the OCTA projection image was used to calculate a flow absent zone (FAZ) value. Pixels without OCTA flow signal, *Q*, were used to calculate the total no-flow regions. As such, the FAZ was calculated as a percent area according to Eq. 4:

$$\mathrm{FAZ} = \frac{\sum_{\mathrm{ij}=1}^{\mathrm{N}} \mathrm{Q_{ij}}}{\sum_{\mathrm{ij}=1}^{\mathrm{N}} \mathrm{B_{ij}}} \quad (4)$$

Statistical analysis (ANOVA) was used to determine significance between groups.

A repeatability study was conducted to explore each metric's sensitivity to imaging and focusing variations using a series of scans from the same heart around similar regions. A small coefficient of variance (< 0.05) was determined for each metric when tested over multiple scans with overlapping FOV and slightly different focus positions. As such, quantitative metrics compared between samples and different imaging regions with coefficients of variances > 0.05 represent morphological changes independent of user setup.

For assessment of perfusion dynamics, velocity maps were created from the OMAG-V data as previously described[146]. The average velocity was quantified in all vessels. An index for relative perfusion was subsequently calculated according to Eq. 5:

$$\text{Relative perfusion} = \sum_{ij=1}^{N} V_{ij} \quad (5)$$

where *V* represents the velocity of an individual pixel. Statistical analysis (ANOVA) was used to determine significance between groups.

3.3.4 *Polarization sensitive optical coherence tomography imaging*

For polarization sensitive optical coherence tomography (PS-OCT), hearts were imaging using a 100-kHz MEMS-VCSEL swept laser source (SL1310V1-10048, Thorlabs), providing an output power of 25 mW with a central wavelength of 1310 nm and a spectral tuning range of 100 nm. The output of the light source was sent to a polarization controller and became linearly polarized through a polarization beam splitter, and then split into the reference and sample arms through a beam splitter at a split-ratio of 50:50.

The reference arm was installed with a quarter-wave plate, with its axis aligned at 22.5° with reference to the input polarization state, ensuring that the reflected light was coupled equally into the vertical and horizontal channels. The sample arm was equipped with a QWP aligned at 45° with respect to the input polarization state, resulting in a circularly polarized light incident at the sample surface. The light coming back from both the reference and sample arms were recombined and sent to PBS1 and PBS2, respectively, where the interference light was split into horizontal and vertical components. Balanced detection was used for both vertical and horizontal channels to collect the interference signals, upon which PS-OCT images are reconstructed. The PS-OCT system was controlled using a home-developed LabView (National Instruments) platform which provided flexibility to control scanning patterns based on the applications. The axial resolution was approximately 7.5 μm, in air.

The osculating plane was then determined based on discrete-differential geometry (DDG). he DDG analysis computes a set of 'TNB' orthonormal bases in 3D space where T is the tangent vector, N is the normal vector and B is the binormal vector of the spatial curve which are then used to determine the osculating plane (i.e., the plane that T and N vectors lie) at each point of the curve[177]. Since PSOCT is based on a round-trip measurement, the measured osculating plane is the apparent plane defined by the accumulated polarization rather than the actual osculating plane.

To retrieve local birefringent information using DDG analysis, a PSOCT-based polarization state transmission model that describes the polarization state evolution in a round-trip measurement was used. This model reveals the relation between local birefringent parameters and the evolution behaviors of the output polarization state in

PSOCT. Based on this relationship, the DDG-based PST method is combined with a set of 3D rotation operations to derive the local optic axis and phase retardation from the measurements.

To eliminate the effect of the depolarization, all the Stokes vectors of the output polarization states were normalized to 1 before calculating the local phase retardation and local axis orientation. The trajectory of the output polarization states in an A-scan at the Poincare sphere is considered as a spatial curve. DDG is applied to this curve to provide the TNB frame of the curve in an A-scan. By using a 3D rotation operation, then the local phase retardations and local axis orientation can be obtained.

Because the asymmetry of the optical path in the PSOCT system can cause an overall rotation of the plane that contains all possible optic axes, the vector An is a vector in 3D space. After the 3D vector An is computed, the effect of the asymmetry of the system can be identified as the V-components of all the 3D vectors An. Since the vertical (along z, or equivalently V on the Poincare sphere) component of the vector An is introduced by the imaging system and not sensitive to tissue structures, it should be removed. As such, the direction of the vector projected onto the QU-plane represents the relative axis orientation of the sample. Note that this is true when the plane of the possible optic axes rotated out of the QU-plane with an acute angle. When the plane of the possible optic axes rotated off the QU-plane with an obtuse angle, the plane of the possible optic axes will be flipped if directly project it into the QU-plane. Hence, a flip operation should be done before finding the absolute axis orientation. To obtain the absolute axis orientation of the sample, we calibrate the system by using a phantom with a known optic axis, and then define this axis as the reference direction (0). RGB colors are utilized to

code the local axis orientation for display. The projected vector is normalized to a unit vector. Red and green are utilized to code the x and y components of the unit vector that represent the optic axis. Because the V-component of An is introduced by the system, the color blue (representing the z component of the vectors) is manually set to 0.

3.3.5 *Histological analysis*

Following OMAG and PS-OCT imaging, each heart was sliced into 2 mm-thick sections from the apex for paraffin processing and embedding. 4 μm sections were cut and stained for picrosirius red/fast green to visualize the infarcted regions or for *Griffonia simplicifolia* lectin (GSL) to visualize vascular lumens. For GSL staining, slides were blocked with 1.5% normal donkey serum followed by sequential staining with GSL (Vector L-1100-5, 8 μg/mL), goat Ab to GSL (Vector AS-2104, 1:100), and a fluorescent secondary antibody. The infarct size was assessed from picrosirius red/fast green staining. The histological vessel area, density and size were quantified with a custom MATLAB code that analyzes confocal microscopic images of GSL-stained slides. Statistical analysis (ANOVA) was used to determine significance between groups.

3.4 Results

3.4.1 *Assessment of vascular density using OMAG*

To assess differences between the microvasculature of healthy and infarcted rat hearts, we acquired OCT scans of healthy and infarcted hearts, with infarcted hearts imaged in both the infarct region and the remote region on the posterior side opposite of the infarct. We used depth-resolved 3D Eigen-decomposition-based optical

microangiography (ED-OMAG) and created compressed 2D *en face* 4 mm x 4 mm images for visualization and quantification the coronary vasculature. (**Figure 3.3**).

First, we used the *en face* images to characterize the vasculature in each region in terms of its density and vessel size. Qualitatively, the healthy and remote regions did not demonstrate any difference in the distribution of microvasculature, however, the infarct region showed a dramatic reduction in microvascular density (**Figure 3.4A-C**). We quantified the vascular density of both capillaries (< 20 μm) and arteriole/venule size vessels (> 20 μm) using vessel area density (VAD) (**Figure 3.4D,E**). We found that

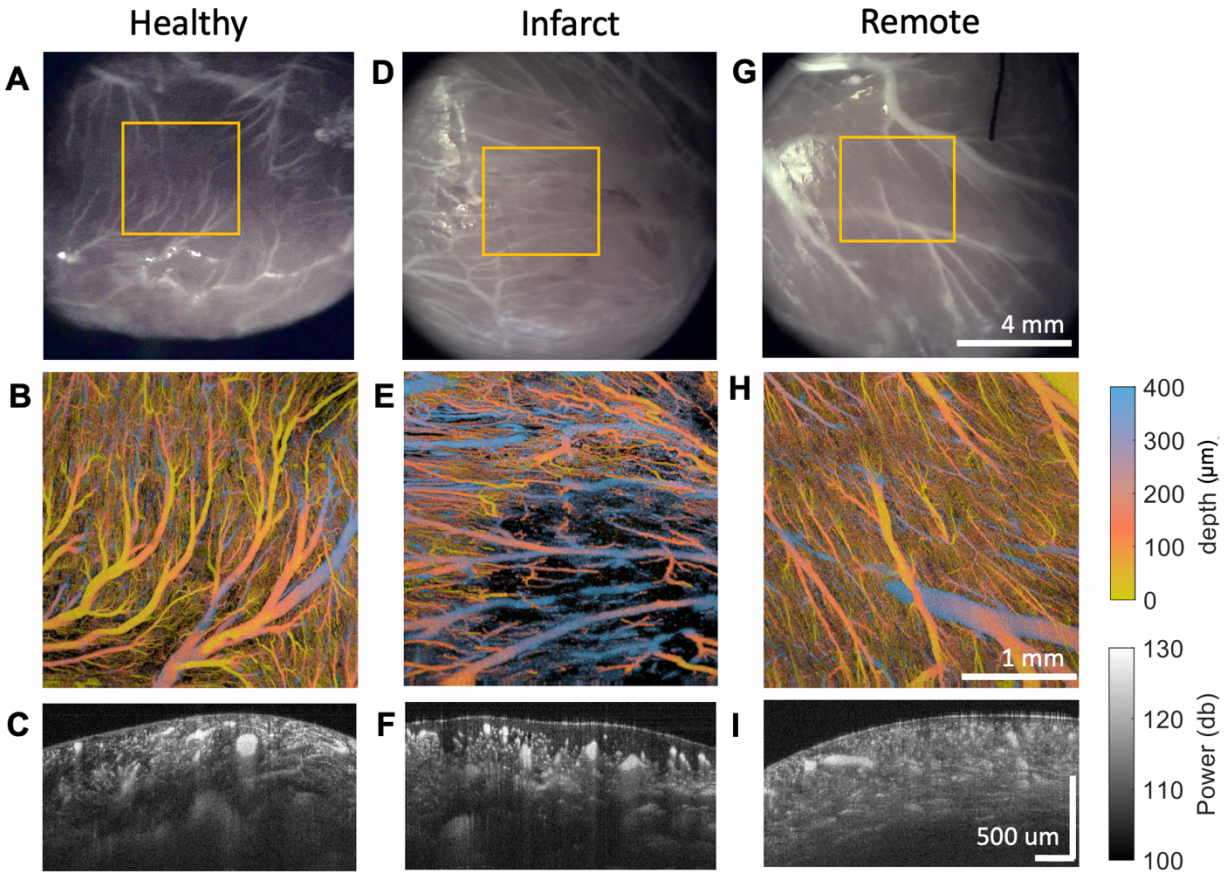

Figure 3.3 OMAG imaging of rat hearts. Representative white light and OMAG images of cardiac microvasculature in (A-C) healthy, (D-F) infarct, and (G-I) remote regions. (A,D,G) White light images with yellow box indicating scanned region. Scale bar, 4 mm. (B,E,H) Color coded *en face* OMAG images. Scale bar, 1 mm. (C,F,I) OMAG cross section images. Scale bar, 500 μm.

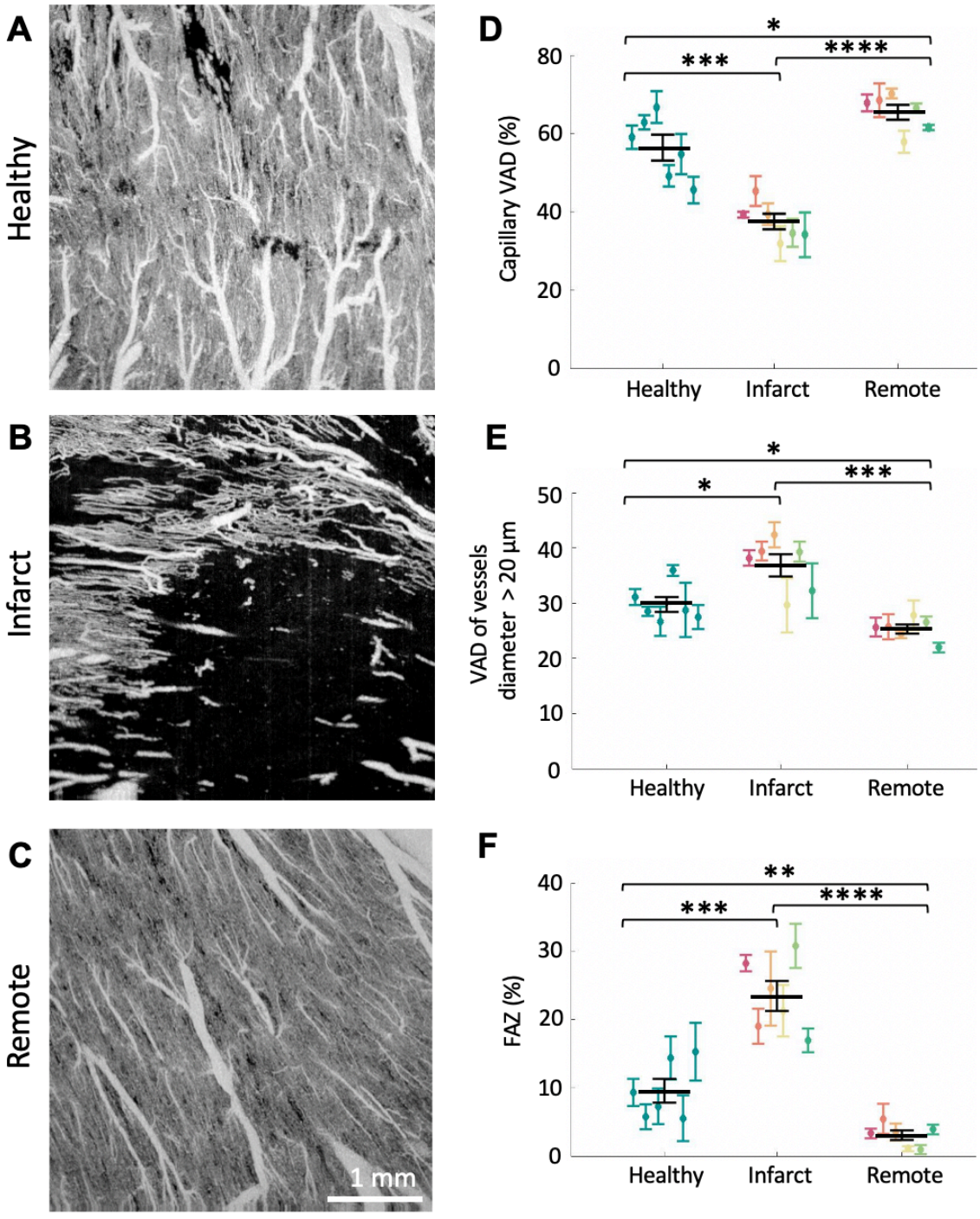

Figure 3.4 OMAG quantification of vessel density. (A,B,C) Representative *en face* OMAG images of (A) healthy, (B) infarct and (C) remote regions. (D,E) Quantification of vessel area density of (D) capillaries (<20 µm) and (E) arteriole/venule size vessels (>20 µm) as a percentage of total area. (F) Quantification of flow absent zone as a percentage of total area. The mean (±SEM) of each group was shown in black. The mean (±SEM) for each individual animal was shown in color with infarct and remote regions on the same heart shown in the same color. *p < 0.05, ** p < 0.01, ***p < 0.001, ****p < 0.0001.

capillary VAD (VAD_C) was lower in the infarct region (37.4 ± 2.0 %) than in both healthy (56.3 ± 3.3 %) and remote regions (65.4 ± 2.0 %), however, VAD for arteriole/venule size vessels (VAD_L) was greater in the infarct region than in healthy and remote regions (36.9 ± 2.0 %; 29.7 ± 1.4 %; 25.3 ± 0.9 %, respectively). This indicates that post-infarct remodeling causes a shift towards larger vessel sizes as previously described[155].

Additionally, we assessed the area in which flow was absent by the flow absent zone (FAZ). The FAZ was significantly larger, in the infarct region (23.5 ± 2.2 %) relative to both healthy (9.6 ± 1.7 %) and remote regions (3.0 ± 0.7 %) (**Figure 3.4F**). These results show that OMAG imaging can be used to non-invasively study vascular remodeling following myocardial infarction by demonstrating that myocardial infarctions lead to more sparse vascularization with a shift towards larger vessels at 1-month post-infarction.

3.4.2 *Assessment of vascular structure using OMAG*

Next, we sought to use our imaging pipeline to assess vascular morphology after myocardial infarction using two metrics, vessel complexity index (VCI) and vessel tortuosity index (VTI), where VCI is the ratio of vessel perimeter to vessel area and VTI measures the vessel curvature. Visually, the vessels appeared more complex and tortuous in the infarct region than in the healthy region (**Figure 3.5A,B**). Quantitatively, the vessels within the infarct region were found to be more complex with VCI being significantly greater in the infarct region (828.9 ± 61) relative to both healthy (469.8 ± 33) and remote regions (490.5 ± 61.6) (**Figure 3.5C**). Similarly, the vessels within the infarct region were significantly more tortuous than healthy and remote regions (1.15 ± 0.01; 1.11 ± 0.001; 1.10 ± 0.003, respectively) (**Figure 3.5D**). Interestingly, we saw that

infarcted heart varied greatly with only three of the six infarct hearts showing an increase of vessel tortuosity. These two metrics quantitatively showed that the microvasculature morphology in the infarct region is more complex and more tortuous. Taken together, this data indicates that OMAG can be used as a powerful tool to assess differences in vascular density and morphology between infarcted and healthy hearts.

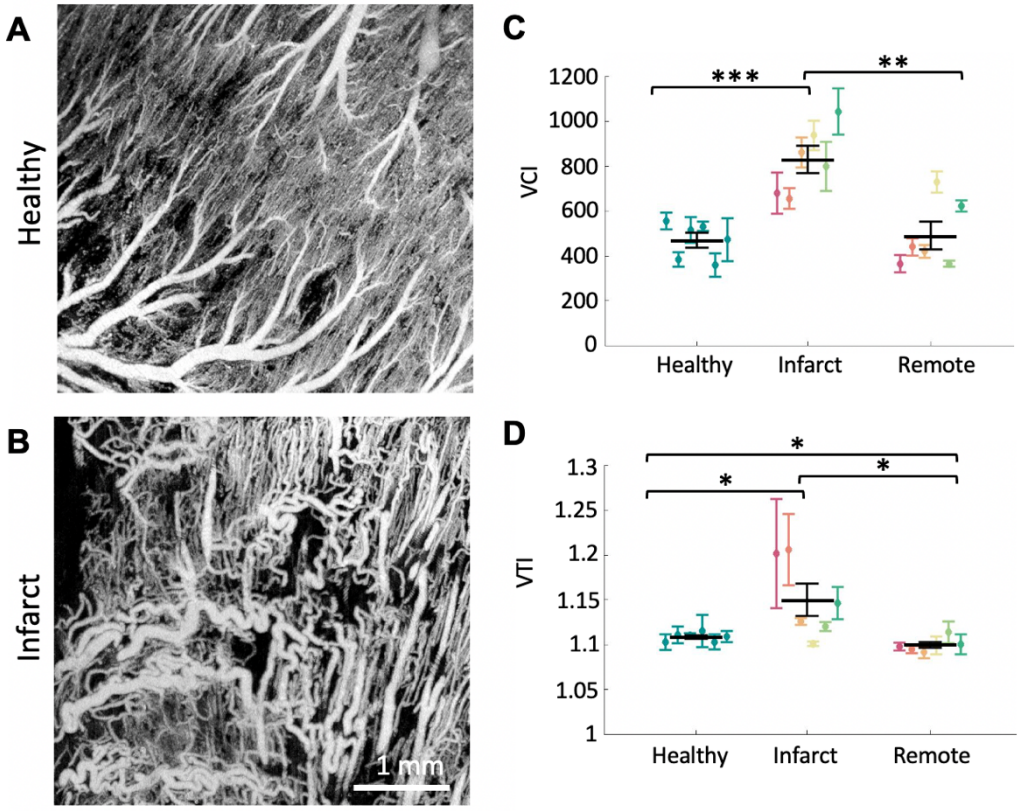

Figure 3.5 OMAG quantification of vessel structure. (A,B) Representative *en face* OMAG images of (A) healthy and (B) infarct regions. (C) Quantification of vessel complexity. (D) Quantification of vessel tortuosity index for larger vessels (< 20 μm). The mean (±SEM) of each group was shown in black. The mean (±SEM) for each individual animal was shown in color with infarct and remote regions on the same heart shown in the same color. *p < 0.05, ** p < 0.01, ***p < 0.001.

3.4.3 Assessment of perfusion dynamics using OMAG-V

To assess perfusion dynamics within the vasculature of infarcted and healthy hearts, we utilized OMAG-based velocimetry which provides measurements of the spatial flow velocity and generated 2D *en face* velocity maps. In healthy rat hearts, we detected flows that ranged between 0 and 1.6 mm/s within the vasculature (**Figure 3.6A**). In the infarcted hearts, we detected flows of similar ranges in both the infarct region and the remote region, however, there was notably less area with high flow in the infarct region while the flow distribution of the remote tissue appeared similar to that of the healthy heart (**Figure 3.6B-C**). To quantify flow dynamics, we first calculated the mean velocity of all the area that was perfusable in the OMAG images. Interestingly, we found no differences in the mean velocity between healthy, infarct, and remote regions (0.37 ± 0.03 mm/s; 0.39 ± 0.04; 0.50 ± 0.03, respectively) (**Figure 3.6D**). We next quantified the tissue perfusion where relative perfusion is the sum of all pixel velocities throughout the entire field of view relative to that of the healthy region average. We found that the relative perfusion of the infarct region (0.68 ± 0.09) was significantly less than that of the healthy (1.00 ± 0.1) and remote regions (1.07 ± 0.10) (**Figure 3.6E**). To determine whether these effects would be seen at the capillary level, we also quantified both mean velocity and relative perfusion in vessels that were < 20 μm in diameter. Again, we saw no differences in the capillary mean velocity between healthy, infarct and remote regions (0.29 ± 0.03 mm/s; 0.30 ± 0.02; 0.36 ± 0.03) and trends towards lower relative perfusion of capillaries in the infarct region (0.21 ± 0.11) than in the healthy (0.33 ± 0.14) and remote regions (0.31 ± 0.09) (**Figure 3.6F-G**). Together, this data suggests that while the infarcted tissue is less perfused at 1-month

post-infarction, this is in large part due to the differences in vascular density as opposed to flow rate.

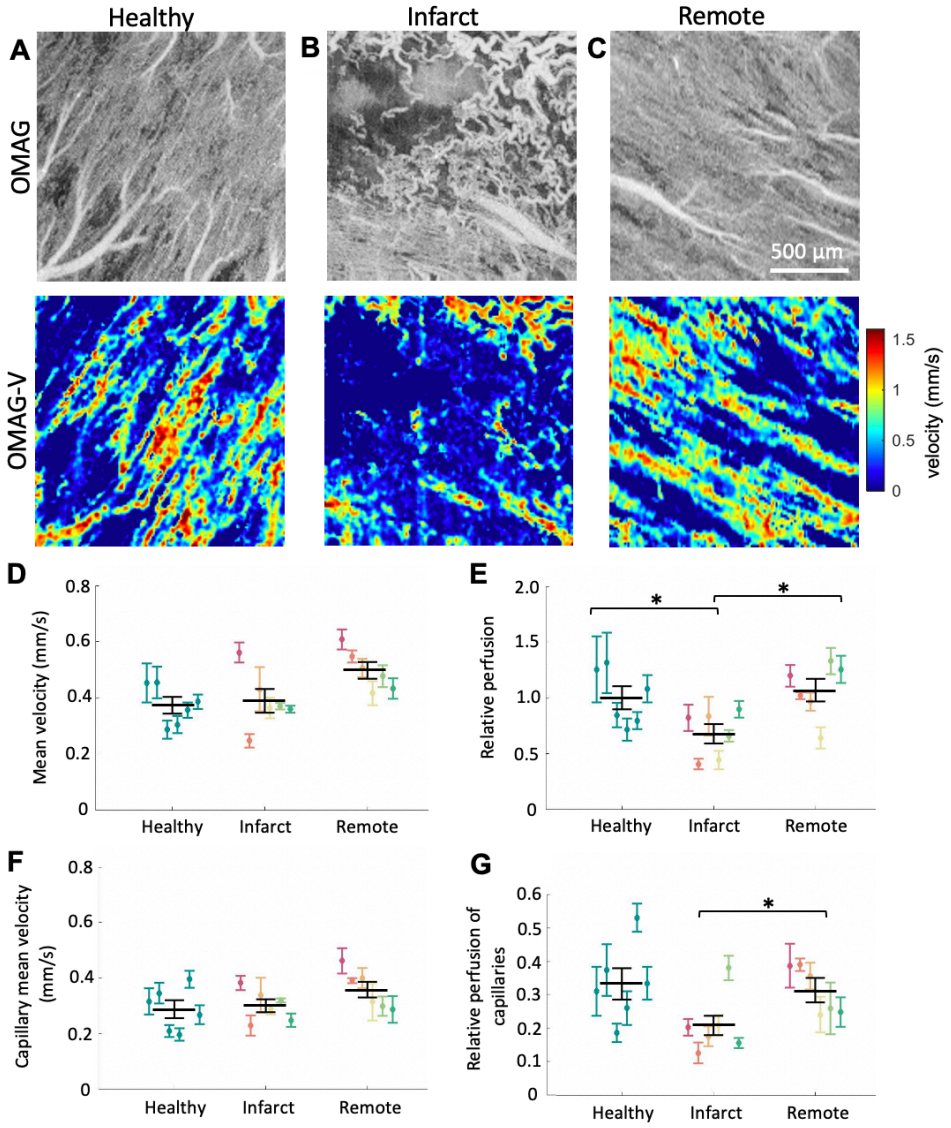

Figure 3.6 OMAG-V assessment of perfusion dynamics. (A,B,C) Representative *en face* OMAG images of (A) healthy, (B) infarct and (C) remote regions on top with corresponding OMAG-V . (D) Quantification mean velocity across vessels of all sizes. (E) Perfusion across vessels of all sizes relative to the average perfusion for healthy vessels. (F) Quantification of mean velocity across vessels < 20 µm in diameter. (G) Perfusion across vessels < 20 µm in diameter relative to the average perfusion for healthy vessels of all sizes. The mean (±SEM) of each group was shown in black. The mean (±SEM) for each individual animal was shown in color with infarct and remote regions on the same heart shown in the same color. *p < 0.05.

3.4.4 *Histological analysis of vascular structure*

To validate our results from OMAG imaging, we performed histology analysis of the healthy and infarcted hearts. First, Picrosirius red/fast green staining was used to visualize healthy and infarcted tissue in all hearts to ensure that imaged regions were appropriately characterized. With this stain, healthy tissue will be stained green while the collagenous scar of the infarct will be stained red. Healthy hearts do not contain any red regions, indicated that all tissue is healthy (**Figure 3.7A**). Infarcted hearts contain large red regions, indicating infarcts were successfully generated by the ischemia/reperfusion surgery (**Figure 3.7B**). Additionally, histological analysis confirmed that the infarcts reached the surface of the heart, the region imaged via OMAG, for all infarcted hearts in this study. All infarcts were an appreciable and similar in size (23.0 ± 3.7 % of left ventricle area) (**Figure 3.7C**). This staining confirms the state of the tissue and that infarcts were present where imaged.

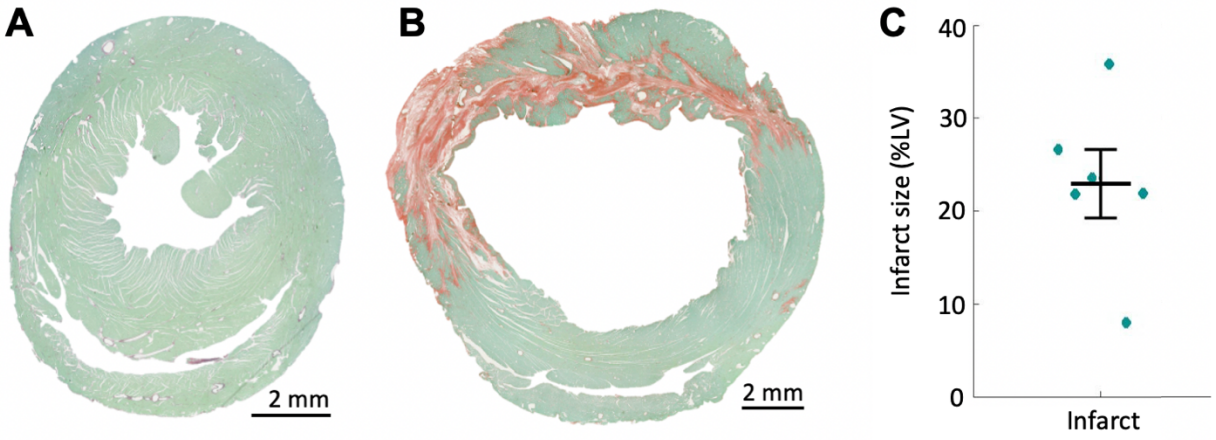

Figure 3.7 Histological analysis of healthy and infarcted hearts. (A) Healthy and (B) infarcted hearts stained for picrosirius red/fast green. Healthy tissue stains green, and infarcted tissues stains red. Scale bar, 2mm. (C) Quantification of infarct size as percentage of left ventricle area.

To visualize vascular patterns, histological sections were also stained for *Griffonia simplicifolia* lectin (GSL), which labeled the endothelium. The healthy and remote regions displayed many small, dense lumens, while the vasculature in the infarct region appeared highly irregular and void of many small capillaries (**Figure 3.8A,B**). Histological analysis confirmed that the blood vessels occupied a greater portion of the total area in healthy and

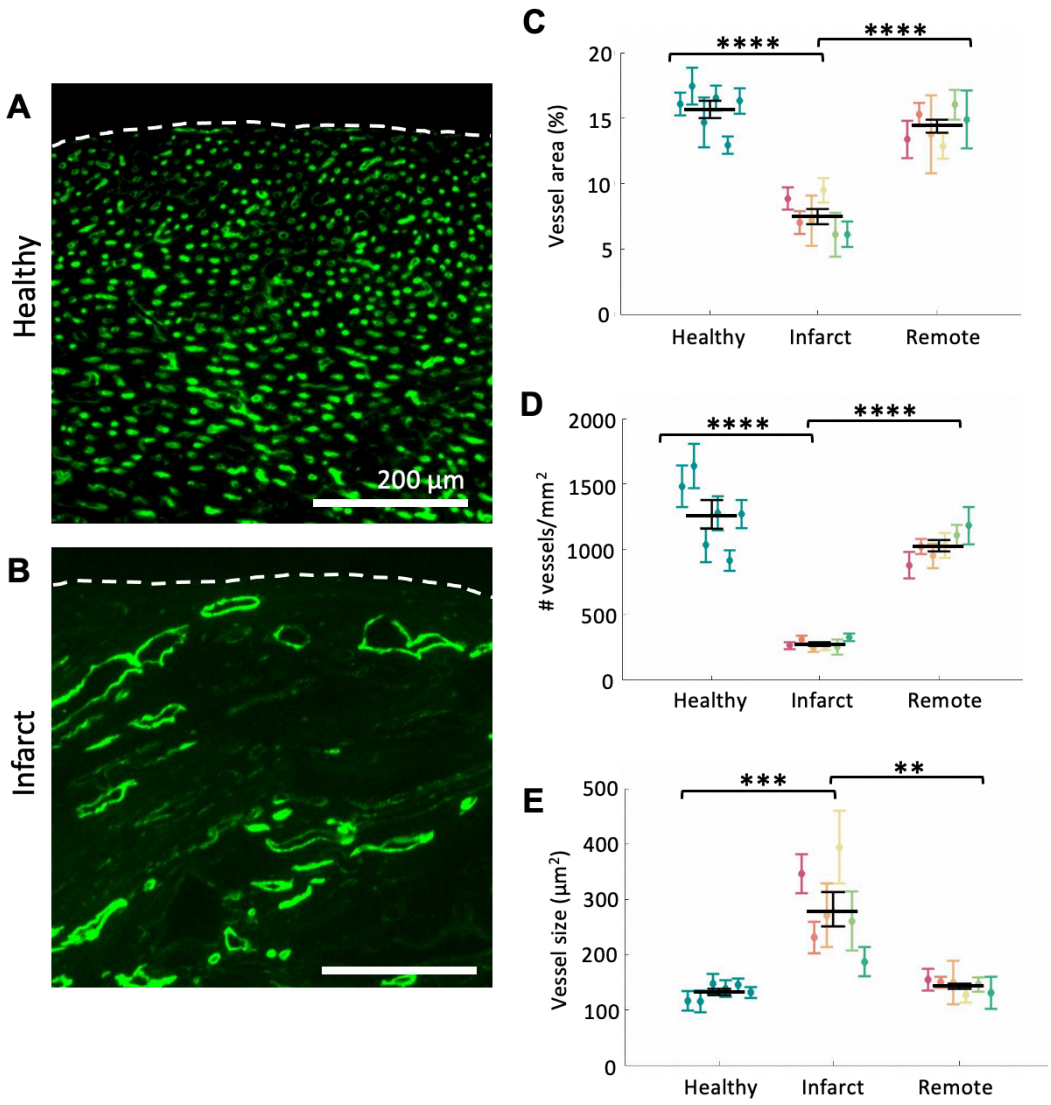

Figure 3.8 Histological analysis of vasculature by *Griffonia simplicifolia* Lectin (GSL) staining. (A,B) Confocal images of (A) healthy and (B) infarct regions stained for GSL in green. A dashed white line marks the surface of the hart. Scale var, 200 µm. (C-E) Quantification of (C) vessel area as a percentage of total area, (D) vascular density, and (E) average vessel size per region. The mean (±SEM) of each group was shown in black. The mean (±SEM) for each individual animal was shown in color with infarct and remote regions on the same heart shown in the same color. $p < 0.01$, ***$p < 0.001$, ****$p < 0.0001$.

remote regions when compared to infarct regions (**Figure 3.8C**). There were more vessels per mm^2 in the healthy and remote regions compared to the infarct region (**Figure 3.8D**). Additionally, infarct regions had greater average vessel sizes (**Figure 3.8E**). These results confirm the trends of lower vascular density and larger vessel sizes demonstrated in the OMAG imaging, reaffirming the ability of OMAG to capture relevant differences between infarcted and healthy vasculature.

3.4.5 *Assessment of fiber orientation using polarization sensitive OCT*

To demonstrate the ability of OCT-based imaging tools to characterize other structural differences between infarcted and healthy hearts, we utilized polarization sensitive OCT (PSOCT) to visualize fiber orientation. Linear gradient changes in the fiber orientation angle along depth was detected in the healthy heart due to the helical architecture of the myocardium (**Figure 3.9A**). In the en-face images (50 μm below the surface) selected at different depths (from 140 to 840 μm relative to tissue surface), the myofiber orientations were highly uniform at each depth and rotated gradually: the mean axis orientation determined from each en-face slice was 159.7° (i.e., −20.3°) ± 2.35°, 167.2° (i.e., −12.8°) ± 2.30°, 4.19° (± 2.49°), 11.7° (± 3.45°) and 45.7° (± 4.51°), respectively, with relative small standard deviations. This phenomenon is displayed using a polar histogram plot to visualize the dominant orientation direction and relative distribution of the optic axis at each depth (**Figure 3.9C**). The preferential collagen distribution demonstrates myofibril uniformity and anticlockwise rotation of the dominant fibers along depth. Depth-resolved reconstruction shows the gradient change of the myofibril direction over depth, consistent with the prior histological observations, demonstrating the usefulness of PSOCT method for studying myofibrillar alignment[178,179].

In comparison, the infarcted heart exhibited disorganization of the myocardial fibers along the depth within the cardiac wall (**Figure 3.9B**). In the *en face* axis orientation images selected at different depths, fibers in the superficial layer (140 μm relative to the tissue surface) appear uniform, which is similar to the healthy heart. Slightly deeper in the tissue, the fiber orientations show random and discontinuous patterns, indicating the presence of an infarct. The orientation distribution of the fibers at each depth in the infarct tissue is shown in the polar histogram, where except for the surface layer (140 μm), the distributions of the orientation in the infarct tissue are widely spread in the deeper layers (**Figure 3.9D**).

Cross-sectional images revealed a gradient of rotating fiber orientation through the wall of the healthy heart (**Figure 3.9E**). And in the infarcted heart, collagen fiber disorder begins around 300 μm from the outer wall (**Figure 3.9F**). Beneath this depth, a linear gradient change in fiber orientation is no longer observed, demonstrating remodeling of the fiber structure after infarction. These results are consistent with histological staining, where the superficial tissue of the infarcted heart appears normal (similar to the tissue of the healthy heart) and random fiber structures appear around 300 μm in depth (**Figure 3.9G,H**).

Depth-resolved axis orientation images of healthy and infarcted rat hearts revealed complex myocardial fiber arrangements which differ along the depth of the cardiac wall. The depth-resolved ability of the DDG-based PST method detected physiologic change deep within the cardiac wall. Overall, rodent heart imaging in this work demonstrated that the method can be readily applied to laboratory studies, potentially providing an insight into the physiology and pathology of the biological tissue.

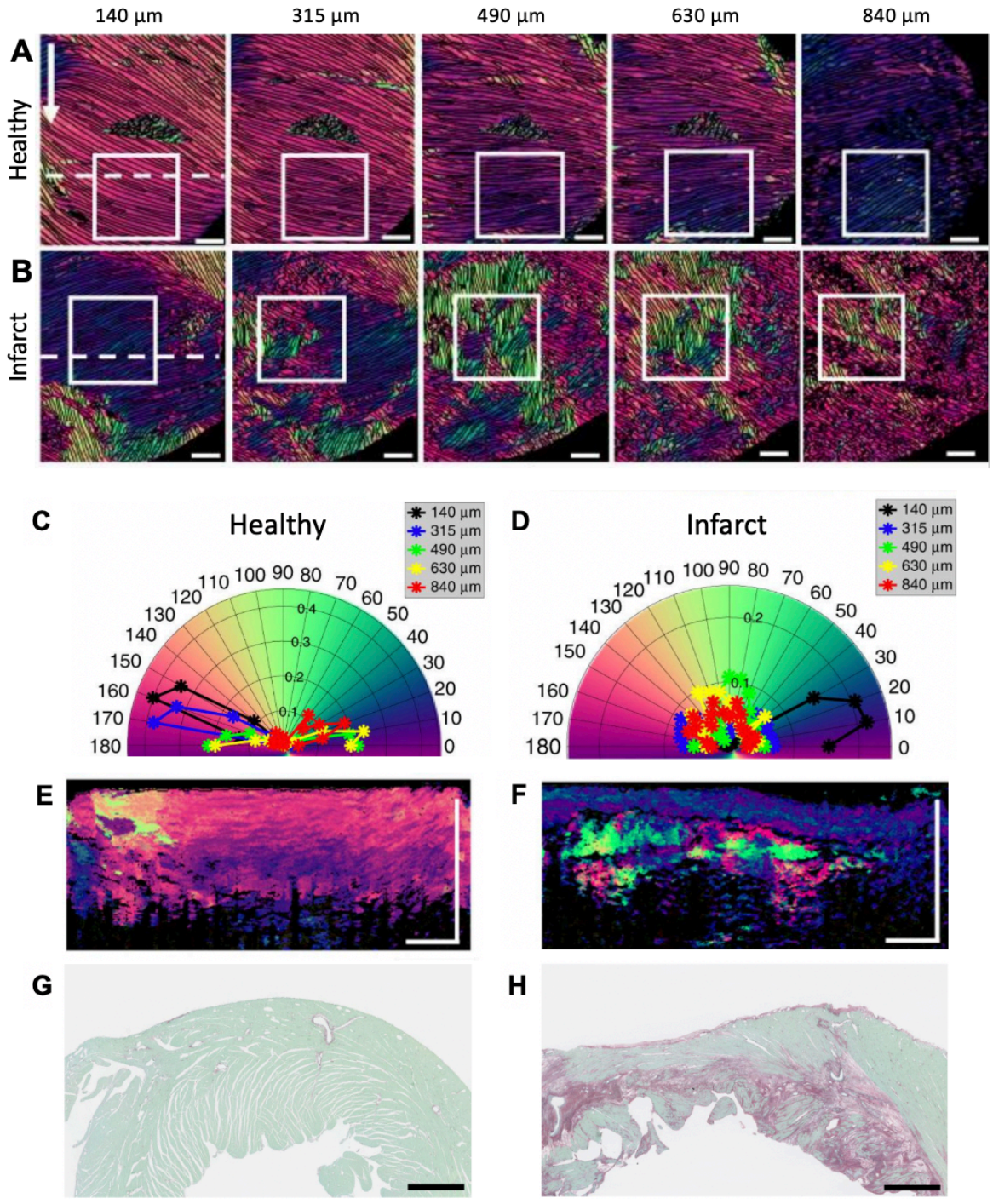

Figure 3.9 Depth-resolved fiber organization in healthy and infarcted rat hearts. (A) *En face* images of (A) healthy and (B) infarcted hearts at different depths as shown from 140 µm to 840 µm. Arrow points in the direction of top to bottom of the heart. Note that a triangular black tape was used as the guide to align the system scanning during imaging, which appears as an artifact in the middle of images in (A). Scale bar, 1 mm. (C,D) Polar histogram distributions of orientation obtained from the white boxes in (A,B). (E,F) Cross sectional views at the white dashed lines in (A,B). Scale bar, 1 mm. (G,H) Histology slices stained for picrosirius red/fast green at approximately similar locations as cross sectional views in (E,F). Collagenous/infarcted regions, red. Healthy tissue, green. Scale bar, 1 mm.

3.5 Discussion

Myocardial infarction often leads to deleterious remodeling and eventually heart failure. As such, monitoring vascular and structural remodeling is critical for better understanding of the post-infarction remodeling process and developing potential therapies for repair and regeneration. In comparison to other imaging approaches, OCT-based imaging offers a non-invasive, user-friendly, fast approach to image of complex 3D architecture and perfusion with high resolution and wide field of view, making it a valuable tool for studying heart remodeling. Here, we developed OCT techniques to monitor vascular perfusion and fiber orientation changes in the rat hearts post-infarction.

First, we assessed vascular structure using optical microangiography (OMAG) and quantitatively measured four different metrics (VAD, VCI, VTI, and FAZ) to characterize microvascular morphology in *ex vivo* fixed healthy and infarcted rat hearts. Next, we evaluated perfusion dynamics of in both healthy and infarcted regions using OMAG-based velocimetry (OMAG-V). Wide-field quantitative assessments were performed on the *en face* OMAG or OMAG-V images. Our result showed that the metrics quantified based on the microvasculature morphology and tissue perfusion in the infarct regions are dramatically different compared to that of the healthy and remote regions and demonstrate that these metrics are sufficiently sensitive to detect changes in the microvascular network after myocardial infarction. Additionally, we assessed the fiber orientation of healthy and infarcted rat hearts using polarization sensitive OCT (PSOCT) and observed helical architecture in the healthy heart but clear fiber disorganization in the infarcted heart. These results demonstrate that multiple OCT-based imaging approaches,

OMAG, OMAG-V and PSOCT, may be utilized to provide valuable insights into post-infarction remodeling in the heart.

As the current standard for assessment of vasculature and myofiber architecture, we additionally used histological analysis to confirm the trends of decreased vascularization and larger vessel size in infracted regions that were apparent from the OMAG images as well as collagenous scar location revealed in the PSOCT images. Although histology can provide valuable information about tissue morphology, it is not an ideal technique for understanding complex vascular networks because it is limited to 2D cross sections. For example, histological analysis does not provide adequate information to study the tortuosity of the vasculature. Additionally, reconstruction of 3D collagen architecture from 2D stacks of histology is extremely challenging. As exemplified in our study, OCT-based imaging provides 3D information about the vascular and fiber architecture, enabling greater understanding than possible with histology.

While massive capillary loss could be visually identified from *en face* OMAG images of the infarct region, this study also provided quantitative measures to evaluate the condition of the infarcted myocardium. The decline of capillary VAD and increase of FAZ both reflect severe structural damage of the coronary microvasculature as a result of the myocardial infarction. This maintained loss of microvasculature would result in a longer diffusion distance to nearby tissue, reduced accessibility for oxygen and nutrients in the infarcted myocardium, and therefore prevention of positive tissue remodeling[151]. Although the resolution of our OCT system is high, our VADc quantification might remain an estimation because the capillary diameter and intercapillary distance are below system resolution, preventing each vessel from resolving in the OCTA *en face* image.

The increase in VAD for arteriole/venule sized vessels within the infarct region suggested a potential expansion of vasculatures in the infarcted region consistent with other studies. It has been demonstrated that the capillary vessels present in the infarct will increase their output by increasing their size, providing functional collateral flow in the surface artery network during redistribution in blood flow after massive capillary loss[153]. This is also seen in the study by Gkontra et al., where the infarcted area showed more perivascular cells on the vessel wall, suggesting vessel dilation post-infarction[50,154]. Our results are in line with this known biological process.

To balance the oxygen diffusion efficacy, newly formed vessels within an infarct can develop into a more tortuous shape to increase the blood flow path length for a higher surface to area ratio. Yet, the tortuous vessels are poorly perfused and would cause damage to the myocardium and surrounding microvasculature structures compared to the healthy capillary bed. Thus, vessel tortuosity remains one of the most common pathological biomarkers. A statistically significant increase in VCI and VTI in the infarct region demonstrated that these metrics could be used as a good indicator to reflect the change in geometric characteristics of coronary vasculature after myocardial infarction. Notably in our assessment, there were no significant differences between the VCI of healthy and remote regions, suggesting that morphological changes that occurred in microvascular networks and infarct scar remaining mainly local to the site of injury.

While statistical significance was found between the infarct region when compared to the healthy and remote regions using the VTI metric, interestingly, only three of the six hearts showed a dramatic increase in the infarct region. The conditions can vary between each biological sample and even between regions on the same sample. This

result suggests that tortuous vessel reconstruction after myocardial infarction might not occur consistently. As such, increasing the sample size in this study may provide higher statistical power. Moreover, although the arc-chord ratio applied in this study for VTI is the most frequently used metric to quantify local vascular tortuosity in 2D projections, the simplicity of this method could limit its sensitivity to the oscillated curvature when down the total pathlength of each vessel, as when vessel have multiple turns between branch points[180]. Additionally, VTI is sensitive to the *en face* compression because the projection view conceals the tortuosity in the z-dimension and VTI would not be sensitive to infarct regions that had significant lack of vasculature. Additional advanced metrics, such as 3D vessel tracing, may be more suitable for case studies on tortuosity quantification on single vessels and could be implanted in future studies.

Although our study demonstrates the feasibility of using OMAG and OMAG-V to identify differences in the vasculature of healthy and infarcted hearts, some limitations exist. One limitation of this study is that shallow tissues depths were used to prevent vessel overlay between multiple capillary layers within the projection, therefore this study was not sensitive to the characteristics through the whole tissue. Additionally, there could be a loss of detailed topological information of the microvasculature because OMAG would not be able to detect vessels that cannot be perfused under specific pressure[147]. In such conditions, the binarization processes using a hessian filter and OSTU's threshold may not reflect the morphological characteristics of all vessels captured within the field of view.

The results of our fiber orientation study also demonstrate the feasibility of using PSOCT to study cardiac remodeling. For example, the depth-resolved PSOCT system

could be used to monitor the healing response after myocardial infarction or remodeling of implantable tissue grafts. The understanding of these matrices and remodeling could help understanding many important physiological diseases, such as biomechanical origin of arrhythmia. However, we note that 22 μm lateral resolution may not be sufficient for detecting minute changes in collagen organization of the heart. Also, it is difficult to observe the dynamics of the myocardial fibers of the whole heart during heart beating because there is a time delay induced by the point scanning protocol when imaging different parts of heart. These two issues can be mitigated simultaneously by integrating the full-field microscopy into the PSOCT system. A high-resolution (~1 μm) 3D volumetric collagen organization image can be obtained with a single shot rather than point scanning. However, imaging depth would decrease in this case.

In conclusion, this study demonstrated high-quality in-depth acquisition and reconstruction of heart microvascular structure over a large field of view using OMAG, perfusion dynamics within the heart vasculature using OMAG-V, and fiber orientation using PSOCT. An automatic method for quantifying microvascular morphology was presented to summarize unbiased characteristics in healthy and infarcted rat hearts. VAD of capillaries and arterioles/venules, VCI, VTI, FAZ, velocity and relative perfusion were quantified from OMAG and OMAG-V vasculature *en face* projection images. Significant changes were seen in vessel density, vessel shape, and tissue perfusion after myocardial infarction. Subsequently, PSOCT was used to generate maps of fiber orientation, indicating the location of the collagen scar in infarcted hearts. In summary, the non-invasive OCT-based imaging modalities utilized in this study could provide a valuable means for further understanding of the post-infarction remodeling processes in the heart.

Chapter 4. Investigate the role of patterned, perfusable vascular networks for engineering implantable cardiac tissues

Parts of this chapter have been published in the following manuscript:

Meredith Redd*, **Nicole Zeinstra***, et al. "Patterned human microvascular grafts enable rapid vascularization and increase perfusion in infarcted rat hearts." Nature communications, 2019[125]. * equal contribution.

4.1 Abstract

Vascularization and efficient perfusion are long-standing challenges in cardiac tissue engineering. Here we report engineer perfusable microvascular constructs, wherein human embryonic stem cell-derived endothelial cells (hESC-ECs) are seeded both into patterned microchannels and the surrounding collagen matrix. *In vitro*, the hESC-ECs lining the luminal walls readily sprout and anastomose with de novo-formed endothelial tubes in the matrix under flow. These constructs are minimally thrombogenic when perfused with blood, have gene expression associated with vascular and tissue development, and can be perfused with sustained perfusion ideal of supporting thick tissues. When cardiac tissues made by adding hESC-derived cardiomyocytes are implanted on infarcted rat hearts, the perfusable microvessel grafts integrate with coronary vasculature to a greater degree and have higher cardiomyocyte density than non-perfusable self-assembled constructs at 5 days post-implantation. Thus, pre-

patterned vascular networks enhance vascular remodeling and accelerate coronary perfusion, potentially supporting cardiac tissues after implantation. These findings should facilitate the next generation of cardiac tissue engineering design.

4.2 Introduction

Engineered tissues have emerged as promising approaches to repair damaged organs as well as useful platforms for drug testing and disease modeling[181,182]. However, insufficient vascularization is a major challenge in engineering complex tissues such as the heart[183,184]. Heart failure is the leading cause of death worldwide, and no available treatment options outside of whole heart transplantation address the problem of cellular deficiency[150,185]. Despite this burgeoning clinical need, the therapeutic application of engineered cardiac tissues has not been achieved, partially due to the lack of comprehensive tissue perfusion *in vitro* and effective integration with host vessels *in vivo*[184].

Prior efforts to vascularize tissue grafts have mostly relied on self-assembly of endothelial cells to form connected tubes within cardiac constructs[97,102,103]. Although the presence of these vessels improves cardiomyocyte maturation and tissue function, the formed network architecture does not provide efficient perfusion, preventing large-scale construct fabrication and culture. When implanted, these grafts partially integrate with host vasculature, but do not establish effective perfusion in a timely fashion[186]. To combat this problem, efforts have been made towards fabricating perfusable vasculature within cardiac tissue constructs in our lab and in others[115,117,125]. Little is known, however, about how these vascular networks will connect with host vessels once implanted.

An engineered tissue also requires appropriate cell sources, which are not only important to promote tissue function, but also critical for clinical translation. In particular, the field of vascularization has mostly relied on HUVECs, a commonly used endothelial source with known function and availability but poor survival and immunogenic issues *in vivo*[187,188]. Our lab has demonstrated that we can use human pluripotent stem cells to derive endothelial cells (hESC-ECs)[73,74] and cardiomyocytes[80,102,189] from mesodermal precursors. Importantly, these hESC-ECs exhibit increased angiogenic behavior in flow-derived microphysiological constructs and are vasculogenic when embedded in bulk hydrogel matrix. These properties indicate hESC-ECs could be an ideal cell source for engineering constructs with high vascular density.

In this study, we combine advanced tissue engineering and stem cell biology to study the vascular anastomosis and host integration of vascularized cardiac tissues in the infarcted heart. We demonstrate vascular remodeling and anastomosis *in vitro* between pre-patterned, perfusable vascular networks, and self-assembled vessels in the bulk matrix, both with hESC-EC cell sources. We saw that hESC-EC-derived microvessels were minimally thrombogenic and could be converted into a thrombogenic state, demonstrating an ideal interaction with blood for *in vivo* implantation. We show remodeled constructs with vascular anastomosis have upregulated genes associated with vascular and tissue development. We found that hESC-ECs are sensitive to flow, but can be cultured with sustained perfusion by using an intermittent flow profile. Importantly, these pre-patterned perfusable constructs improved vascular host integration, which likely supported graft cardiomyocyte remodeling when implanted on an infarcted heart compared to self-assembled controls. Our work demonstrates that pre-perfused,

patterned vessels provide important cues for rapid anastomosis and host integration, and sheds light on engineering translational cardiac patches for heart regeneration.

4.3 Scientific Methods

4.3.1 Generation of hESC-derived endothelial cells

All experiments used cells derived from RUES2 (Rockefeller University, NIH 0013) hESCs. *In vitro* microvessel experiments used genetically modified RUES2 hESCs that contain a dual-reporter (mTmG-2a-Puro) transgene[190]. Cells were maintained in undifferentiated colonies on Matrigel (BD Biosciences) coated plates with mTeSR-1 (Stemcell Technology) or mouse embryonic fibroblast conditioned media (MEF-CM) supplemented with 5 ng/mL human basic fibroblast growth factor (hbFGF) (Peprotech)[191]. Untreated cells with the dual-reporter transgene stably express tdTomato red fluorescent protein (mTm). To generate a stable GFP stem cell line, mTmG-2a-Puro hESCs were treated with 5 μM de-salted Cre recombinase (Excellgen) for 24 hours to induce recombination and excision of TdTomato followed by two 24 hour doses of 5 ng/mL puromycin (InvivoGen) to purify the recombined population. GFP-expressing cells were expanded and analyzed for GFP purity using flow cytometry on unfixed and unstained cells. hPSCs were differentiated into endothelial cells through cardiac mesoderm using high Activin A and low BMP4 (**Figure 4.1A**)[73,74]. Briefly, single cell suspensions of noncolored or mTm- and GFP- expressing hESCs were obtained using enzymatic dissociation and re-plated on Matrigel at a density of 105K cells per cm^2 in mTeSR-1 or MEF-CM + 5 ng/mL bFGF and 1 μM CHIR-99021 (Cayman Chemical). When the plated cells reached about 80% confluent monolayer, they were fed with day 0 induction media

(100 ng/mL Activin A (R&D) in RPMI (Gibco, with L-glutamine) + B27 supplement (ThermoFisher, without insulin) and 1X Matrigel. 18 hours post induction, the cells were fed with 5 ng/mL BMP4 (R&D) and 1 μM CHIR-99021 in RPMI + B27 (without insulin). 24 hours later, the media was changed to endothelial induction media: Stempro34 (Invitrogen) containing 200 ng/mL VEGF (Peprotech), 5 ng/mL bFGF, 10 ng/mL BMP4, $4x10^{-4}$ M monothioglycerol (Sigma), 50 μg/mL Ascorbic Acid (Sigma), 2 nM L-Glutamine (Invitrogen) and pen-strep (Invitrogen). The cells remained in endothelial induction conditions for 72 hours, with no media changes. At the end of 72 hours (differentiation day 5), endothelial progenitor cells were harvested for re-plating and flow cytometry analysis. The cultures were fed with fresh Stempro (with L-glutamine and pen-strep) 1 - 2 hours prior to re-plating to improve survival and attachment. Cells were then enzymatically harvested to obtain a single cell suspension and re-plated in 0.2% gelatin coated tissue culture flasks with endothelial growth media (EGM, Lonza) containing 20 ng/mL VEGF (Peprotech), 20 ng/mL bFGF, and 1 μM CHIR-99021. An aliquot of day 5

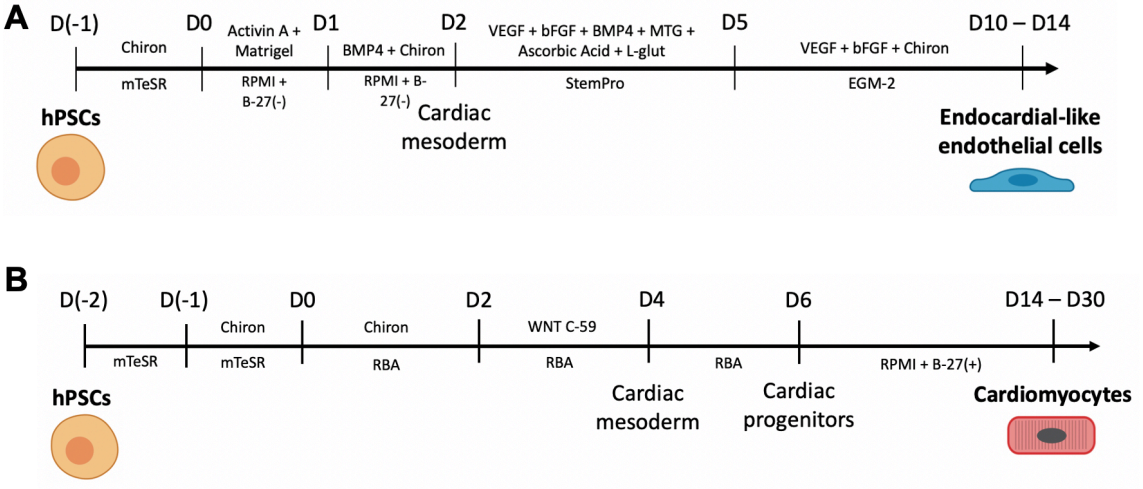

Figure 4.1 Differentiation of hESC-ECs and hESC-CMs. (A) Differentiation protocol of hPSCs into endocardial-like endothelial cells (hESC-ECs) through cardiac mesoderm. (B) Differentiation protocol of hESCs into cardiomyocytes (hESC-CMs).

cells was stained with CD34 - APC FACs antibody (BD 555824, 1:4) and analyzed with flow cytometry to determine differentiation efficiency of endothelial progenitors. Re-plated cells were maintained in EGM with CHIR-99021, bFGF, and VEGF (EGM + Factors). In all experiments, hESC-ECs were harvested at differentiation day 10 – 14 and then used to generate engineered microvessels. Aliquots of differentiated cells were stained with CD31 – PE FACs antibody (BD 555446, 1:4) and analyzed with flow cytometry to determine endothelial purity. All staining for flow cytometry was done on live cells. Aliquots were washed in PBS containing 5% FBS, resuspended in DMEM media (Corning) with conjugated antibody, and kept in the dark on ice for 45 minutes. Stained cells were washed and analyzed immediately with FACs Canto II cell analysis instrument and FlowJo Software.

4.3.2 *Generation of hESC-derived cardiomyocytes*

Noncolored RUES2 hESCs were differentiated into hESC-derived cardiomyocytes (hESC-CMs) using modulation of Wnt signaling (**Figure 4.1B**)[72]. Briefly, undifferentiated cells were maintained as described above in mTeSR-1. Single cell suspensions of noncolored hESCs were dissociated and replated at a density of 40K cells per mm^2 in a Matrigel-coated 12 well plate in mTeSR-1. After 24 hours, cells were supplemented with 1 μM CHIR-99021. At 48 hours after replating, cells were fed with day 0 induction media of 3 μM CHIR-99021 in RPMI containing 500 μg/mL bovine serum albumin (Sigma) and 213 μg/mL ascorbic acid (RBA). On day 2, media was changed to 2 μM WNT-C59 (Selleck) in RBA media. On day 4, media was changed to RBA without supplementation. Beginning on day 6, cells were fed with RPMI + B27 supplement (ThermoFisher, with

insulin) on every other day until harvest. Initial beating was observed on day 6 – 8. In all experiments, cardiomyocytes were enzymatically harvested into a single cell suspension at differentiation day 29 – 31 and then used to generate cardiac constructs. Aliquots of differentiated cells were stained with mouse anti-cTnT (ThermoScientific MS-295, 1:100) and goat anti-mouse IgG-PE (Jackson Cat 115-116-072, 1:200) for 30 minutes each in PBS containing 0.75% saponin and 5% FBS (Gibco). Stained cells were analyzed by flow cytometry with FACs Canto II cell analysis instrument and FlowJo Software to determine cardiomyocyte purity. For all cardiac constructs, hESC-CMs had cardiomyocyte purity >70% (Supplementary Figure 11A-B).

4.3.3 *Fabrication and culture of engineered microvessels*

Engineered microvessels were generated using injection molding and soft lithography techniques[123,124]. Briefly for endothelial cell only microvessels constructs, 15 mg/mL stock collagen (dissolved in 0.1% acetic acid) was neutralized and diluted to 6 mg/mL on ice with 1M NaOH (20 mM final), 10X M199 (Sigma), and EGM[124]. For constructs containing cardiomyocytes, 15 mg/mL stock collagen was diluted to 6 mg/mL on ice with 1M NaOH (10mM final), 10x RPMI (Sigma, 1x final), 30x Matrigel (1x final), 100x Hepes (Invitrogen, 1x final), and RPMI + B27 supplement[125]. For experiments containing hESC-ECs in the bulk collagen, the cells were added after the collagen was neutralized at a density of 3 x 10^6 per mL, and the volume of EGM was adjusted accordingly to compensate for the additional volume of cells. For cardiac constructs, cells were added to collagen mixture at densities of 12 x 10^6 per mL hESC-CMs, 3 x 10^6 per mL hESC-ECs, and 3 x 10^6 per mL human bone marrow-derived stromal cells (HS-27a).

HS-27a (courtesy of Beverly Torok-Storb laboratory at Fred Hutchinson Cancer Research Center) were maintained on 0.2% gelatin-coated flasks in DMEM GlutaMAX (Thermo Fisher) containing 20% FBS and 1x pen-strep.

Specially designed devices that contain holes for collagen injection, inlet, and outlet were used during injection molding, assembly, and microvessel culture. The microchannels were created by molding liquid 6 mg/mL collagen (acellular (μV only) or hESC-EC containing (μV+SA)) around a microfabricated polydimethylsiloxane (PDMS) stamp that contains vessel network geometry. For *in vitro* experiments, 3 x 3 geometry with 100 μm feature height was used. After gelation, the channel was enclosed with a separately generated flat layer of collagen to create embedded microfluidic channels surrounded by native collagen matrix on all sides. Day 10 - 14 noncolored or mTm-hESC-ECs were seeded in the channel by perfusing at a density of 10 x 10^6 per mL. The cells were allowed to circumferentially attach overnight in static conditions, followed by flow through the lumen to remove the non-attached cells in the lumen and reservoir. Constructs were then cultured under gravity driven flow for 4 or 7 days with EGM + factors media. Gravity driven flow is generated by replacing the media at the device inlet every 12 hours for the duration of the culture period. These culture conditions generate sheer stresses on the order of 0 – 10 dyne per cm^2 with a time average of 0.1 dyne per cm^2 and the highest sheer application immediately after media replacement[124]. For sustained perfusion experiments, microvessels were connected to an ELVEFLOW OB1 pressure driven microfluidic system using tubing then perfused with EGM + GFs using continuous (2 μL/min) or intermittent (cycles of 2 μL/min for 1 hours then 0.1 μL/min for 3 hours). For perfusable cardiac constructs, housing devices contained pieces that were removed after

collagen gelation to allow for additional media access. Cardiac constructs were submerged in 25% EGM + factors and 75% RPMI + B27 supplement and cultured under gravity driven flow with EGM + GFs.

4.3.4 *Analysis of in situ microvessel immunofluorescence and bead perfusion*

To assess the cell death in microvessels, vessel lumen was perfused with 10 μM ethidium homodimer-1 and Hoechst for one hour followed by 3x 5 min PBS washes, then imaged on a Nikon A1R confocal microscope for z-stack images before fixation. ImageJ particle analysis for red channels within the specified distance ranges from the microvessels: [0 - 300 μm], [300 - 600 μm], and [600 - 900 μm]. In other conditions, engineered vessels were perfusion-fixed after 4 or 7 days in culture with 3.7 % formaldehyde (Sigma) for 20 minutes followed by 3x 20 min PBS washes. Samples were blocked in 2% BSA (Sigma) and 0.5% Triton X-100 (Sigma) in PBS for one hour followed by an overnight incubation with the following primary antibodies at 4°C: rabbit pAb to hCD31 (abcam 28364, 1:25), mouse pAb to VE-Cadherin (abcam 7047, 1:50), rabbit pAb to DsRed (abcam 16667, 1:100), and goat pAb to GFP (abcam 5450, 1:400). One hour incubation with the following secondary antibodies, conjugated primary antibodies, and nuclei counterstains was performed at room temperature: donkey anti-goat Alexa Fluor 488 (Invitrogen A11055, 1:100), donkey anti-mouse Alexa Fluor 647 (Invitrogen A31571, 1:100), donkey anti-rabbit Alexa Fluor 594 (Invitrogen A21207, 1:100), and Hoechst 33342 (Sigma, 1:250). Three-dimensional z-stack images were acquired on a Nikon A1R confocal microscope with all image post processing and quantification done with ImageJ software. GFP-hESC-EC density and lumen size were quantified in μV + SA constructs

by applying a threshold to maximum intensity projections of the GFP channel followed by ImageJ particle analysis (particles less than 20 μm^2 in size excluded to account for background) within the specified distance ranges from the microvessels: [0 - 300 μm], [300 - 600 μm], and [600 - 900 μm]. After all confocal images were collected, vessels were perfused with 50 μL of 1.0 μm diameter red fluorescent beads (Thermo Fisher F13083, 1 x 10^{10} beads per mL, 580/605) diluted 1:30 in PBS. Brightfield and fluorescent time series were collected with no delay at 10X magnification on a Nikon high resolution wide-field microscope. Perfusion area was quantified by measuring the total area of perfused beads in large images that were manually stitched together with ImageJ software from smaller 10X. For each vessel, the stitched image encompassed a field of view twice the area of the original pattern boundary.

4.3.5 *Whole blood perfusion and analysis of platelet accumulation*

Fresh blood (in 0.129 M sodium citrate) was obtained through Puget Sound Blood Center under University of Washington Institutional Review Board (IRB) approved protocols from consenting healthy donors. Platelets in the platelet-rich plasma (PRP) were labeled with FITC-conjugated CD41a antibody (BD 555466, final concentration of 2.5 μg/mL) for 30 min at room temperature. The labeled PRP were reconstituted with red blood cells and buffy coat at the original ratio to produce reconstituted whole blood, which was perfused through the live microvessels that had first been washed with PBS. For activated microvessels, 50 ng/mL PMA or 1μg/mL IL-1β were perfused through the vessel lumen for 30 mins before PBS wash. The blood flow was set for 15 to 30 minutes so that the wall shear stresses are at between 10 and 30 dyne per cm^2. All blood perfusion

experiments were done in mTm-hESC-EC seeded microvessels that were cultured for 4 days. Brightfield and fluorescent no delay time series were collected at 10X magnification on a Nikon high resolution wide-field microscope to visualize red blood cell movement and platelet accumulation of the vessel walls. At the end of blood perfusion, the vessels were washed with PBS for three times to remove the excessive blood cell suspensions, and fixed *in situ* using 3.7% formaldehyde. The vessels were then washed with PBS three times and immunohistochemically stained for CD31 and VWF, and imaged in a Nikon A1R confocal microscope to obtain image stacks along z direction[124]. Using ImageJ software, the projections of image stacks were made and platelet adhesion was quantified by measuring the area of CD41a+ fluorescent signal and normalizing to vessel wall surface area.

4.3.6 *RNA isolation and RNA-seq data analysis*

Total RNA from three types of constructs was purified using the RNAeasy Mini Kit (Qiagen) and residual DNA was removed by on-column DNase digestion. RNA quality was assessed with the Agilent RNA 6000 Nano Kit using the Agilent 2100 Bioanalyzer (Agilent Technologies). Only samples with RNA integrity number higher than 8 were kept for further analysis. RNA sequencing was performed on poly-A-enriched samples using Illumina TruSeq.

RNAseq samples were aligned to hg38 using TopHat v2.1.0[192]. Gene-level read counts were generated with htseq-count v0.6.1p1 using the intersection-strict overlapping mode[193]. Genes with more than 1 reads per million in at least 2 samples were kept for further analysis. The GLM method in edgeR v3.18.1 was used for differential expression

analysis[194]. *prcomp* function from R was used to for Principal Component Analysis. Genes with fold change >1.5 and FDR<0.01 were considered differentially expressed. Hallmarks gene set was used for pathway enrichment analysis[195]. Hypergeometric test was used to test the significance of overlap between up-/down-regulated genes and a pathway.

4.3.7 *Rat ischemia/reperfusion and cardiac patch implantation surgeries*

All animal procedures in this study were approved by the University of Washington Institutional Animal Care and Use Committee (IACUC, protocol #2225-04) and performed in accordance with US NIH Policy on Humane Care and Use of Laboratory Animals. Male athymic nude Sprague-Dawley rats (approximately 250 g – 300 g, 8 weeks of age) underwent two thoracotomy surgeries for ischemia/reperfusion injury (I/R) and implantation of vascular grafts (4 days post I/R). Subcutaneous administration of sustained release buprenorphine (1 mg/kg) provided analgesia for at least 2 days after all surgeries. The animals were closely monitored for 48 hours to provide post-operative care to ensure and maintain animal health and comfort as outlined in the IACUC protocol. Cyclosporine A treatment (5 mg/kg) to prevent mitochondrial permeability transition pore opening in the grafts was administered subcutaneously for a total of 7 days beginning the day before implant surgery. For the ischemia/reperfusion surgery, the rats were anesthetized with an intraperitoneal (IP) injection of 68.2 mg/kg ketamine and 4.4 mg/kg xylazine. A second dose of full strength ketamine/xylazine followed by additional ketamine boosts (20 mg/kg, administered as needed) were used to maintain a surgical plane of anesthesia. During the procedure, the rats were intubated, mechanically ventilated, and maintained on a water-circulating head pad. Core body temperature was monitored at

regular intervals and maintained at 37°C. To induce myocardial infarction, the heart was exposed, and the left anterior descending (LAD) coronary artery was ligated and occluded for 60 minutes, followed by reperfusion and aseptic chest closure. For cardiac patch implantation, patterned vascular constructs (μV + SA) as previously described and control non-patterned constructs (SA) that were gelled in 8 mm diameter x 1 mm height PDMS wells were made with hESC-CMs (12 x 10^6 per mL), noncolored hESC-ECs (3 x 10^6 per mL), and HS-27a (3 x 10^6 per mL) in the bulk in 6 mg/mL. Perfusable cardiac constructs were seeded with noncolored hESC-ECs along the luminal walls and cultured under gravity driven flow with EGM + GFs and media of 25% EGM and 75% RPMI + B27 supplement were placed on top of both μV + SA and SA cardiac construct throughout culture. Both types of constructs were cultured for 4 days *in vitro* to allow initial remodeling and anastomosis of angiogenic sprouts from the channels to de novo tubules from bulk-seeded endothelial cells. One day prior to surgery, cardiac constructs were heat shocked at 42°C for 1 hour. On the day of implant surgery, the rats were anesthetized via inhalation of isofluorane at 5%. The rats were intubated and mechanically ventilated with continued isofluorane supplementation (3%) to maintain a surgical plane of anesthesia. Core body temperature was monitored at regular intervals and maintained with a water-circulating head pad at 37°C. Immediately prior to implantation, the constructs were carefully removed from their housing devices and placed in warm media bath for vascular constructs or pro-survival media on ice for cardiac constructs. Pro-survival media consisted of the following medias at a 1:1:2 ratio: EGM + factors, RPMI + B27 supplement, and pro-survival cocktail containing Matrigel (30x final), 200 nM cyclosporine (Novartis), 100 μM ZVAD (benzyloxycarbonyl-Val-Ala-Asp(O-methyl)-fluoromethyl ketone,

Calbiochem), 50 nM Bcl-X_L BH4 (cell-permeant TAT peptide, Calbiochem), 100 ng/mL IGF-1 (Peprotech), and 50 μM pinacidil (Sigma) in RPMI[191]. For μV + SA constructs, an 8 mm diameter biopsy punch was used to remove the 1 mm thick patterned region of the collagen gel from excess surrounding collagen. Additional 2 mm biopsy punches were created at the inlet and outlet to create structural conduits from the network to the underside of the construct. The constructs were implanted on the epicardial surface of the left ventricle with 8-0 surgical suture at 3 to 4 points of contact. Once the implant was secured, excess blood was dabbed clean followed by aseptic chest closure.

Sample sizes were determined based on pilot studies without rigorous statistical analysis. Experimental groups were assigned randomly in terms of the rat order and construct types for implantation by two independent observers.

4.3.8 *Tissue harvest and retrograde perfusion fixation*

At their experimental endpoint, the rats were euthanized with a chemical overdose of pentobarbital/phenytoin solution (Beuthanasia; 1.5 mL IP injection). Once the animals achieved deep anesthesia but while the heart was still beating, the chest was opened and 50U Heparin was intravenously infused via the inferior vena cava and allowed to circulate for 1-2 minutes to prevent thrombosis in the coronary vessels. Intravenous infusion with supersaturated potassium chloride (KCl) was then used to arrest the heart in diastole followed immediately with excision of the heart. The aorta was cannulated followed by retrograde perfusion with a vasodilator buffer (PBS containing 4 mg/L Papaverin and 1 g/L adenosine) followed by 4% paraformaldehyde perfusion for 10 minutes. Perfusion pressure was maintained at ~100 mmHg. After perfusion fixation, the hearts were

transferred to fresh fixative O/N at 4°C. After overnight fixation, the cannulated hearts were transferred to PBS buffer until lectin perfusion.

4.3.9 *Histological assessment of grafts and lumen quantification*

Following fixation, the hearts were perfused with PBS to wash out remaining fixative followed by perfusion for 10 minutes with an unconjugated *Griffonia simplicifolia* lectin I (GSL I, Vector Labs, 8 µg/mL) in order to label the perfused vasculature (GSL I-bound). The hearts were flushed with PBS, and then sliced into 2 mm-thick sections from the apex for paraffin processing and embedding[100,191]. 4 µm sections were cut and stained for picrosirius red/fast green (to assess infarct size) or subjected to immunohistochemistry[80,100]. Briefly, slides were de-paraffinized and rehydrated followed by enzymatic antigen retrieval (EAR) with proteinase k (Roche, 15 µg/mL in 10 mM Tris/HCl) at 37°C for 20 minutes or heat induced epitope retrieval (HIER) for 20 minutes in boiling Tris/EDTA buffer (pH 9.0) or citrate buffer (pH 6.0). The samples were blocked and permeablized with natural donkey serum (NDS) (Jackson, 10%) and 0.5% Triton X-100 followed by overnight incubation with primary antibodies: goat Ab to GSL I (Vector AS-2104, 1:200), mouse mAb to sarcomeric α-actinin (abcam 9465, 1:50. EAR), and mouse mAb to human β-myosin heavy chain (hybridoma supernatant, ATCC #CRL-2046, full strength, HIER citrate). For immunofluorescent based stains, Alexa Fluor- conjugated secondary antibodies (Invitrogen) were used along with Hoechst (Sigma, 1:250) nuclei counterstain. Apoptotic cells were identified using a Click-iT Plus TUNEL Assay with Alexa Fluor 594 dye (Thermo Fisher). For brightfield peroxidase detection of macrophages or human β-myosin heavy chain (graft size), a biotintylated goat anti mouse

secondary antibody (Jackson, 1:500) was used in conjunction with Vectastain avidin/biotin complex (ABC) kit (Vector labs) and 3,3'-diaminobenzidine (Sigma) followed by routine hematoxylin counterstain to detect nuclei. The density and size of perfused lumens in vascular grafts were quantitated with custom Matlab code to analyze 20X confocal microscopy images of slides stained for GSL I. The graft size was determined by total β-myosin heavy chain+ area relative to total left ventricle area on a 4 μm section containing 4-5 heart sections. The number of cardiomyocytes per area (cardiomyocytes density) was quantified by manual cell counting of β-myosin heavy chain+ cells in 20x confocal microscopy images. Overall and cardiomyocyte-specific viability within the graft was determined by total nuclei or sarcomeric α-actinin+ cell colocalization with TUNEL+ marker determined by particle analysis of 40x confocal microscopy images on ImageJ. All analysis of animal experiments was performed by a blinded observer without knowledge of experimental group.

4.3.10 *Statistical analysis*

Unless otherwise noted, single variable analysis with two-tailed t-test assuming unequal variance was used to determine statistical significance between two samples. All results are presented as mean ± standard error and assumed to be distributed approximately normally. For *in vitro* microvessels, the sample number represents the number of constructs analyzed unless otherwise noted. For *in vivo* experiments, the sample number per group represents the number of animals. Significance was defined as $*p < 0.05$ and $** p<0.01$ for all results.

4.4 Results

4.4.1 Engineering human stem cell-derived microvasculature

To engineer human stem cell-derived microvessels *in vitro*, we first generated endothelial cells, previously called endocardial-like endothelial cells, from a dual reporter RUES2 human stem cell line (mTmG-2a-puro RUES2) using our recently established differentiation protocol[73,74,190]. These stem cells stably express either TdTomato red fluorescent protein or (following Cre-mediated recombination) GFP, allowing us to evaluate vascular remodeling between two separately seeded vascular compartments (**Figure 4.2A-B**). Both mTm- and GFP-expressing hESCs differentiated into endothelial progenitors by differentiation day 5 with greater than 70% populations expressing CD34, a surface marker expressed by both hematopoietic and endothelial populations (**Figure 4.2C-D**)[196]. After an additional week in endothelial culture conditions, endothelial populations arose with greater than 98% purity by day 14 as shown by expression of endothelial junction protein, CD31 (**Figure 4.2E-F**). These cells widely express the endocardial transcription factor, NFATC1, throughout the culture (**Figure 4.3**). We previously demonstrated that these differentiated endothelial cells undergo tubulogenesis when embedded in soft collagen gels and extensive angiogenesis when lined in a 3D engineered microvessel platform[74].

Here, we further developed constructs with enhanced vascularity by combining the lithographically defined network and self-assembled *de novo* small tubes of hESC-ECs[123,124]. Microfluidic channel networks were fabricated in collagen gel matrices with and without bulk-seeded GFP-hESC-ECs. The patterned network was then seeded with mTm-hESC-ECs to form the endothelial-lined lumen (**Figure 4.4A**). After culturing under

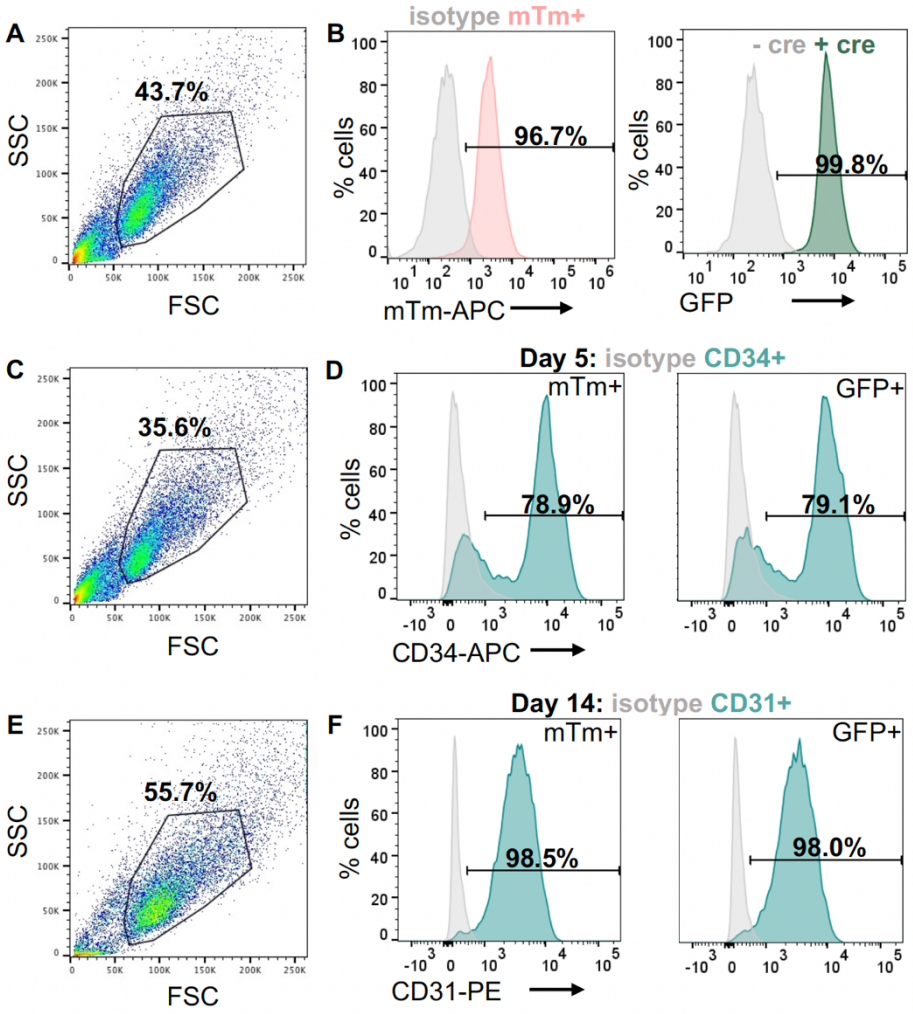

Figure 4.2 Flow cytometry of hESC-ECs from mTm- and GFP-expressing hESCs (A-B) Assessment of TdTomato expression in dual fluorescent hESC reporter line with GFP expression after Cre recombinase-induced recombination and purification. (A) Forward and side scatter used to gate main population. (B) mTm expression (DsRed+, left) before and GFP expression (right) after Cre recombinase-induced recombination and purification with overlay of isotype controls. (C-D) Assessment of Day 5 CD34+ progenitor cells. (C) Forward and side scatter used to gate main population. (D) CD34 expression of mTm-hESC (left) and GFP-hESC (right) differentiations with overlay of isotype controls. (E-F) Assessment of Day 14 CD31+ populations. (E) Forward and side scatter used to gate main population. (F) CD31 expression of mTm-hESC-ECs (left) and GFP-hESC-ECs (right) with overlay of isotype controls.

gravity-driven flow for four or seven days, mTm-hESC-ECs in the lumen formed patent microvessels (μV) that retained the original network geometry and sprouted extensively into the bulk matrix while GFP-hESC-ECs in the matrix underwent tubulogenesis to form

self-assembled (SA) lumens in the surrounding collagen (**Figure 4.4B**). Anastomosis was observed between GFP+ *de novo* tubes and mTm+ endothelium through direct connection at the patterned microvessel or to the smaller angiogenic sprouts (**Figure 4.4C**). Likewise, many GFP-hESC-ECs did not form *de novo* tubes, but rather incorporated directly into the vessel wall of the both the sprouts and the pre-patterned microvessel (**Figure 4.4D**).

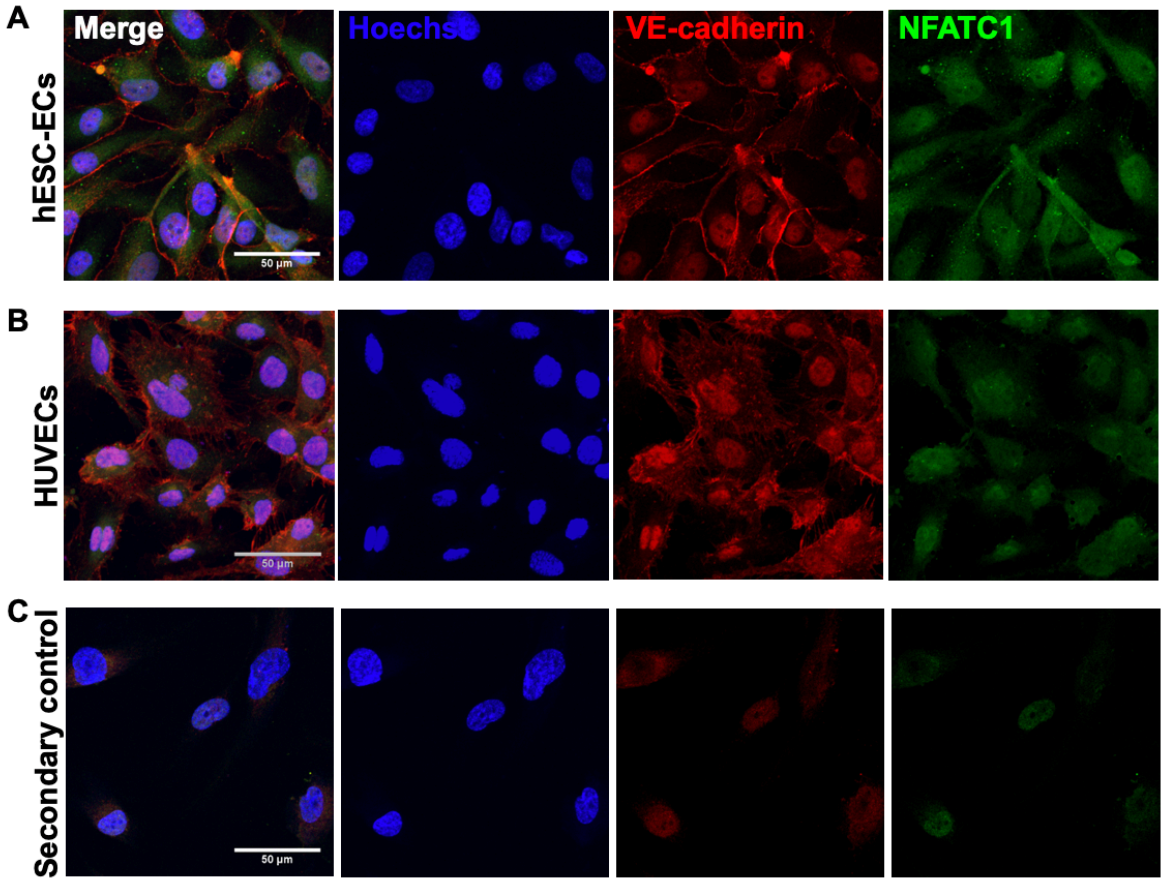

Figure 4.3 Additional characterization of hESC-ECs by NFATC1 staining (A-C) Immunofluorescence images of endothelial cells stained for VE-cadherin (red) and NFATC1 (green). Scale bar, 50 µm. (A) hESC-ECs in culture. (B) HUVECs in culture. (C) Staining control with secondary antibody only. Representative images for (A), (B), and (C) from 2 biological replicates for each condition, with similar results. Hoechst-stained nuclei, blue.

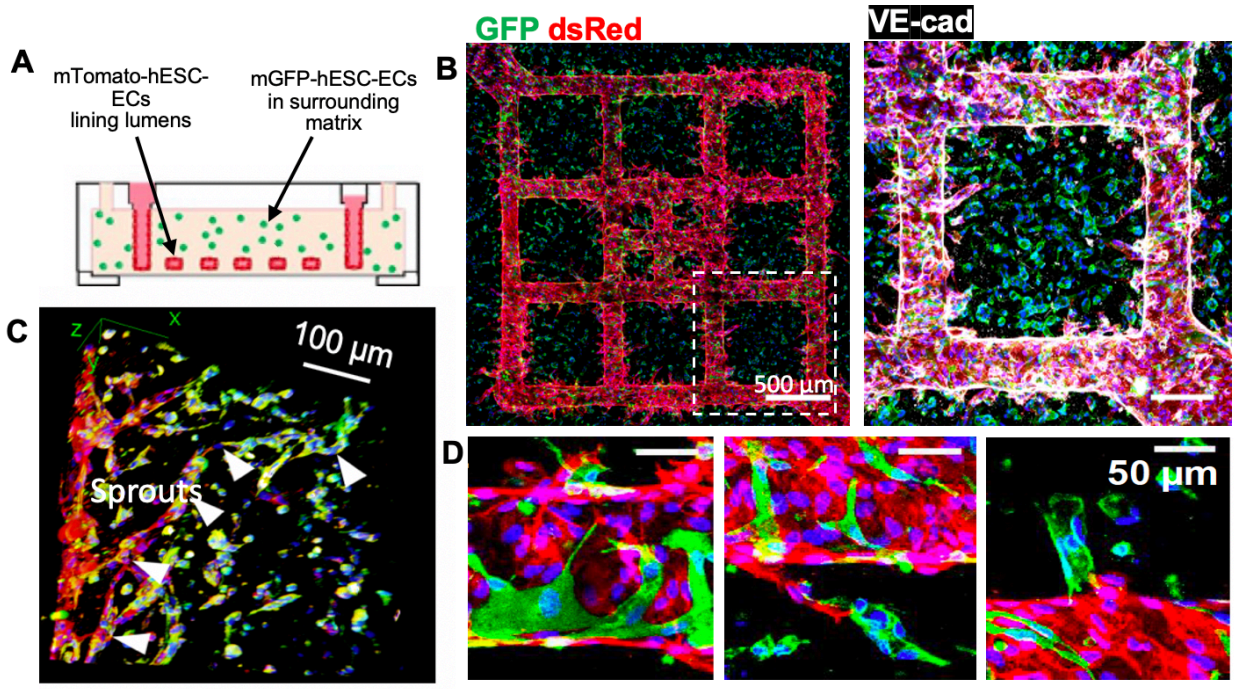

Figure 4.4 *In vitro* anastomosis of hESC-ECs in engineered microvessels (A) Schematic of *in vitro* culture device for µV + SA constructs: mTm-hESC-EC microvessels formed via perfusion and attachment with bulk-seeded GFP-hESC-ECs in the surrounding collagen gel. (B) Left: Maximum intensity projection (MIP) of stitched large image confocal z-stack of µV + SA construct cultured for 4 days and stained for DsRed (red) and GFP (green) to detect mTm- and GFP-expressing hESC-ECs, respectively. Scale bar, 500 µm. Right: Outlined region (white box) stained for DsRed (red), GFP (green), and VE-cadherin (white). Scale bar, 200 µm. (C) 3D view of GFP+ *de novo* lumen integrated with mTm+ microvascular sprout (white arrowheads) stained for CD31 (red) and GFP (green). (D) High magnification images of GFP-hESC-ECs (green) integrated with mTm-hESC-ECs (red) patterned vessel in µV + SA constructs. Scale bar, 50 µm. Scale bar, 100 µm. D4, after 4 days of culture. D7, after 7 days of culture.

4.4.2 *Effects of microvessel remodeling on bulk viability and perfusability*

We analyzed *de novo* lumen density and average lumen size with respect to the distance from the µV wall in µV + SA constructs. GFP+ lumen density was significantly decreased with increased distance from the vessel wall after 7 days in culture with a similar trend after just 4 days (**Figure 4.5A-C**). The density of GFP+ cells near the vessel wall was comparable from day 4 to day 7 suggesting that the decline in EC density at the larger distances (>600 µm) was likely due to lumen regression or cell death rather than

migration (**Figure 4.4D**). Ethidium homodimer-1 staining showed trends towards decreasing cell viability with increased distance from the vessel wall and was lower at day 7 compared to day 4 (**Figure 4.4E**). These findings suggest that perfusion promotes better *de novo* lumen formation which in turn leads to better remodeling and anastomosis.

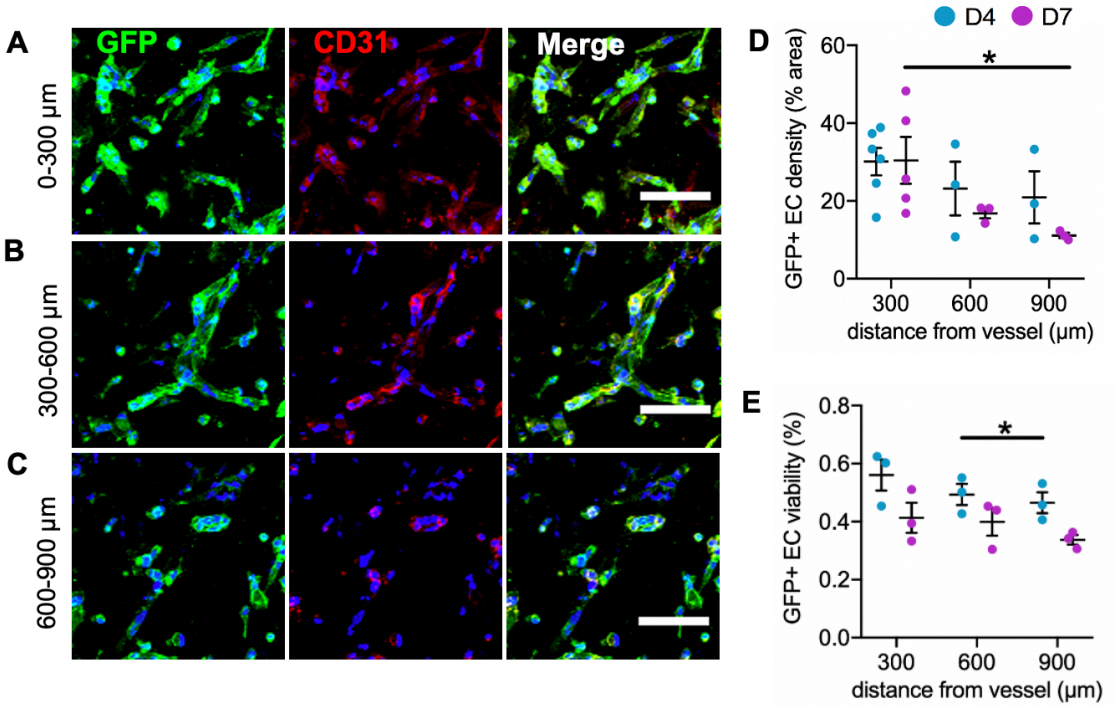

Figure 4.5 Characterization of hESC-ECs in bulk collagen in engineered microvessels (A-C) Maximum intensity projection of confocal z-stack of GFP-hESC-EC tubulogenesis in interstitial collagen matrix of µV + SA device after 7 days of culture at distances 0-300 µm (A), 300-600 µm (B), and 600-900 µm (C) from the patterned microvessel wall stained for GFP (green, left) and CD31 (red, middle). Merged image, right. Scale bar, 100 µm. (D-E) Quantification of GFP-hESC-EC *de novo* lumens in relation to proximity to the patterned vessel in µV + SA constructs after 4 days (blue circles) and 7 days (purple circles) of culture. Data were quantified in for each construct at three distances from the patterned microvessel wall: 0-300 µm, 300-600 µm, and 600-900 µm (x-axis). (D) Quantification of GFP+ EC density (percent area occupied by GFP+ ECs). N = 6,5 biologically independent samples for D4 and D7, respectively. P = 0.032 for D4 at 0-300 µm and 600-900 µm, p > 0.05 for all others (two-tailed t-test). (E) Quantification of cell viability (as percentage of GFP+ ECs) in the bulk matrix. N = 3 biologically independent samples for both D4 and D7. P = 0.046 for 300-600 µm and 600-900 µm for D4, p > 0.05 for all others (paired t-test). Error bars, mean ± SEM. *p < 0.05 determined using two-tailed t-test for (E) and paired t-test for (F). EC, endothelial cell. D4, after 4 days of culture. D7, after 7 days of culture.

We next examined the flow and perfusion characteristics of engineered microvessels and endothelial sprouts in μV only and μV + SA constructs. Fluorescent beads, perfused from the vessel inlets, were observed to immediately fill the endothelial-lined, patterned microchannels before moving into the endothelial sprouts (**Figure 4.6A**). By comparing bead perfusion images with immunofluorescent confocal images, we confirmed that sites of anastomosis between the *de novo* lumens and the patterned μV were patent and perfusable (**Figure 4.6A**). The total perfused area of the constructs increased with time in both μV + SA and μV only groups but was not significantly different between the two groups (**Figure 4.6B-D**). This suggests substantial vascular remodeling occurred over time, but the addition of perfusable anastomotic connections in μV + SA constructs was not yet sufficient to influence the global perfusion dynamics of the constructs. Flow simulation of idealized sprouted vessel networks showed that the addition of sprouts led to higher flow in the vessel networks when the same pressure drop is applied between an inlet and an outlet, indicating a lower flow resistance (**Figure 4.6E**). Together, these data suggest that localized vascular remodeling and anastomotic events decrease the vascular resistance, allowing more efficient perfusion through endothelial sprouts.

4.4.3 *Stem cell-derived microvessels are non-thrombogenic*

Next, we investigated the interaction between blood and hESC-EC-derived engineered microvessels. Citrate-stabilized, ABO-matched whole blood with labeled platelets was perfused from the inlet and into the microvessel lumens. Most blood flowed freely and continuously through the patterned microvessel and exited from the outlet

throughout 20 – 30 minutes of perfusion (>20 minutes) (**Figure 4.7A**). Some blood cells entered the endothelial sprouts and eventually stopped, presumably due to their dead-

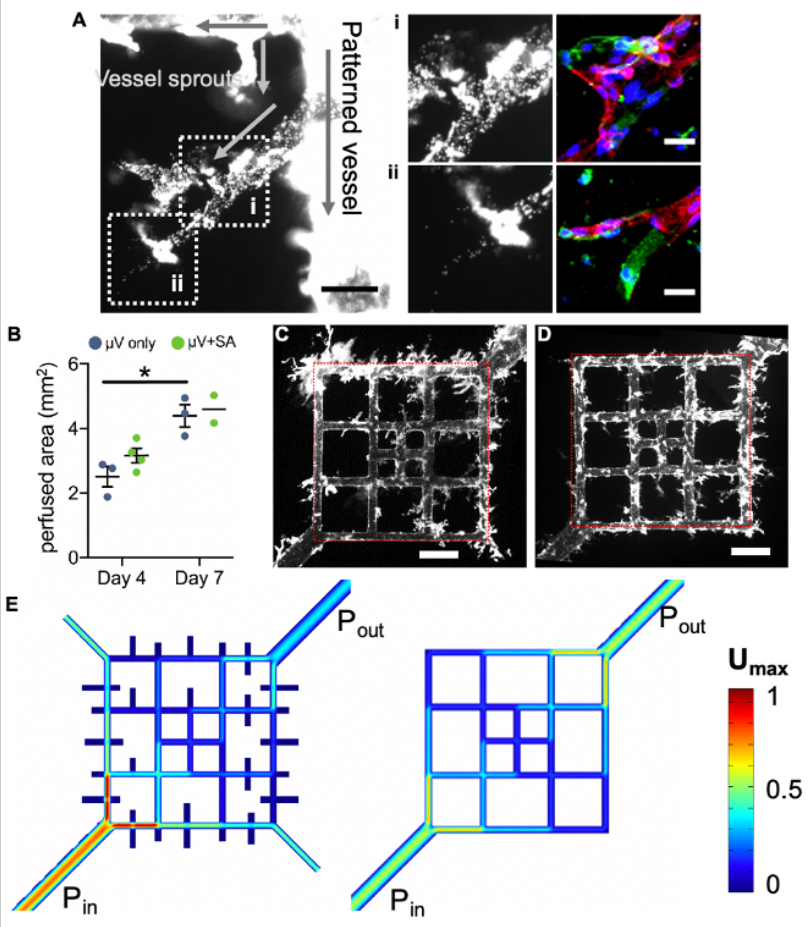

Figure 4.6 Fluorescent bead perfusion of engineered microvessels (A) μV + SA construct with perfused anastomotic connections. High magnification views of outlined regions (i) and (ii) with corresponding *in situ* staining for mTm-hESC-ECs (DsRed+, red) and GFP-hESC-ECs (GFP+, green). Scale bars, 100 μm, 40 μm. (B) Quantification of perfused area in bead perfusion experiments for μV only (blue circles) and μV + SA (grey circles) constructs after 4 days and 7 days of culture. N = 3,4,3,2 biologically independent samples for D4 μV only, D4 μV +SA, D7 μV only, and D7 μV +SA, respectively. p = 0.016 for D4 μV only and D7 μV only, p > 0.05 for all others (two-tailed t-test). (C-D) Large images of bead perfused μV only (C) and μV + SA (D) constructs. For each vessel, the stitched image encompassed a field of view twice the area of the original pattern boundary (red dashed line) or 40% greater in each direction. Scale bar, 500 μm. (E) Flow simulation using COMSOL software for pressure-driven steady-state laminar flow through a square network model either with sprouts (left) or without sprouts (right). Newtonian fluid properties of water and pressure drop of 100 Pa between inlet and outlet were assumed. Model with sprouts has 25% greater area than model without sprouts. For colormap, flow velocity normalized by the maximal velocity (U_{max}) in both networks. The maximal velocity was approximately 25% higher in sprouted vessel model than the original vessel model. P_{in}, inlet pressure. P_{out}, outlet pressure. Error bars, mean ± SEM. *p < 0.05.

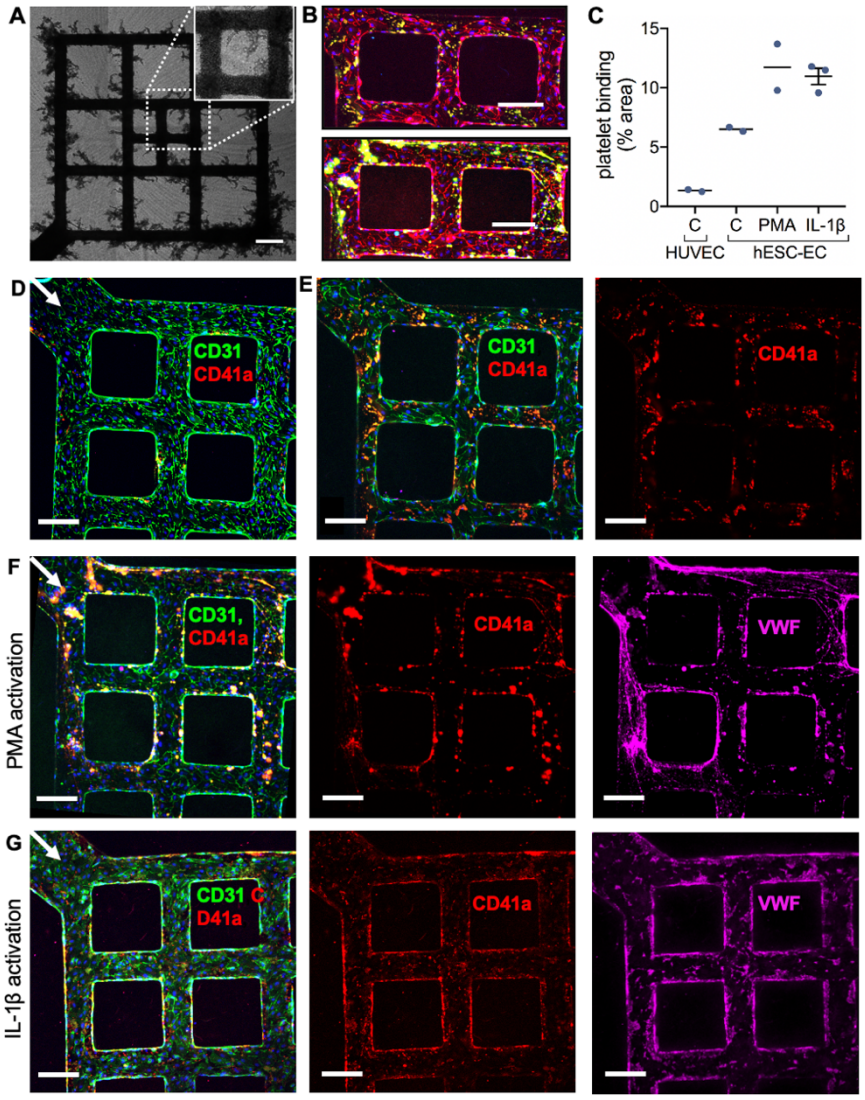

Figure 4.7 Citrated whole blood perfusion of engineered microvessels (A) Brightfield stitched large image of red blood cell-filled pattern and sprouts with magnified view (inset, white dotted boundary) for hESC-EC-seeded μV only constructs after 4 days of culture. Scale bar, 200 μm. (B) Maximum intensity projection of confocal z-stack of constructs with adhered platelets through after 30-minute perfusion and subsequent PBS washes for untreated hESC-EC-seeded constructs (top) and PMA-treated hESC-EC-seeded constructs (bottom) stained for CD31 (red) and CD41a (green). Scale bar, 200 μm. (C) Quantification of platelet adhesion on the vessel wall for constructs seeded with HUVECs in control conditions (C – HUVEC), hESC-ECs in control conditions (C – hESC-EC), and hESC-ECs treated with PMA (PMA – hESC-EC) or IL-1β (IL-1β – hESC-EC). Data is expressed as a percentage of the vessel wall surface area. N = 2,2,2,3 biologically independent samples for C - HUVEC, C - hESC-EC, PMA, and IL-1β, respectively. Error bars, mean ± SEM. (D-G) Maximal intensity projection of confocal z-stacks of constructs after 10 minutes of whole blood perfusion, fixed and stained for CD41a (red), CD31 (green), and VWF (magenta). Constructs seeded with HUVECs in control conditions (D), hESC-ECs in control conditions (E), hESC-ECs with 30-minute treatment of 50 ng/mL PMA prior to whole blood perfusion (F) and hESC-ECs with 30-minute treatment of 1μg/mL IL-1β prior to whole blood perfusion (G). Scale bar, 200 μm. Hoechst-stained nuclei, blue.

end architecture. In regions where sprouts connected two branches of the patterned vessel, individual red blood cells could be seen passing through the newly-formed anastomosis bridges. Few red blood cells clumped or adhered to the vessel throughout the blood perfusion, and these could be completely washed out of the main vessel without obstructing flow. Small amounts of platelets, labeled with antibodies to CD41a, aka platelet-specific glycoprotein IIb, adhered to the vessel wall of engineered microvessels but without formation of large aggregates (**Figure 4.7B**). Subsequent immunofluorescent analysis showed low platelet adherence on the walls of hESC-EC endothelium, and platelets (CD41a) that were adhered were primarily localized to endothelial junctions, although there was somewhat greater adhesion in the hESC-EC constructs than in quiescent HUVEC-seeded microvessels (**Figure 4.7C-E**). When activated with PMA or IL-1β, the hESC-EC microvessels showed increased platelet adhesion after 20 minutes of blood perfusion (**Figure 4.7B,F-G**). These findings demonstrated hESC-EC-formed microvessels are non-thrombogenic and can convert to a thrombogenic state as a physiological response to stimuli.

4.4.4 *Unique microvessel gene expression of vascular development*

To better understand the difference among SA only, μV only, and μV + SA constructs, we collected RNA for transcript profiling using RNAseq analysis for the three groups after three days of culture *in vitro*. The microvessels in the μV only and μV + SA constructs are made from a large grid pattern (13 x 13) with lumen diameter of 125 μm to maximize the vascular surface and RNA yield. Although we predicted that the μV + SA constructs would have an intermediate profile between the μV only and the SA only

constructs, this was not the case. Strikingly, more than 5000 genes were significantly different (fold change > 1.5 and FDR < 0.05) in μV + SA constructs compared to SA constructs, whereas approximately 500 genes were significant when comparing μV vs SA constructs. We performed principle component analysis (PCA), which showed that PC1 separated the μV + SA constructs from the other two, whereas in PC2 the μV + SA constructs were intermediate between the μV only or the SA only constructs (**Figure 4.8A**). The top genes that differentiated the μV + SA constructs from the other two in PC1 (**Figure 4.8B**) include enzymes such as *ENO2*, *ALDOA*, and *ARG2*; peptidases such as *MME* and *MMP9*; glucose transporters such as *SLC2A1* (aka *GLUT1*) and *SLC2A3* (aka *GLUT3*); growth factors such as *VEGFA* and *VEGFB*; and other angiocrine factors such as *ANGPTL4* and *IGFBP5* (**Figure 4.8C**).

Next, we performed Differential Expression Analysis (**Figure 4.9A**) and Gene Ontology terminology analysis (**Figure 4.8D**) which showed that μV + SA, compared to SA condition, had significant upregulation in hypoxia, glycolysis, TNFα signaling via NFKB, mTORC1 signaling, and Epithelial mesenchymal transition (EMT). The comparison of μV vs. SA showed similar patterns, though to a lower extent and with fewer significant genes (**Figure 4.8D and Figure 4.9B**). Canonical pathway analysis showed that the μV + SA constructs had significant upregulation of EIF2 signaling, mTOR signaling, IL-8 signaling, EMT regulation, glycolysis, HIF1α signaling, as well as signaling of VEGF, endothelin-1, Wnt/β-catenin, Neuregulin, and CXCR4, and downregulation of PTEN, Notch, and apoptosis signaling (**Figure 4.9C**). The functional annotation associated in these analyses showed increased function in development of endothelial tissue, endothelial cell proliferation, cell assembly, and DNA binding and interactions.

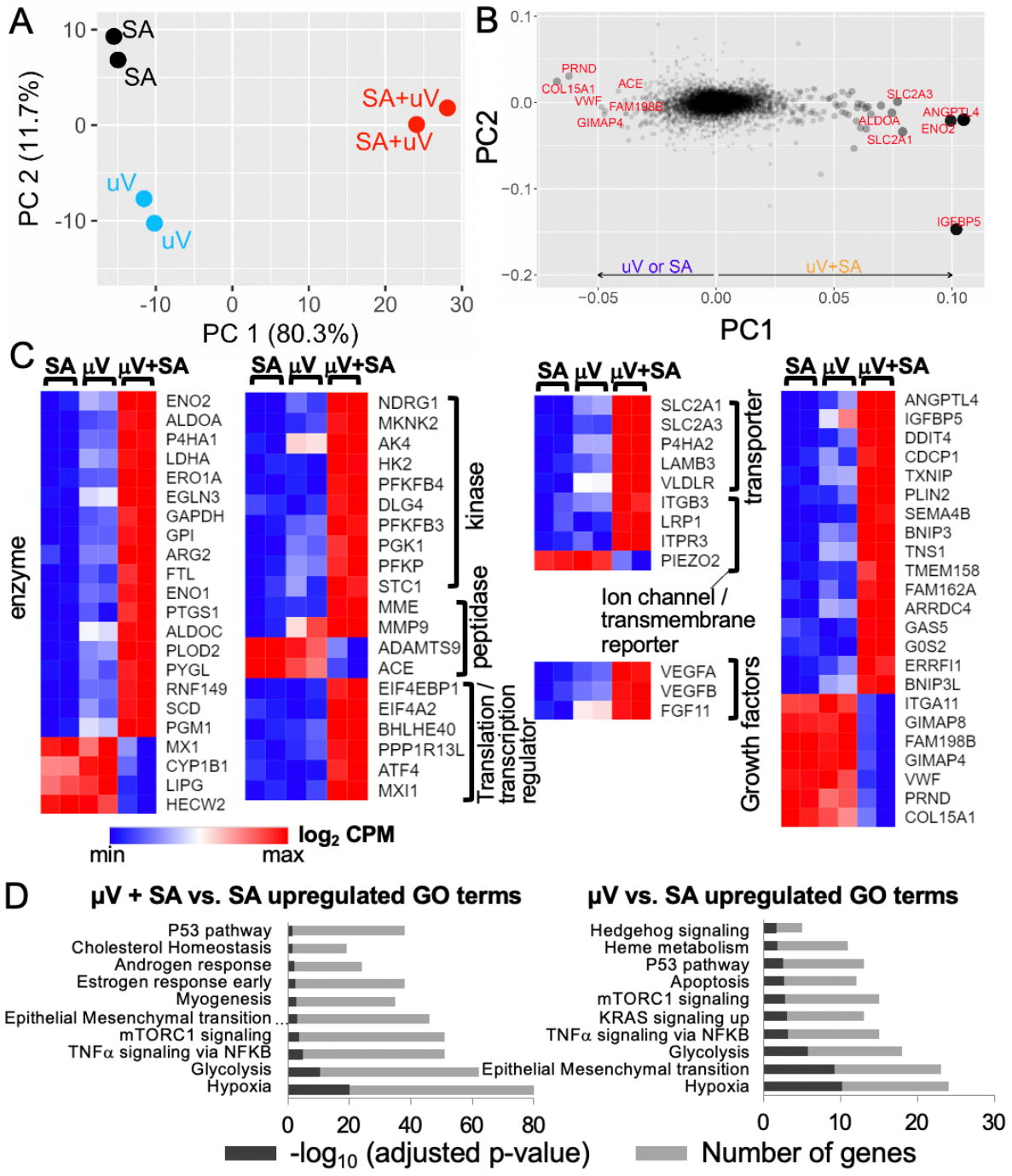

Figure 4.8 Global RNA sequencing reveals differential gene expression profiles among SA, μV only, and μV + SA constructs after 3 days of culture *in vitro* (A) 2D principle component analysis (PCA) of RNA sequencing data for cultured constructs showing clustered group for each condition. (B-C) Top genes contributing to PC1: (B) Size of the circle is proportional to the contribution. (C) Heat map of top 75 genes (log_2 CPM) contributing to PC1 in categorized functions. Colormap normalized to minimum and maximum expression. Red, high expression. Blue, low expression. (D) Gene ontology terminology analysis (GO) showing different gene clusters for μV + SA vs. SA (left) and μV vs. SA (right). Each sample is 2 constructs pooled. CPM, counts per million.

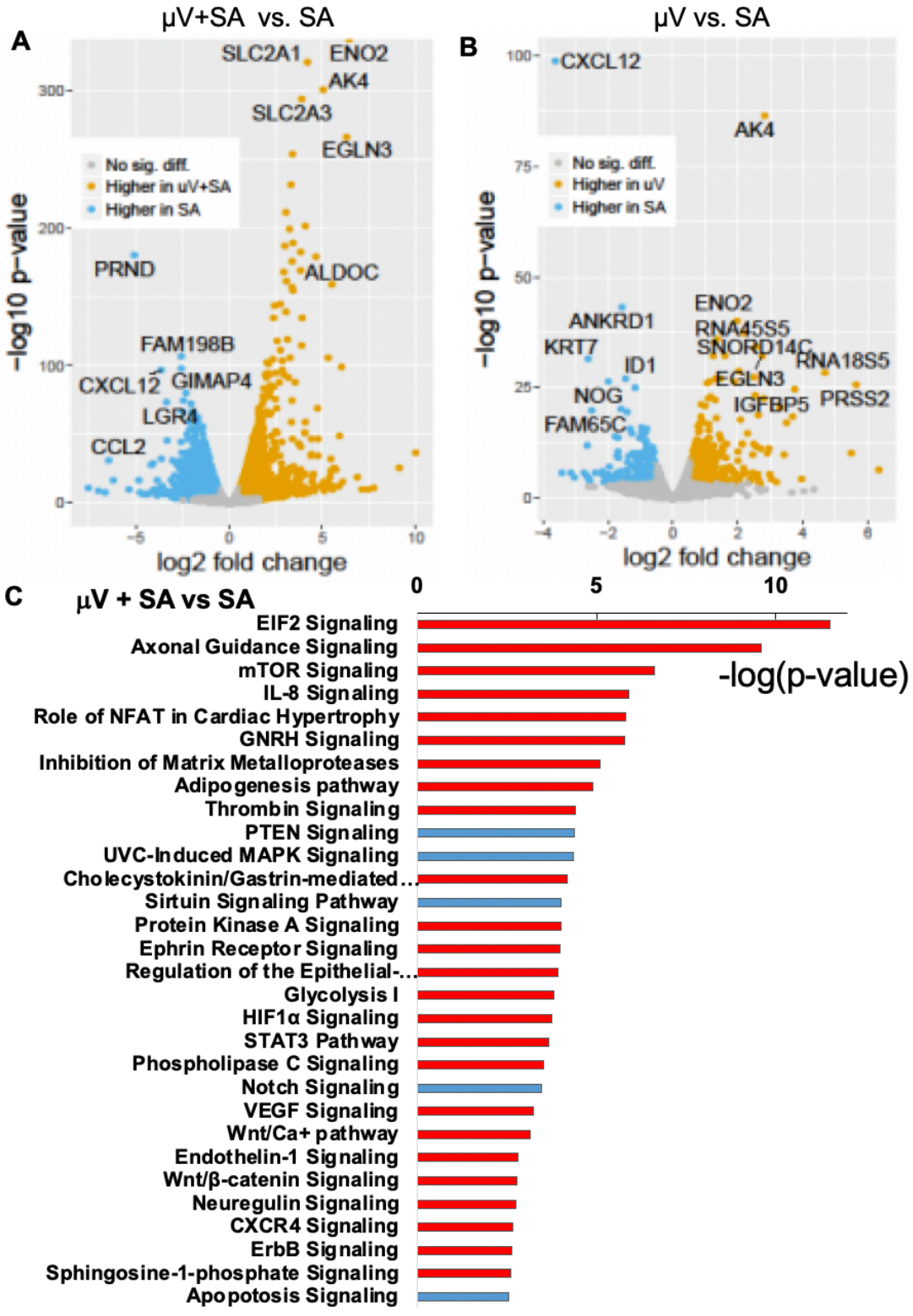

Figure 4.9 Additional gene expression analysis for SA, μV only, and μV + SA constructs after 3 days of culture *in vitro* (A-B) Volcano plots showing different gene expression comparing μV + SA constructs vs. SA constructs (A) and μV only vs. SA only constructs (B). (C) Canonical pathway analysis for comparison between μV + SA and SA only constructs.

These expression analyses suggest that μV + SA constructs are significantly different compared to SA only or μV only ones in terms of endothelial phenotypes and vascular development, which may change their host integration *in vivo* as well.

4.4.5 *Sustained perfusion of hPSC-EC microvessels*

As the goal of incorporating vasculature into engineered tissues is to increase perfusion to the center of the tissue, we next assessed the ability of hESC-EC-derived microvessels to withstand continuous flow. After 2 days of culture to allow full adhesion and endothelial cells, μV only constructs made from a large grid pattern (13 x 13) were attached to an ELVEFLOW pressure-driven perfusion system using tubing then perfused with EGM + GFs (**Figure 4.10A**). The computer-controlled ELVEFLOW uses feedback from microfluidic flow sensors to continuously adjust a pressure head and also allows the user to define complex flow profiles, making changes to flow rate less sudden than syringe pump perfusion. While hPSC-EC-derived microvessels cultured under our usual conditions of gravity-driven flow have high endothelial patency, hPSC-EC-derived microvessels were not able to withstand continuous perfusion of 2 μL/min (~1 dyne/cm^2) for a 24-hour period (**Figure 4.10B-C**). Interestingly however, hESC-EC microvessels maintained their integrity when intermittently perfused with 2 μL/min for 1 hour followed by 0.1 μL/min for 3 hours in a cyclic pattern over a 24-hour period (**Figure 4.10D**). Quantification of area coverage reveals high patency in both gravity-driven (91.3 ± 5.1 %) and intermittent (84.5 ± 6.1%) flow regimes and low patency in a continuous flow regime (10.4 ± 3.2%) (**Figure 4.10E**). As a comparison, we also generated μV only constructs with HUVECs and saw that HUVECs remain patent under continuous perfusion at 2

μL/min (**Figure 4.10F-G**). These results indicate the hESC-EC-derived microvessels are highly sensitive to flow, however, this sensitivity has a temporal component with duration of high flow pulses being a critical factor.

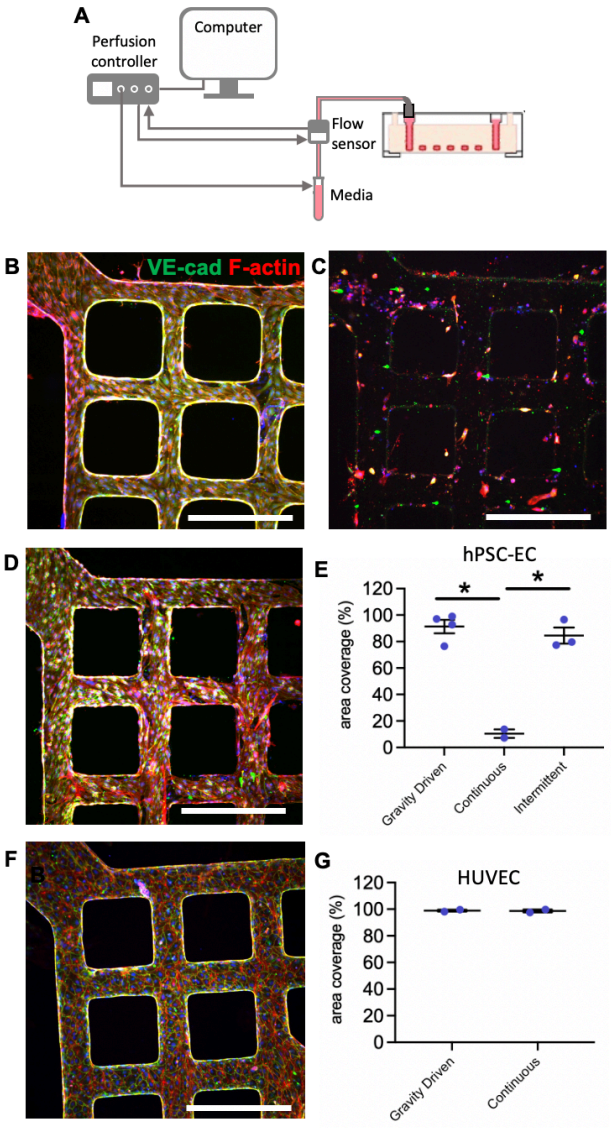

Figure 4.10 Sustained perfusion of hESC-EC and HUVEC microvessels. (A) Schematic of microvessel attached to pressure-driven perfusion system. (B-D) Inlet of hESC-EC microvessels after 24-hour culture by (B) gravity-driven perfusion, (C) continuous perfusion (2 μL/min) and (D) intermittent perfusion (2 μL/min for 1 hour, 0.1 μL/min for 3 hours). VE-cadherin (green); F-actin (red). (E) Quantification of vessel area coverage under different flow regimes for hESC-EC microvessels. (G) Inlet of HUVEC microvessels after 24-hour culture by continuous perfusion (2 μL/min). (F) Quantification of vessel area coverage under different flow regimes for HUVEC microvessel. Error bars, mean ± SEM. *p < 0.05 determined using two-tailed t-test.

4.4.6 Pre-patterned cardiac grafts survived implantation and were perfused

To determine the benefit of increased early perfusion of engineered microvessel grafts, we implanted both perfusable (μV + SA) and non-perfusable (SA) cardiac constructs containing additional hESC-derived cardiomyocytes (hESC-CMs) onto infarcted athymic Sprague-Dawley rat hearts. The cardiac constructs contained hESC-CMs and human bone marrow-derived stromal cells HS-27a in addition to hESC-ECs at

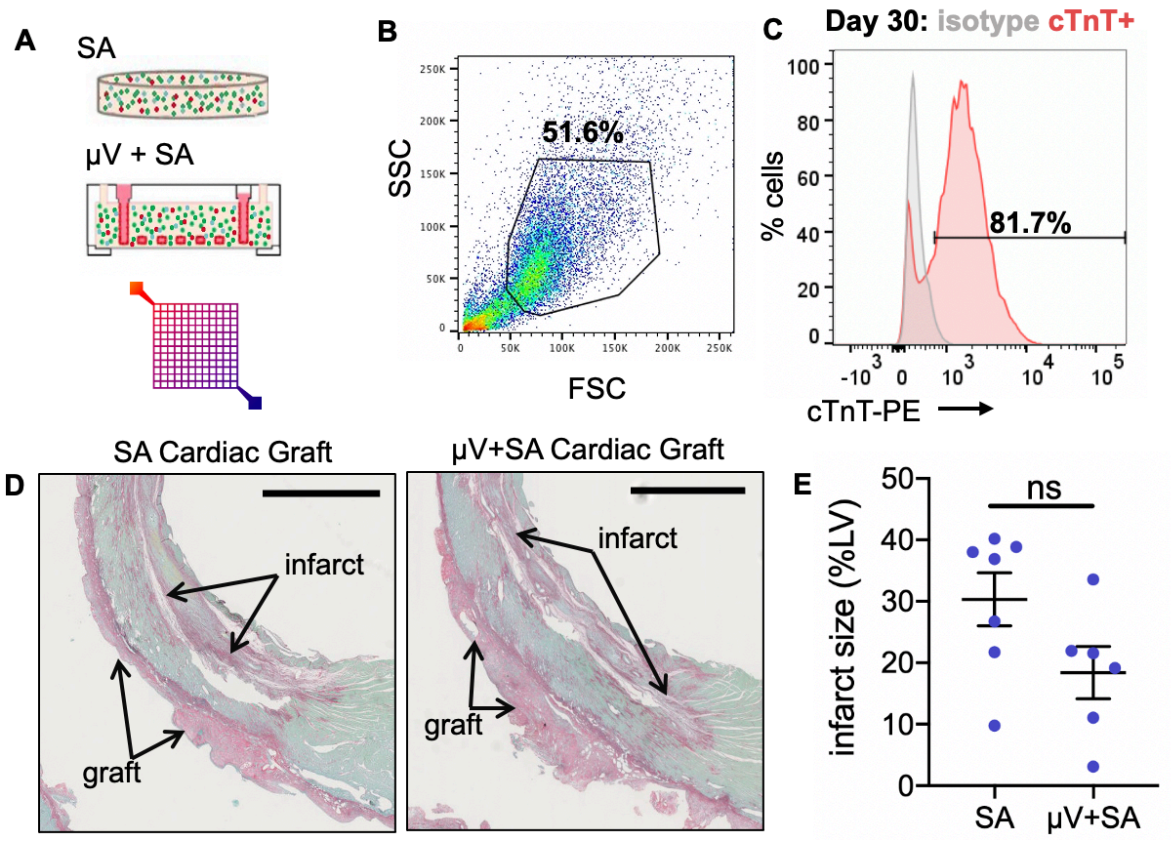

Figure 4.11 Generation of cardiac patches and assessment of ischemia/reperfusion induced myocardial injury (A) Schematics of SA (top) constructs and μV + SA (middle) constructs with large grid-like geometry used for network patterning (bottom). (B-C) Flow cytometry assessment of Day 30 cTnT+ cardiomyocyte population from hESC differentiation. (A) Forward and side scatter used to gate main population. (C) cTnT expression of hESC-CMs with overlay of isotype controls. (D) Picrosirius red/fast green stain to SA (left) and μV + SA (right) grafts. Collagenous regions, such as the infarct and grafts, stain red/purple and healthy tissue regions stain green. Scale bar, 2 mm.(E) Quantification of infarct size as a percentage of left ventricle area. N = 7,6 biologically independent animals for SA and μV + SA, respectively. $p > 0.05$ (two-tailed t-test). Error bars, mean ± SEM. ns = non-significant ($p > 0.05$).

a ratio of 4:1:1 respectively in bulk matrix and were 8 mm in diameter with 1 mm thickness (**Figure 4.11A**). A large grid pattern (13 x 13), same as that used in RNAseq studies, was used for for μV + SA constructs and hESC-ECs were also seeded and cultured under perfusion within the pre-patterned lumens as described earlier (**Figure 4.11A**). All hESC-CM populations used for cardiac constructs had cardiomyocyte purity >70% as indicated by expression of cardiac marker cTnT (**Figure 4.11B-C**). After 4 days of culture, spontaneous beating was detected in both μV + SA and SA cardiac constructs. At 5 days post-implantation, hearts were excised, and histological analysis was performed. Both groups had similar infarct sizes (**Figure 4.11D-E**). To assess hESC- CM graft retention, we stained for human-specific β-myosin heavy chain (β-MHC) (**Figure 4.12A-B**). The density of β-MHC+ cells was significantly greater in the μV + SA cardiac grafts (194 ± 31 cells/mm^2) than the SA grafts (85 ± 12 cells/mm^2). The β-MHC+ graft size, normalized by the left ventricle size, was measured to be greater, however not significantly, in μV + SA grafts than SA grafts (0.16 ± 0.05% and 0.11 ± 0.02% respectively; p = NS, two-tailed t-test) (**Figure 4.12C**). This suggests perfusable microvessels enhanced hESC-CM remodeling, which could potentially improve cardiac engraftment and function long term. The total perfused vessel density was also significantly greater in μV + SA cardiac grafts (320 ± 53 vessels/mm^2) than in SA cardiac grafts (179 ± 24 vessels/mm^2) (**Figure 4.12D**). Additionally, the average lumen size was greater, though not significantly, in μV + SA grafts (75 ± 32 μm) than in SA grafts (40 ± 8 μm) (**Figure 4.12D**). We next sought to determine whether cells within the grafts were viable and performed a TUNEL assay to mark apoptotic cells (**Figure 4.13A**). Both μV + SA and SA grafts had low levels of apoptotic cells (1.1 ± 0.5% and 1.9 ± 0.5% respectively; p = NS, two-tailed t-test) **(Figure**

4.13B). To specifically determine hESC-CM viability, we performed a TUNEL assay with an α-actinin co-stain to label cardiomyocytes. We were unable to identify any TUNEL+/α-actinin+ cells, indicating that remaining cardiomyocytes had high viability and possibly passed the peak cell death at 5-days post implantation (**Figure 4.13C**)[197]. These findings

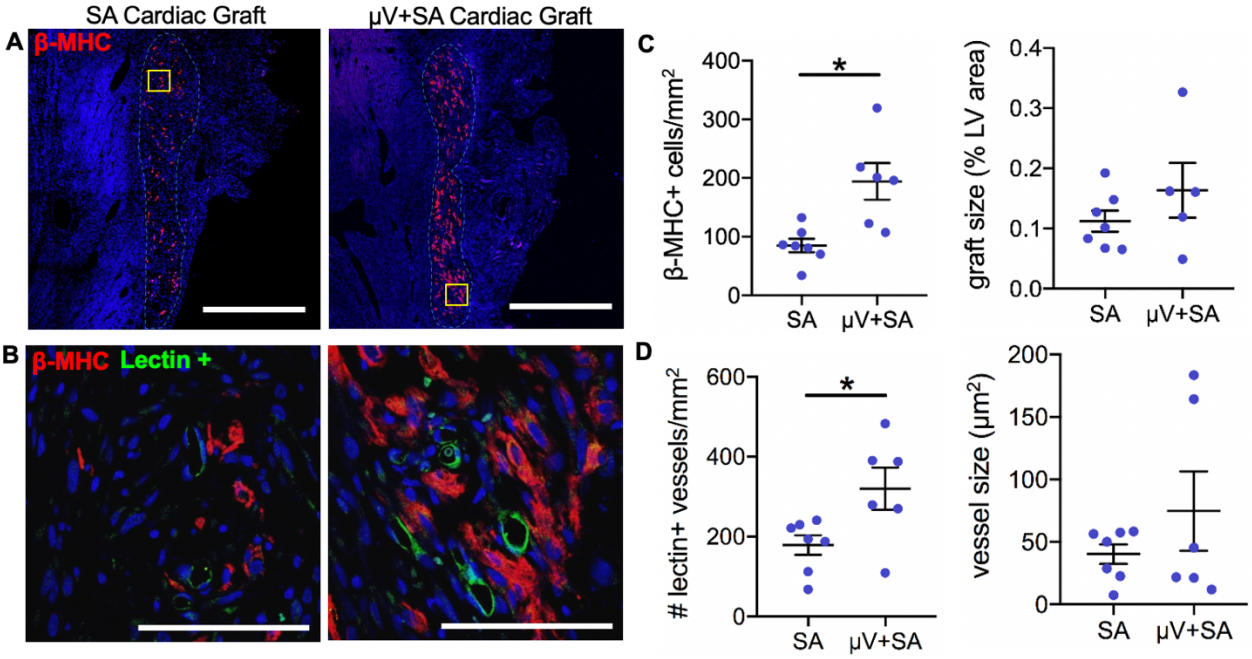

Figure 4.12 Cardiomyocyte engraftment and host vascular integration of cardiac constructs in rat ischemia/reperfusion model 5 days post implantation (A-B) Immunofluorescent stained paraffin sections of SA (left) and μV + SA (right) cardiac grafts: (A) Whole graft section containing hESC-CMs (β-MHC, red). Gray dotted line outlines graft tissue. Scale bar, 1 mm. (B) High magnification images of boxed region in A (yellow box) with hESC-CMs (β-MHC, red, bottom right) and perfused vessels (Lectin+, green, bottom left). Merged, top. Scale bar, 100 μm. (C) Quantification of cardiomyocyte density (number of β-MHC+ cells per mm^2) and β-MHC+ graft size (% LV area). N = 7,6 biologically independent animals for SA and μV + SA, with one animal with μV + SA graft excluded from graft size calculation due to partial graft removal during tissue processing. $p = 0.015$ for density, $p > 0.05$ for graft size (two-tailed t-test). (D) Quantification of vessel density (number of vessels per mm^2) and average vessel size for all perfused vessels (Lectin+) in the cardiac grafts. N = 7,6 biologically independent animals for SA and μV + SA, respectively. $p = 0.046$ for vessel density, $p > 0.05$ for vessel size (two-tailed t-test). Hoechst-stained nuclei, blue. Data collected from at least two confocal images of randomly selected regions per sample. Images analyzed by a custom lumen identifying code for vessel density and size. Error bars, mean ± SEM. *$p < 0.05$ determined using two-tailed t-test. β-MHC, beta-myosin heavy chain.

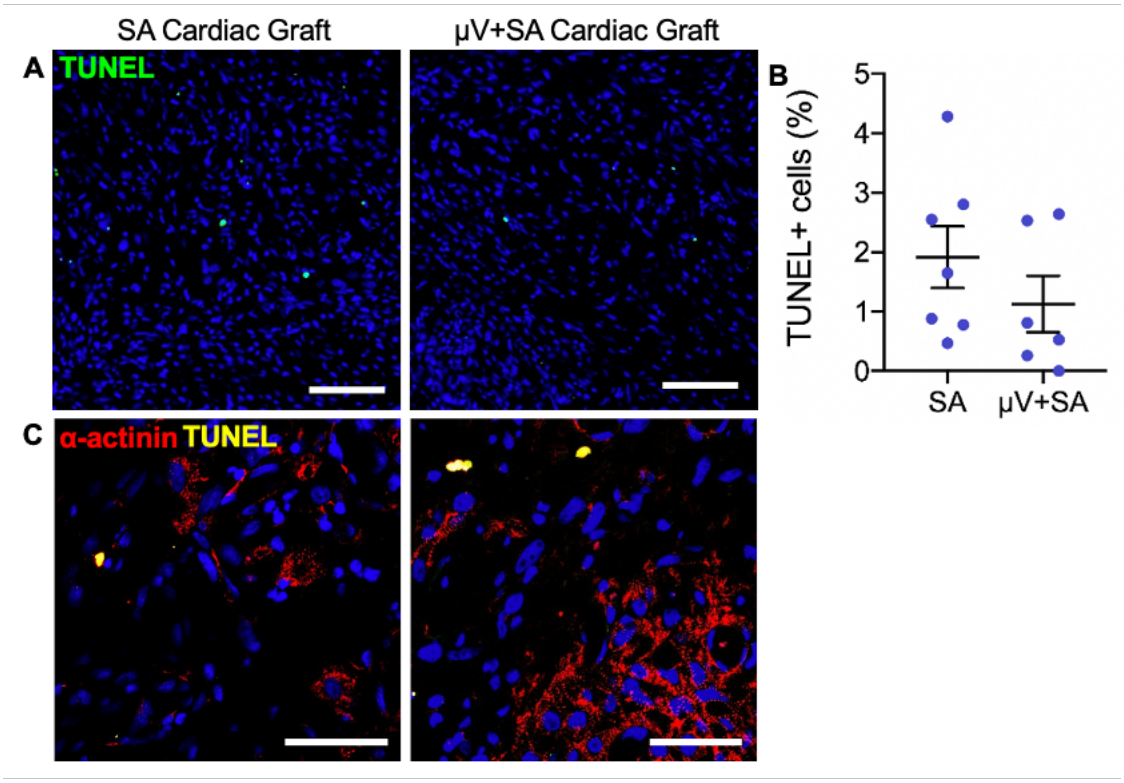

Figure 4.13 Apoptosis in cardiac constructs in rat ischemia/reperfusion model 5 days post implantation (A) TUNEL assay for apoptotic cells (TUNEL, green) on paraffin sections of SA (left) and μV + SA (right) cardiac grafts. Scale bar, 100 μm. (B) Quantification of apoptotic cells (TUNEL+) as a percentage of all cells (human and host) in the graft. N = 7,6 biologically independent animals for SA and μV + SA, respectively. $p > 0.05$ (two-tailed t-test). Error bars, mean ± SEM. (C) TUNEL assay for apoptotic cells (TUNEL, yellow) on paraffin sections of SA and μV + SA grafts with co-stain for cardiomyocytes (α-actinin, red). Scale bar, 50 μm.

demonstrate the beneficial role of a perfusable, patterned vascular network in cardiac graft remodeling, which could lead to enhanced engraftment and function long term.

4.5 Discussion

Vascularization and rapid host integration remain as critical challenges for engineered cardiac tissues, and for their successful translation to the clinic for heart regeneration. While considerable progress has been made to generate pre-vascularized

tissues, efficient perfusion has not been achieved *in vitro* or *in vivo* when implanted on injured myocardium. In this study, we successfully engineered highly vascularized constructs from stem cell derived endothelial cells by incorporating self-assembled capillary tubes around a patterned and perfusable microvascular network. We demonstrated that pre-patterned perfusable microvessels underwent extensive remodeling and anastomosis with *de novo* capillary tubes *in vitro*, and the resulting perfusable vascular construct systemically integrated with host vasculature after implantation better than non-patterned, non-perfusable constructs.

Our study demonstrated the successful use of hESC-ECs, and potentially patient-derived induced pluripotent stem cells (hiPSCs), as the vascular cell source in engineered tissue constructs. The use of a patient-specific autologous cell source would bypass the immunogenic risks associated with clinical transplantation[187]. In addition, the use of endothelial cells at the same developmental stage as the cardiomyocytes may provide important signaling to promote cardiomyocyte maturation and tissue function. Our work took a step beyond endothelial cell differentiation from hESCs, and further built 3D microvessels that allow for robust culture and phenotype maintenance under flow. We demonstrated and utilized their angiogenic, tubulogenic, and nonthrombogenic properties towards engineering highly vascularized constructs for tissue engineering applications.

Our studies uncovered that perfusion facilitates anastomosis and vascular remodeling *in vitro*. We showed that anastomosis occurs between *de novo* capillary tubes and pre-patterned vascular conduits and that bulk-seeded endothelial cells directly incorporate into the microvascular endothelium, leading to increased flow velocity and decreased vascular resistance. This phenomenon appears similar to the incorporation of

endothelial progenitor cells into active sites of angiogenesis in animal models of ischemia[198]. Transcriptional analysis further revealed unique gene clusters towards upregulated signaling in hypoxia, glycolysis, and vascular development in anastomosed constructs. These studies demonstrate the formation of a highly remodeled perfusable vascular network with numerous anastomotic connections, and more importantly, these vessels are capable of carrying blood without blockage.

Our implantation studies quantitatively demonstrated that perfusable vascularized grafts integrated significantly better than non-perfusable self-assembled vascular grafts. Several studies have shown that prior vascular patterning in grafts promotes better overall integration, presumably as a result of topographical cues that provide guidance to the invading host blood vessels[107,188,199–201]. Given this extensive remodeling process, it would be interesting to determine if the precise geometry of the vasculature affects its ability to integrate. Here we used a grid-like pattern to fabricate the microvessels in order to maximize the perfusion area with multiple vascular branches. In future applications, the network structure could be generated with aligned parallel vessels or acute angle branches to better mimic coronary structure. Juhas *et al*. recently demonstrated that the aligned structure of muscle fibers can provide structural cues and guidance to invading host vasculature[202]. In the context of the heart, it is possible that the presence of oriented cardiomyocytes along with patterned parallel vasculature could help guide coronary infiltration to better mimic myocardial structure. In our vascularized grafts, the patterned vasculature provides support for the surrounding cardiomyocytes, suggesting the important role of vascular patterning and perfusion in tissue remodeling and host integration.

In addition to our studies of implantable cardiac grafts, we previously conducted studies with endothelial cell only grafts. In these studies, we exploited OCT-based imaging technology in the intact heart to assess the perfusion dynamics in grafts under physiological pressure, which had not been achieved previously. The live heart poses a major challenge for assessment of coronary flow due to large motion artifacts. Our use of diastolically arrested, fixed hearts allowed for precise control of the applied pressure at physiological level for flow measurement while eliminating the motion artifacts associated with the beating heart. While this is admittedly different from a living, beating heart, it does present a snapshot of the heart's microcirculation at the peak phase of coronary perfusion. This, in combination with Intralipid perfusion to mimic blood flow and generate angiograms, made it possible to obtain the 3D vascular structure, flow velocity, and perfusion rate of the vasculature down to the capillary scale in tissue grafts implanted on infarcted hearts. More importantly, our approach allowed for unambiguous distinction between the host and graft with respect to their tissue structure and perfusion dynamics. Our patterned vascular grafts at 5 days post implantation demonstrated comparable perfusion velocities (0.72 mm/s in 20 - 30 μm sized vessels) to those in the non-infarcted myocardium as well to previously reported values in similar sized venules and arterioles in living tissues[200,203,204].

Despite a normal range of velocities displayed in vessels within patterned vascular grafts, these newly integrated vessels do not yet structurally resemble proper coronary structure. The graft vessels are more sparsely distributed with less organized structures compared to the dense, aligned vasculature displayed by their healthy counterparts. Surprisingly, the overall structure of perfused graft vessels did not retain the original

geometry of the network pattern, but the pre-patterning did enhance vascular density and perfusion. Our histological assessment suggested that although the implanted human endothelial cells did contribute to the newly connected and perfused vessels in the graft, most perfused vessels originated from the host. In conjunction with the results from our *in vivo* studies with implantable perfusable cardiac grafts, this suggests that the pre-patterning determines host vessel infiltration patterns and leads to better vascular structure and function.

Our work demonstrated improved integration in the heart using patterned perfusable vasculature and demonstrated its contribution to support cardiac grafts after implantation. This work took important steps towards addressing several of the key challenges associated with cardiovascular tissue engineering, namely vascularization and host integration, and will have numerous implications in future cardiac tissue engineering and regenerative approaches.

Chapter 5. Engineer thick tissues with multilayer, perfusable vasculature

5.1 Abstract

Fabrication of large-scale engineered tissues requires extensive vascularization to support tissue survival and function. Here, we report a modular fabrication approach to generate 1.5-mm thick tissues with large, three-dimensional, perfusable networks of endothelialized vasculature using soft lithography and stacking of collagen membranes. *In vitro*, our perfusable vascular networks exhibit angiogenic remodeling and evenly distributed perfusion while maintaining their patterned, open-lumen architecture. Towards regenerative medicine applications, we engineer thick tissues with stem cell-derived endothelial cells and demonstrate increased gene expression indicative of vascular development and angiogenesis when compared to constructs with non-perfusable, self-assembled vasculature. Upon implantation onto infarcted rat hearts, perfusable stacked vascular networks attain greater host vascular integration at a 5-day timepoint than self-assembled controls as indicated by 2.5-fold greater perfused vascular density measured by histological analysis and 5-fold greater perfusion measured by optical microangiography. This approach to engineering vascularized tissues can be easily tuned to achieve different network geometries with increasing vascular complexity. By demonstrating that thick, perfusable tissues with dense vascularization throughout can be fabricated through modular assembly, this work will advance the field of vascular engineering and enable creation of large-scale, highly metabolic engineered tissues.

5.2 Introduction

Tissue engineering has emerged as a promising approach to generate biomimetic constructs for disease modeling, drug development, and *in vivo* regeneration. Consequently, engineered tissues have been made to imitate a wide range of complex organs including kidney, liver, heart, and lung[205]. By replicating three-dimensional features of the heart, cardiac tissues have the potential to combat cardiovascular disease, the leading cause of death worldwide[32,84]. One of the most significant contributors to the burden of cardiovascular disease is myocardial infarction (MI), which frequently results in functional decline and eventual heart failure[38,40]. Organ failure, like that which occurs after MI, has motived the generation of implantable tissues that can substitute function or provide regenerative benefit for many different organs[206]. However, generation of large-scale engineered tissues will depend on adequate vascularization to meet the metabolic needs throughout the construct.

Early work on vascularization in engineered tissues utilized endothelial cells to form self-assembled vascular networks within 3D hydrogels[83,97,102,103]. Although the addition of endothelial cells has been shown to improve maturation and tissue function[102,104,105], these early attempts at vascularization lacked perfusion. Consequently, diffusion limits constrained the thickness of tissues to approximately 500 μm during *in vitro* culture. Upon implantation, tissues with self-assembled vascular networks slowly and incompletely integrate with host vasculature[106], which is insufficient for supporting implantation of thick, highly metabolic tissues. Strategies like patterning of endothelial cells into non-perfusable cords or allowing for extensive vascular remodeling prior to implantation have been shown to improve integration with host vasculature[107,110]. Yet, the

challenges of *in vitro* culture will remain for non-perfusable tissues, limiting their scalability.

To overcome this issue, recent efforts including our own have been made to incorporate perfusable vasculatures into engineered tissues. Many approaches towards perfusable vascularization have emerged including anastomosis-based remodeling[113,115], needle subtraction[111], soft lithography[117], subtractive sacrificial scaffolds[116,121,207], and 3D printing[118–120]. However, immediately perfusable tissues with high vascular density have not been achieved in a cell compatible material as will be necessary to support highly metabolic tissues. While 3D printing has recently garnered much attention, its application has primarily been limited to fabrication of large caliber and low-density vasculature[122]. Generation of complex, small diameter vascular networks using 3D printing approaches will be restricted by long printing times without perfusion and material limitations. Similar challenges in achieving vascular complexity and accomplishing immediate and maintained perfusion within a cell compatible material have hampered the application of numerous other vascularization techniques for large-scale tissue fabrication.

We have previously engineered perfusable vasculature with planar geometry using soft lithography patterning of collagen[123,124]. We have shown that this approach results in immediately perfusable vasculature while enabling vascular and tissue remodeling, making this approach suitable for generation of functional engineered tissues[124,125]. Further, we have demonstrated that our microvessel constructs promote rapid host vascular integration after implantation onto infarcted rat hearts[126]. While these results indicate the usefulness of our microvessel platform, new techniques are needed for thick perfusable tissue fabrication.

In this aim, we engineer 1.5-mm thick, perfusable, highly vascularized tissues by stacking multiple layers of patterned collagen membranes to create a large network of perfusable, endothelial-lined lumens within a matrix that can be remodeled. We combine confocal microscopy, scanning electron microscopy, optical coherence tomography, transcriptional profiling, and graft implantation onto infarcted rat hearts to present the structure, perfusion, and host vascular integration of the thick vascularized networks. We demonstrate that our technique allows for robust fabrication of large tissues that have the necessary stability to maintain perfusion while supporting vascular remodeling *in vitro*. We show that our highly vascularized stacked tissues have gene expression towards vascular development when compared to non-perfusable tissues and that gene expression is minimally affected by adding more layers of perfusable vasculature to the tissue. Further, stacked vascular networks increased host vascular integration after implantation at an early timepoint, illustrating the benefit of our technique for *in vivo* applications. Overall, our work demonstrates that modular assembly of individually constructed pieces can be used to create thick, highly vascularized tissues. This work will facilitate large-scale fabrication of highly metabolic tissues with consistent vascularization throughout, enabling the next generation of complex engineered tissues.

5.3 Scientific Methods

5.3.1 *Cell culture and hESC-EC differentiation*

Human umbilical vein endothelial cells (HUVECs) and human embryonic stem cell derived endothelial cells (hESC-ECs) were used in this study. HUVECs were cultured in EGM-2 and used at passage 5-6. hESC-ECs were differentiated from a genetically

modified mTmG-2a-Puro dual-reporter line of RUES2 (Rockefeller University, NIH 0013) hESCs[190]. The hESCs were only used in their untreated state in which the mTmG-2a-Puro transgene causes the cells to stably expresses tdTomato red fluorescent protein (mT). Undifferentiated hESCs were maintained on Matrigel (BD Biosciences) in mTeSR Plus (Stemcell Technologies). To differentiate the hESCs into hESC-ECs, cells were treated with high Activin A and low BMP4 as previously described[73,74]. Briefly, hESCs were replated into Matrigel coated 24-well plates at a density of 200K/well in mTeSR Plus with 10 μM Rock inhibitor (Stemcell Technologies) and 1 μM CHIR-99021 (Cayman Chemical). After 24 hours, hESCs were induced in RPMI (Gibco) with 100 ng/mL Activin A (R&D), 1x Matrigel and 1x B-27 Supplement, minus insulin (Thermo Fisher). The time of induction is referred to as day 0. 18 hours after induction, the media was changed to RPMI with 5 ng/mL BMP4 (R&D), 1 μM CHIR-99021, and 1x B-27 Supplement, minus insulin. On day 2 at 42 hours after induction, the media was changed to StemPro-34 SFM (Invitrogen) with 100 ng/mL VEGF (Peprotech), 5 ng/mL bFGF (Peprotech), 10 ng/mL BMP4, 50 μM Ascorbic Acid (Sigma), 2 mM L-Glutamine (Invitrogen), and 400 nM monothioglycerol (Sigma). The media was unchanged for 72 hours. At day 5, the media was changed to StemPro with 10 μM Rock inhibitor and 2 mM L-Glutamine. One hour after the media change, cells were harvested using versene (Thermo Fisher) with 0.25% trypsin (Thermo Fisher). Cells were replated into 0.2% gelatin coated 10 cm dishes at a density of approximately 10 K/cm^2 in EGM-2 with 20 ng/mL VEGF, 20 ng/mL bFGF and 1 μM CHIR-99021. Media was changed to EGM-2 with 20 ng/mL VEGF and 20 ng/mL bFGF at day 7 then changed every other day until the cells were harvested for use via trypsinization. hESC-ECs were used at day 10-12 for all experiments. To assess purity,

an aliquot of hESC-ECs was fixed in 4% PF then stained with 1:5 mouse anti-human CD31 FITC (BD Biosciences, 560984) in PBS for 45 minutes. Cells were assessed by flow cytometry on a Canto II system and FlowJo Software.

5.3.2 *Fabrication and culture of perfusable multilayer microvessels*

Multilayer microvessels were fabricated via soft lithography of collagen by adapting a previously published protocol for fabrication of single layer microvessels[124]. First, custom made acrylic housing devices that contained holes for inlets and collagen injection were milled and fabricated. The top housing devices were constructed to have removable portions to allow for additional media access upon submersion. Plastic shims (AccuTrex) of thickness 0.0075 inches were cut into 50 x 50 mm squares. Holes were cut in the center (~25 mm in diameter) and four corners. Flat and patterned PDMS pieces were prepared, with patterned pieces having a 13 x 13 grid network that protruded 110 μm. Inner surfaces of plastic shims and housing devices (excluding the removable pieces of the top housing device) were coated with 1% polyethylinime (Sigma) and 0.1% glutaraldehyde (Sigma) to provide a surface for collagen bonding. Once all the components were prepared, 6 mg/mL collagen was prepared by mixing 15 mg/mL type I collagen (extracted from rat tails) diluted in 0.1% acetic acid, 1 M NaOH (20 mM final concentration), 10x Medium 199 (ThermoFisher), Matrigel (1:60 dilution), and EGM-2. Either 3 million/mL HUVECs or 2.5 million/mL hPSC-ECs were added to the liquid collagen and the collagen was maintained on ice. Top and bottom collagen pieces were fabricated as previously described in Zheng et al[124]. Collagen membranes with one sided patterned were fabricated by gelling collagen within the large circular cutout of the plastic shims in between one flat piece and

one patterned piece of PDMS. A 2-mm biopsy punch was used to cut holes in the membranes for the inlet and outlet. For multilayer microvessels with 4 layers, 3 collagen membranes were sandwiched between the top and bottom housing devices, resulting in a collagen construct with height of approximately 1.5 mm. For 8-layer microvessels, 7 collagen membranes were added. This results in a stacked 3D geometry of open lumens that is completely perfusable through the same inlet and outlet. HUVECs or hPSC-ECs were seeded into the lumen as previously described then the removable pieces were removed. Single layer microvessels were similarly constructed without collagen membranes. For RNAseq and *in vivo* experiments, self-assembled constructs were created by gelling collagen in 12 mm x 1.5 mm PDMS wells. All microvessels were placed into deep 10 cm dishes that snugly fit the housing device. EGM-2 was added to submerge the microvessel to approximately half the height of the housing device. Microvessels were then cultured without motion overnight to allow for cell attachment. After 24 hours, microvessels were moved to a custom-made plate rocking system that tipped the culture dishes 15° every 3 hours. The dishes were aligned such that the inlets and outlets were perpendicular to the axis of rotation, causing media to accumulate in the lower inlet/outlet then perfuse through the microvessel to the other inlet/outlet after tipping. The media was removed from the inlets and outlets and replaced every 24 hours. For hPSC-EC microvessels and self-assembled constructs, 20 ng/mL VEGF and 20 ng/mL bFGF were added directly after fabrication. HUVEC microvessels were either cultured without additional supplementation or with 50 ng/mL VEGF, 50 ng/mL bFGF, 50 ng/mL phorbol 12-myristate 13 acetate (PMA) (Sigma), and 300 nM sphingospine-1-phosphate (Tocris) which was added to the media 24 hours after fabrication.

5.3.3 Immunofluorescent and histological staining, imaging, and analysis

All immunofluorescent and histological analysis was performed on multilayer and single layer microvessels that were cultured for 7 days. At the endpoint, 4% PF was perfused through the inlet and added onto the exposed collagen surface and left to fix for 30 minutes. Microvessels were then washed with PBS three times in the same manner. For 3D immunofluorescent imaging and analysis, microvessels were stained for VE-cadherin and F-actin. Briefly, microvessels were permeabilized and block with 0.5% Triton X-100 (Sigma) and 2% BSA (Sigma) in PBS for 1 hour. Microvessels were then stained with 1:100 Alexa Fluor 647 Phalloidin (Thermo Fisher, A22287), 1:50 mouse anti-human CD144 PE (Thermo Fisher, 12-1449-82), and 1:250 Hoechst for HUVEC microvessels or 1:100 Alex Fluor 488 Phalloidin (Thermo Fisher, A12379), 1:50 mouse anti-human CD144 APC (Thermo Fisher, 17-1449-42), and 1:250 Hoechst for mT-hESC-EC microvessels. For 8-layer tissues, RapiClear (SunJin Lab, RC149001) was added to the inlet and to the surface of the exposed collagen at least 1 hour prior to imaging to allow for increased visualization through collagen at greater depths. Large images containing the whole grid were taken on a Nikon Eclipse Ti2 widefield microscope. Smaller view 10x 3D confocal z-stacks were taken on a Nikon A1R confocal microscope at random locations within the grid pattern. FIJI was used to create maximum intensity projection images and for quantification of luminal volume and cross-sectional measures from the 10x confocal z-stacks. For luminal volume analysis, the open luminal area was quantified within each z-plane then multiplied by the thickness between individual slices. The luminal volume represents the luminal volume within one 10x z-stack field of view, not the total construct. For cross sectional analysis, orthogonal views of z-stacks were used to measure height,

width, and area of individual lumens. IMARIS Viewer was used to create orthogonal images of 8-layer microvessels. For histological assessment, microvessels were embedding in OCT compound (Fisher Scientific) then sectioned into 10 μm slices using a CryoStat. Sections were stained for either *Ulex Europaeus* Agglutinin I (UEA) or Col IV and VE-cadherin. For UEA staining, slides were blocked with 5% Normal Goat Serum (Jackson ImmunoResearch) for 1 hour, stained with 1:100 biotinylated UEA (Vector Laboratories, B-1065-2) overnight, stained using a VectaStain Elite ABC-HRP kit (Vector Laboratories, PK-6100) and SIGMAFAST DAB tablets (Sigma, D4293). For Col IV and VE-cadherin staining, slides were permeabilized and blocked with 0.5% Triton X-100 and 2% BSA for 1 hour, stained with 1:100 rabbit anti-collagen IV (Abcam, ab6586) overnight, then 1:100 mouse anti-human CD144 APC (Thermo Fisher, 17-1449-42), 1:100 Alexa Fluor 488 goat anti-rabbit, and 1:250 Hoechst for 1 hour then imaged on a Nikon TiE Inverted Widefield Fluorescence Microscope with Yokogawa W1 spinning disk head.

5.3.4 *Scanning electron microscopy preparation and imaging*

Scanning electron microscopy (SEM) was performed on 8-layer microvessels that were fixed on day 7 as described above. Following 4% PF fixation, the entire collagen construct containing the microvessels was removed from the housing device and plastic shims. The portion of the construct that contained the grid pattern was cut out using a razor blade, then cut in half for a cross-sectional slice through the lumens. Next, constructs were fixed in ½ strength Karnovsky's fixative (2.5% glutaraldehyde, 2% PF in 0.1M sodium cacodylate buffer, pH 7.3) overnight at 4°C. Constructs were then rinsed with 0.1M cacodylate buffer and dehydrated through a graded series of alcohols and

critical point dried using a Autosamdri-815 (Tousimis Corp). Then, constructs were mounted on stubs and sputter coated with gold/palladium using a Denton Desk IV (Denton Vacuum). Samples were imaged on a JSM 6610 LV scanning electron microscope at 5kV (JEOL). FIJI waw used to determine density of lumens and distance between lumens.

5.3.5 *Optical microangiography assessment of perfusable multilayer microvessels*

To visualize the 3D perfusable volume within the multilayer microvessels, optical microangiography (OMAG) imaging was used. During imaging, microvessels fixed with 4% PF at day 7 were attached to a syringe pump and perfused with 1% Intralipid (Sigma) in PBS at 10 µL/min. A handheld probe-based swept-source OCT (SSOCT) imaging system was used to collect the data. The probe was fixed on a custom built stand during imaging. The system implemented a vertical-cavity surface-emitting (VCSEL) swept laser source with a central wavelength of 1060 nm and 100 nm spectral bandwidth, giving a ~10 um axial resolution. The imaging probe was installed with a 5x objective lens with a ~20 um lateral resolution. Two separate scanning protocols were used to collect structural data for OMAG and to collect velocity data for optical microangiography-based velocimetry (OMAG-V).

In the first protocol for collecting OMAG data, an 9 mm x 9 mm field of view was imaged. A B-M mode scanning protocol was performed where 800 A-scans were acquired along the X-direction to compose a single B-scan (cross section) and 800 B-scans were taken along the Y-direction to generate a 3D volume. Each B-scan was repeated eight times then averaged and log-compressed to reconstruct tissue structure along the Z-

direction. In the second protocol for OMAG-V data, the data were collected by repeating each B-scan for ten times before switching to the following B-scan location until the whole volume was collected. In the fast axis, each B-scan is composed of 150 A-scans and 150 B-scans. A total of 1.6 mm x 1.6 mm will be covered with this scanning protocol. Temporal changes across the repeated B-scans were used to reconstruct vascular structures and produce velocity data using ED-based OMAG as previously described[145,146].

5.3.6 *Bead perfusion analysis*

After fixation at day 7 as described above, multilayer and single layer microvessels were attached to a syringe pump and perfused with 1:1000 FluoSpheres Carboxylated-Modified Microspheres beads, 2.0 μm diameter (Thermo Fisher, F8826) diluted in PBS at 10 μL/min. During the perfusion, fluorescent videos were acquired on a Nikon TiE Inverted Widefield Fluorescence Microscope with Yokogawa W1 spinning disk head with no delay. Four videos were acquired for each microvessel, with one video for each vessel layer at the center of the focal plane. The field of view for the videos included the 2 x 2 square section of the grid closest to the inlet, containing the first bifurcation. Bead velocity was quantified in the two straight portions of the pattern closest to the diagonal between the 4^{th} and 5^{th} bifurcations by manual particle tracking on FIJI.

5.3.7 *RNA isolation and RNA-seq data analysis*

RNA from hESC-EC multilayer microvessels, hESC-EC single layer microvessels, and hESC-EC self-assembled constructs at day 4 was collected and processed using an RNAeasy Micro Kit (Qiagen). RNA quality was assessed with an Aligent High Sensitivity

RNA ScreenTape System. All samples had RNA integrity number greater than 9. RNA samples were prepared using an XT DNA Library Prep Kit (Nextera XT) and a SMART-Seq v4 Ultra Low Input RNA Kit (SMARTv4), a poly-A selection kit using an oligo dT primer. RNA sequencing was performed on an Illumina NovaSeq 6000 SP with paired-end reads. RNAseq data was analyzed using iDEP.95 (integrated, Differential Expression and Pathway analysis, Bioinformatics Research Group, South Dakota State University). Samples were aligned to the hg38 and genes with >1 reads per million in at least a sample were kept for further analysis. edgeR was used for differential expression analysis with genes having fold change > 1.5 and FDR < 0.05 considered differentially expressed. ShinyGO v0.75 (Gene Ontology Enrichment Analysis, Bioinformatics Research Group, South Dakota State University) was used for GO term analysis and the top 12 relevant terms were displayed.

5.3.8 *Rat surgeries for ischemia/reperfusion and patch implantation*

All animal procedures were approved by the University of Washington Institutional Animal Care and Use Committee (IACUC, protocol #2225-04) and performed in accordance with US NIH Policy on Humane Care and Use of Laboratory Animals, including close monitoring following surgeries. In this study, 8-week-old, approximately 250-300g male athymic nude Sprague-Dawley rats were used. All rats had two thoracotomy surgeries that were 4 days apart. For the first surgery, rats underwent an ischemia/reperfusion surgery in which the left descending coronary artery was reversibly ligated for 60 minutes. Prior to the surgery, rats were given an intraperitoneal injection of 68.2 mg/kg ketamine and 4.4 mg/kg xylazine for anesthesia. Rats were also given a

second injection of ketamine and xylazine after the ligation began and a subcutaneous injection of sustained release buprenorphine (1 mg/kg) after surgery for analgesia. For the second surgery, collagen patches containing hESC-ECs were implanted onto the surface of the heart over the infarct and attached using two or three 8-0 sutures. The collagen patches were 4-layer microvessel or self-assembled constructs that contained hESC-ECs. They were constructed as described above and cultured for 4 days before being removed from the housing device and plastic shims and cut into a disk (8 mm in diameter x 1.5 mm thick) using a biopsy punch. Rats were anesthetized before and during the patch implantation surgery using isofluorane. Again, rats were given sustained release buprenorphine after surgery for analgesia. Additionally, rats received cyclosporine A (5 mg/kg) to prevent cell death by closing the mitochondrial permeability transition pore.

5.3.9 *Tissue harvest and retrograde perfusion fixation*

At 5 days after the ischemia/reperfusion surgery, rats were anesthetized with isofluorane then given 1.5 mL pentobarbital/phenytoin solution (Euthansol) for euthanasia. After breathing ceased, the chest was opened while the heart was still beating. 50 U Heparin then 3 mL of supersaturated KCl were injected into the inferior vena cava and allowed to circulate. Hearts were then excised, cannulated via the aorta, and attached to a custom-made perfusion system for retrograde perfusion. Vasodilation buffer (PBS with 4 mg/L Papaverin and 1 g/L adenosine) was first perfused through the heart to flush out the blood. Then 4% PF was perfused for 10 minutes at a stable pressure

of 100 mmHg to preserve the vasculature. Hearts were additionally fixed in 4% PF overnight before being rinsed with PBS the following day.

5.3.10 *Optical microangiography assessment of infarcted hearts with microvessel grafts*

Three hearts were randomly selected from each group for OMAG and OMAG-V imaging prior to histological analysis. Hearts were imaged using OMAG and OMAG-V protocols described above for multilayer microvessels, however, the field of view was only 4 mm x 4 mm for OMAG. During imaging, each sample was fixed in the center of a Petri dish using a 3D printed mount to prevent sample motion and perfused with 10% Intralipid through the cannulated aorta at a pressure of 100 mmHg. For quantification and visualization, the 3D vascular images were compressed to en-face images using maximum-intensity projection of vessels. Vessel area density was calculated as a percentage of pixels with perfusion signal over the whole imaging field. Relative perfusion was calculated by summing velocity of every pixel in the image and dividing by the average velocity sum for healthy regions.

5.3.11 *Lectin perfusion to label perfusable vasculature*

Prior to sectioning or tissue clearing, cannulated whole hearts were perfused with lectins to label perfusable vasculature. Briefly, hearts were attached to the custom-made perfusion system used during perfusion fixation and OMAG imaging. They were then perfused with PBS containing 8 μg/mL fluorescein-labeled *Griffonia simplicifolia* Lectin (GSL) (Vector Laboratories, FL-1101) and 8 μg/mL rhodamine-labeled *Ulex Europaeus* Agglutinin (UEA) (Vector Laboratories, RL-1062-2).

5.3.12 *Histological assessment of implanted tissues*

After lectin perfusion, hearts were cut into five 2 mm thick sections from the apex. Heart sections were then embedding in paraffin and sliced into 5 μm thick sections and put on slides for histological analysis. Slides were stained for picrosirius red/fast green or hemotoxylin and eosin to assess infarct size and gross morphology. Additional slides were stained for immunofluorescent analysis to assess vascularization within the grafts. Briefly, deparaffinized slides were subjected to antigen retrieval by a 25-minute incubation in 10 mM Tris/HCl with 15 μg/mL Proteinase K (Roche) at 37°C then blocking and permeabilization with 5% NDS and 0.1% Triton-X at room temperature for 1 hour. Next, slides were stained with 1:150 rabbit anti-DsRed (Conetech, 632496), 1:200 goat anti-GSL (Vector, AS-2104), and 1:150 mouse anti-Rhodamine (abcam, ab9093) in 5% NDS overnight, followed by staining with corresponding donkey secondaries. GSL stains both rat and human endothelium while UEA is specific to human endothelium. Because the lectins were perfused through the intact vasculature prior to heart sectioning, GSL stains all perfusable lumens and UEA stains perfusable human lumens. 20x or larger views of the grafts were imaged on a Nikon TiE Inverted Widefield Fluorescence Microscope with Yokogawa W1 spinning disk head. The density and size of GSL+, Rhodamine+ (UEA+), DsRed+ (mTm hESC-ECs) lumens were quantified using a custom Matlab code and 20x images.

5.3.13 *Heart tissue clearing and 3D imaging*

Cardiac patches were cleared and immunostained using a protocol derived from the Ce3D clearing protocol[208]. Cardiac patch samples were first punched out using a six-

millimeter biopsy punch. Samples were washed in PBS for one hour before being blocked overnight in Ce3D alternative blocking buffer (1x PermWash + 0.3% TritonX-100 + 1% bovine serum albumin + 1% normal donkey serum in PBS) at 38°C with slow shaking. The samples were next incubated in a primary antibody solution with goat anti-PDGFRβ (R&D Systems, AF385) at a concentration of 1:100 in the Ce3D blocking buffer with the addition of 5% dimethyl sulfoxide for 24 hours at 38°C with shaking. Samples were then washed with Ce3D wash buffer (0.3% TritonX-100 + 0.5% 1-thioglycerol in PBS) for six hours at 38°C with shaking, with the wash buffer changed every two hours. After washing, samples were incubated in a secondary antibody solution. Secondary antibodies, donkey anti-goat 647 (Thermo Fisher, A21447) and Hoechst (Thermo Fisher, H1399), were added at a concentration of 1:400 in the Ce3D blocking buffer with the addition of 5% dimethyl sulfoxide and incubated at 38°C with shaking overnight. Wash steps using Ce3D wash buffer were then repeated as previously described. Samples were next incubated in Ce3D clearing solution (40% N-methyl acetamide + Histodenz + 0.1% TritonX-100 + 0.5% 1-thioglycerol), shaking at 38°C overnight and then moved to room temperature. After a minimum of 24 hours of clearing, z-stacks of the full sample were taken at 10x using a Leica SP8 confocal microscope.

5.3.14 *Statistical analysis*

For statistical analysis of two groups, two-tailed *t* tests assuming unequal variance were used. For analysis of three or more groups, one-way ANOVA was used to test for differences among the groups, followed by pairwise *t* tests with correction for multiple comparisons. All results are presented as mean ± standard error of mean. Each data

point represents an average for each microvessel or animal and sample numbers represent the number of microvessels or animals analyzed. Significance is represented as * for $p < 0.05$, ** for $p < 0.01$, *** for $p < 0.001$, and **** for $p < 0.0001$.

5.4 Results

5.4.1 *Stacked multilayer microvessels for robust generation of 3D perfusable vasculature*

Previously, we have achieved microvessel networks in planar structure at ~110 μm in diameter. To support generation of thick tissues, we developed a stacking method to fabricate multilayer microvessels with 3D perfusable vascular networks in a collagen matrix. The multilayer microvessels were generated through soft lithography of multiple collagen layers that were subsequently stacked together to form a large network of open lumens (**Figure 5.1A**). The middle layers are formed by patterned collagen membranes that were stacked between a flat bottom piece of collagen and a patterned top piece of collagen within a housing device. Each layer was patterned with a 13 x 13 grid with 110 μm features and all layers were connected at the inlet and outlet by biopsy punch holes. To supplement the vascular network, housing devices with removable pieces were used to allow for additional media access on the surface of the construct, as this would be beneficial in highly cellularized tissues. This fabrication method allows for flexible design in regard to thickness, distance between vessels, and network geometry because membrane number, thickness, and patterning can be easily modified.

Using this method, we first generated microvessels with 4 layers of perfusable lumens by using three 190 μm-thick patterned collagen membranes. Following fabrication, multilayer microvessels were seeded with HUVECs by perfusion through the inlet and cultured in media containing VEGF, bFGF, S1P, and PMA (VBSP) to promote vascular remodeling. Microvessels were also cultured on a custom-built plate rocker to

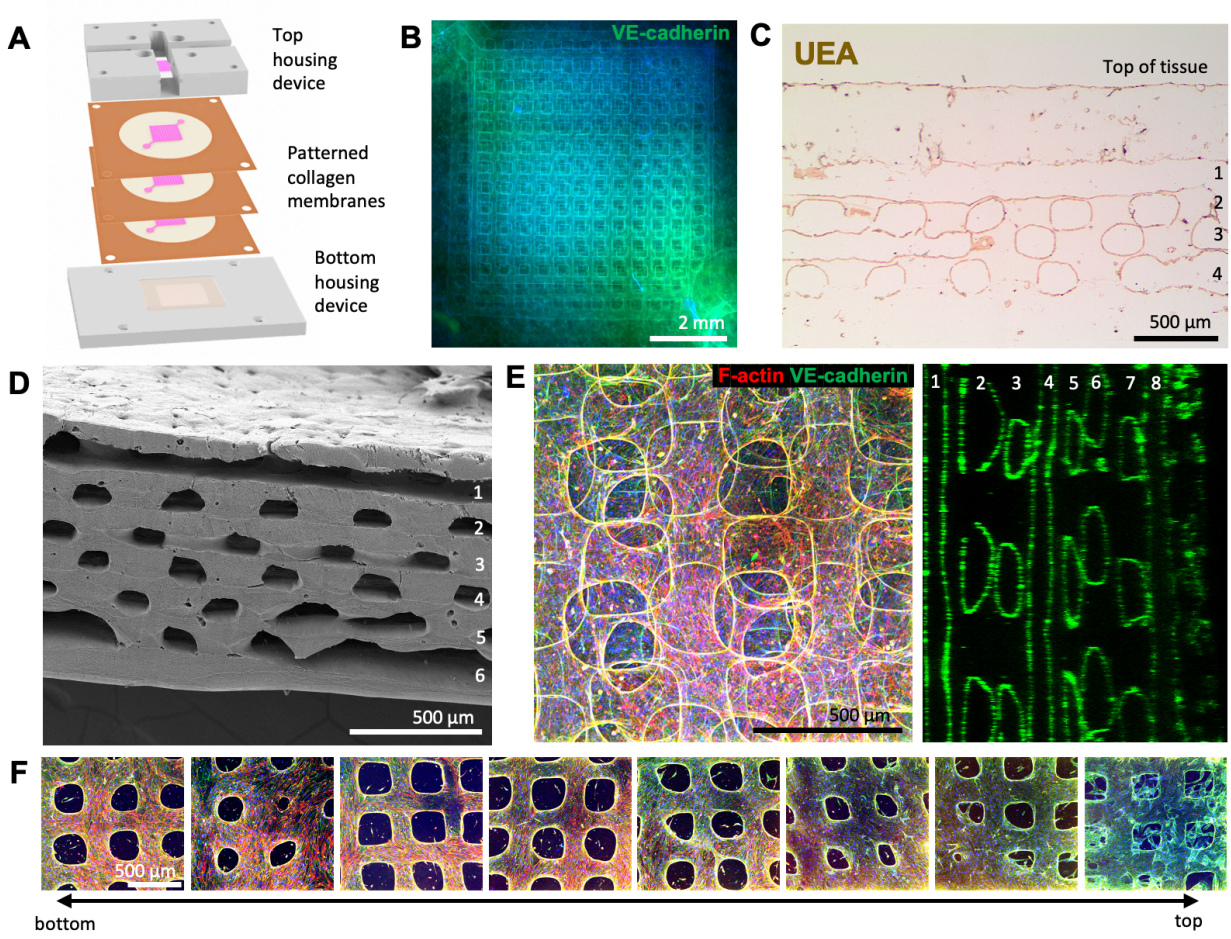

Figure 5.1 Multilayer microvessel fabrication and gross characterization. (A) Schematic of multilayer microvessel fabrication. (B) Stitched image of whole grid of 4-layer microvessels after 7 days of culture stained for VE-cadherin (green). Scale bar, 2 mm. (C) Histological section of 4-layer microvessel with immunohistochemical stain for *Ulex Europaeus* Agglutinin (UEA) to label human endothelium. (D) Scanning electron microscopy image of bottom 6 layers of 8-layer microvessel. Scale bar, 500 μm. (E) Confocal z-stack of 8-layer microvessel after 7 days of culture stained for VE-cadherin (green) and F-actin (red). Maximum intensity projection (MIP) of whole stack on left, orthogonal view on right. (F) MIP of individual layers from multilayer microvessel in (E). Scale bar, 500 μm.

initiate gravity driven perfusion through the vascular network once every 3 hours. At 7 days of culture, multilayer microvessels maintained their initial network geometry with patent endothelial-lined lumens in each of the 4 layers (**Figure 5.1B-C**). This indicates that multilayer vasculature can be successfully fabricated, endothelialized and cultured. To determine the robustness of our modular fabrication approach, we next generated 2 mm-thick constructs with 8 layers of perfusable vasculature (**Figure 5.1D-F**). The 8-layer microvessels were successfully seeded through the same inlet and outlet and maintained patent endothelial-lined lumens in all 8 layers (**Figure 5.1E-F**). Additionally, scanning electron microscopy (SEM) imaging revealed that 8-layer microvessels had a robust structural architecture of open lumens and high vascularity (**Figure 5.1D**). In the SEM images, we saw that the vascularized portion of the tissue had 20 patterned lumens per mm^2, covering over 25% of the cross-sectional area. There were less than 380 μm between any adjacent lumens in the xy-plane, which is mainly determined by the selected geometry of the patterned network. More importantly, adjacent lumens in the z-direction were separated by less than 120 μm, indicating the close proximity that can be achieved between stacked layers. Together, this demonstrates that stacking of patterned collagen to create multilayer microvessels is a robust technique for creating thick, highly vascularized tissues.

Next, we assessed the detailed structure of multilayer microvessels through histological analysis and SEM because the ability to remodel while maintaining structural integrity is critical for success of vascularized engineered tissues. We found that multilayer microvessels were capable of remodeling their surrounding collagen matrix to undergo angiogenesis while maintaining high fidelity after 1 week of culture, however, the

amount of vascular remodeling varied from region to region (**Figure 5.2A-B**). These variations could be due to the flow distribution differences in different regions in the square grid pattern we selected or additional exposure to proangiogenic factors at the surface of the tissue. In regions of both high and low vascular remodeling, the network maintained its initial pattern and the endothelium in the patterned lumens was smooth and well adhered to the collagen (**Figure 5.2A-B**). In regions of high vascular remodeling, sprouts with open lumens were seen branching off the patterned network and into the surrounding bulk collagen (**Figure 5.2B-D**). Occasionally, the vascular remodeling resulted in adjacent layers remodeling into one another, forming endothelial-lined pores connecting the two layers (**Figure 5.2D**). We next observed the interface between collagen layers because it could be an area of structural weakness due to our fabrication technique of stacking collagen layers after they were individually gelled. While we expected that we may see some gaps between the collagen layers, SEM imaging revealed that the collagen layers joined without gaps (**Figure 5.2E**). In fact, it appears as if the collagen matrix may be slightly compressed at the interface, indicating that the two layers are tightly joined. Additionally, we observed collagen IV on the endothelialized walls of both the patterned lumens and sprouts, indicating the presence of a basement membrane to adhere the endothelial cells to the surrounding matrix (**Figure 5.2F**). Taken together, these results indicate that a modular fabrication approach can be used to generate thick, highly vascularized tissues that simultaneously support cellular remodeling and structural integrity of the vasculature.

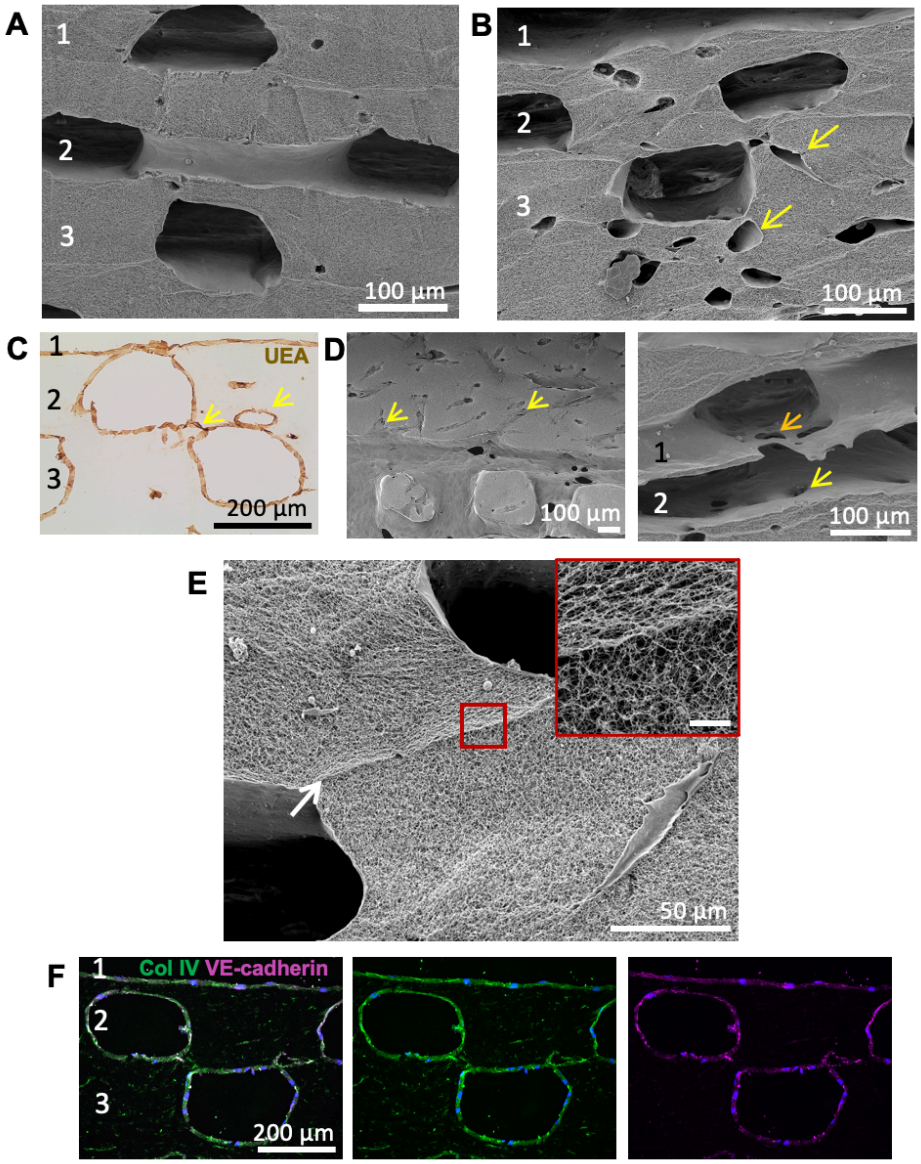

Figure 5.2 Assessment of multilayer microvessel fine structure and remodeling. (A,B) Scanning electron microscopy images of different regions of multilayer microvessel with angiogenic sprouts (yellow arrows). Scale bar, 100 µm. (C) Histological section of multilayer microvessel with immunohistochemical stain for *Ulex Europaeus* Agglutinin (UEA) to label human endothelium. Scale bar, 200 µm. (D) Scanning electron microscopy images of individual layer (left) with angiogenic sprouts (yellow arrows) and region with holes connecting layers (right) (orange arrows). Scale bar, 100 µm. (E) Scanning electron microscopy image of collagen interface (white arrow) between layers in multilayer microvessel. Inlayed image in red box. Scale bars, 50 µm and 10 µm. (F) Histological section of multilayer microvessel with florescent stain for collagen IV (green) and VE-cadherin (magenta). Scale bar, 200 µm.

5.4.2 *Perfusability of multilayer microvessels*

To assess the 3D luminal architecture and perfusability of our multilayer microvessels, we generated 4-layer microvessels that were cultured with or without additional proangiogenic factors, referred to as VBSP and EGM respectively, and 1-layer microvessels with similar conditions for comparison (**Figure 5.3A-D**). First, we analyzed cross-sectional and 3D views of the luminal architecture using confocal microscopy. Based on the geometry of our soft lithography patterning which had 110 μm x 110 μm channel features, we would expect to see lumens that were approximately the same size. All types of microvessels had lumens with widths that were greater than 110 μm (EGM 1-layer: 132.4 ± 0.8; VBSP 1-layer: 236.9 ± 15.3; EGM 4-layer: 110.8 ± 2.5; VBSP 4-layer: 197.4 ± 9.8 μm) but heights that were less than 110 μm (EGM 1-layer: 75.5 ± 5.45; VBSP 1-layer: 91.5 ± 1.6; EGM 4-layer: 64.1 ± 2.9; VBSP 4-layer: 76.7 ± 2.8 μm), indicating that vascular patterns were slightly compression during fabrication (**Figure 5.3E**). In both the 1-layer and 4-layer microvessels, the proangiogenic factors increased the width, height, and subsequently the cross-sectional area (EGM 1-layer: 8651.1 ± 536.6; VBSP 1-layer: 18500.5 ± 614.0; EGM 4-layer: 6108.4 ± 423.3; VBSP 4-layer: 12549.0 ± 388.3 μm^2) of each patterned lumen, suggesting vascular remodeling (**Figure 5.3E-F**). When comparing 1-layer and 4-layer microvessels, both the EGM and VBSP 4-layer microvessels (EGM 4-layer: 0.16 ± 0.01; VBSP 4-layer: 0.32 ± 0.01 μm^3) had slightly smaller cross-sectional areas than 1-layer microvessels of the same condition (EGM 1-layer: 0.06 ± 0.01; VBSP 1-layer: 0.11 ± 0.01 μm^3) (**Figure 5.3F**). Although the average cross-sectional areas were smaller for 4-layer microvessels, the total luminal volume per

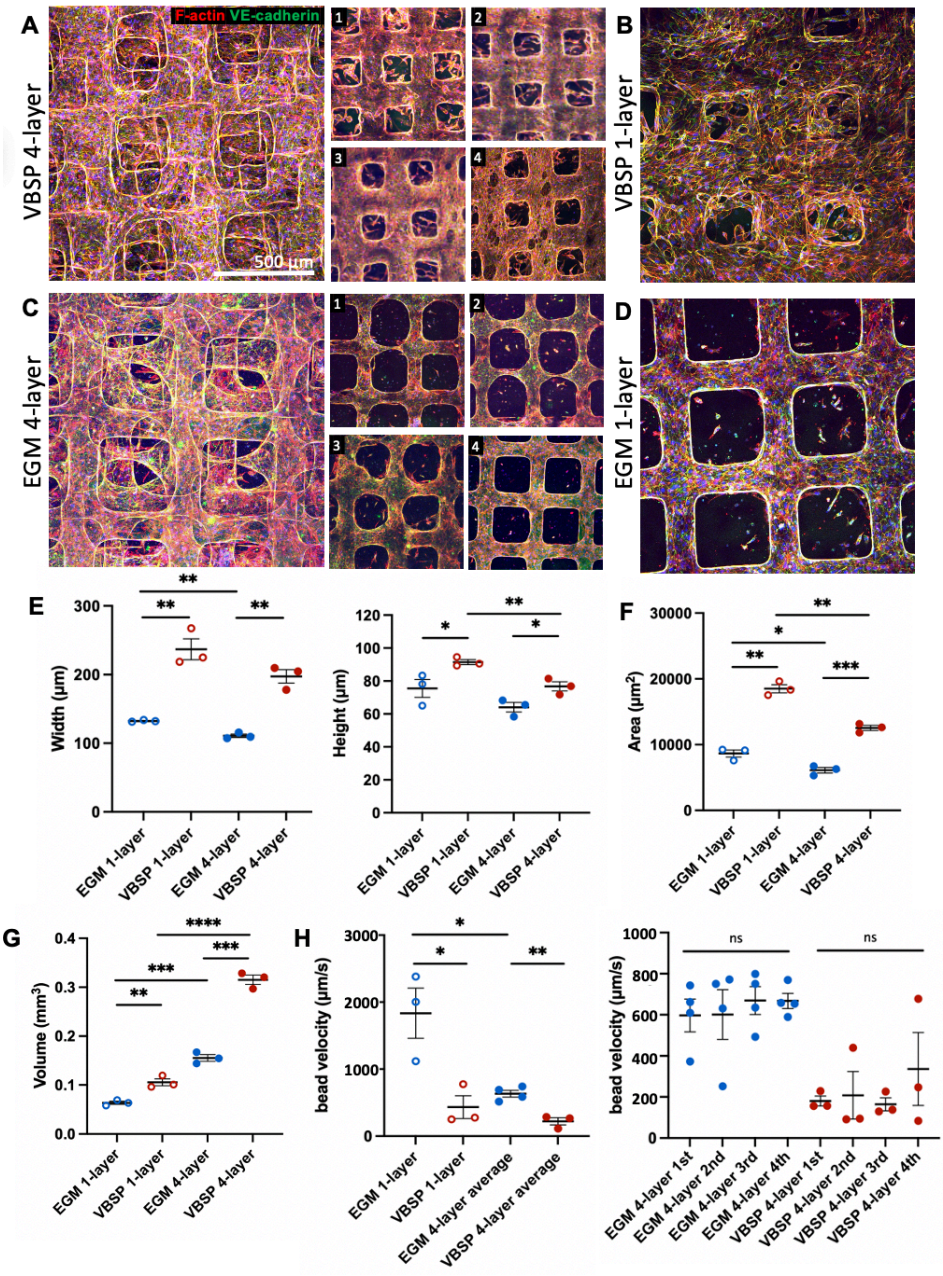

Figure 5.3 Luminal volume and perfusion of multilayer microvessels. (A-D) Confocal z-stacks of VBSP 4-layer (A), VBSP 1-layer (B), EGM 4-layer (C), and EGM 1-layer (D) after 7 days of culture stained for VE-cadherin (green) and F-actin (red). MIP of whole stack. MIP of individual layers on right for 4-layers. Scale bar, 500 μm. (E-G) Quantification of average lumen width (E), average lumen height (E), average cross-sectional area per lumen (F), and total luminal volume per field of view (G) for EGM 1-layer, VBSP 1-layer, EGM 4-layer, and VBSP 4-layer vessels. (H) Quantification of average bead velocity at the center of the channel between the fourth and fifth bifurcations for EGM 1-layer, VBSP 1-layer, EGM 4-layer, and VBSP 4-layer vessels. Error bars, mean ± SEM. *p < 0.05, **p < 0.01, ***p < 0.001, and ****p < 0.0001 determined using two-tailed t-test.

field of view was drastically higher in the 4-layer microvessels than the 1-layer microvessels for both the EGM and VBSP conditions (**Figure 5.3G**).

To assess the perfusability, we first perfused florescent beads through the inlets at a constant flow rate of 10 μL/min and quantified bead velocity in the center of the channel at the same point in every microvessel and each layer (**Figure 5.3H**). As expected, the trends where inversely related to those of the luminal volume, with trends towards decreased bead velocity in 4-layer microvessels when compared to 1-layer microvessels and in microvessels with VBSP when compared to microvessels with EGM only (EGM 1-layer: 1835.0 ± 375.3; VBSP 1-layer: 434.2 ± 170.7; EGM 4-layer: 633.8 ± 50.7; VBSP 4-layer: 222.3 ± 54.0 mm/s). As maximum velocity is proportional to resistance when flow rate is held constant, this indicates that the multilayer architecture reduces the overall resistance within the construct. To determine whether perfusion through the multilayer microvessels was uniformly distributed between layers or whether our fabrication technique biased the perfusion towards specific layers, we also compared the bead velocity within individual layers of multilayer microvessels (**Figure 5.3H**). We found no statistically significance difference between individual layers for both microvessels with EGM and microvessels with VBSP, suggesting uniform distribution.

To visualize the perfusion through the multilayer microvessels, we utilized optical microangiography (OMAG) to obtain 3D images of Intralipid perfusing through the vasculature (**Figure 5.4A-C**). We saw that the initial patterned geometry was entirely perfusable after 7 days of culture. We additionally utilized OMAG-based velocimetry (OMAG-V) to visualize the flow dynamics near the inlet of multilayer microvessels (**Figure 5.4D**). Consistent with the results of the bead perfusion analysis, we saw similar perfusion

profiles throughout each layer, suggesting evenly distributed perfusion. Overall, these results demonstrate that our method can be used to robustly create highly perfusable tissues with well-distributed flow.

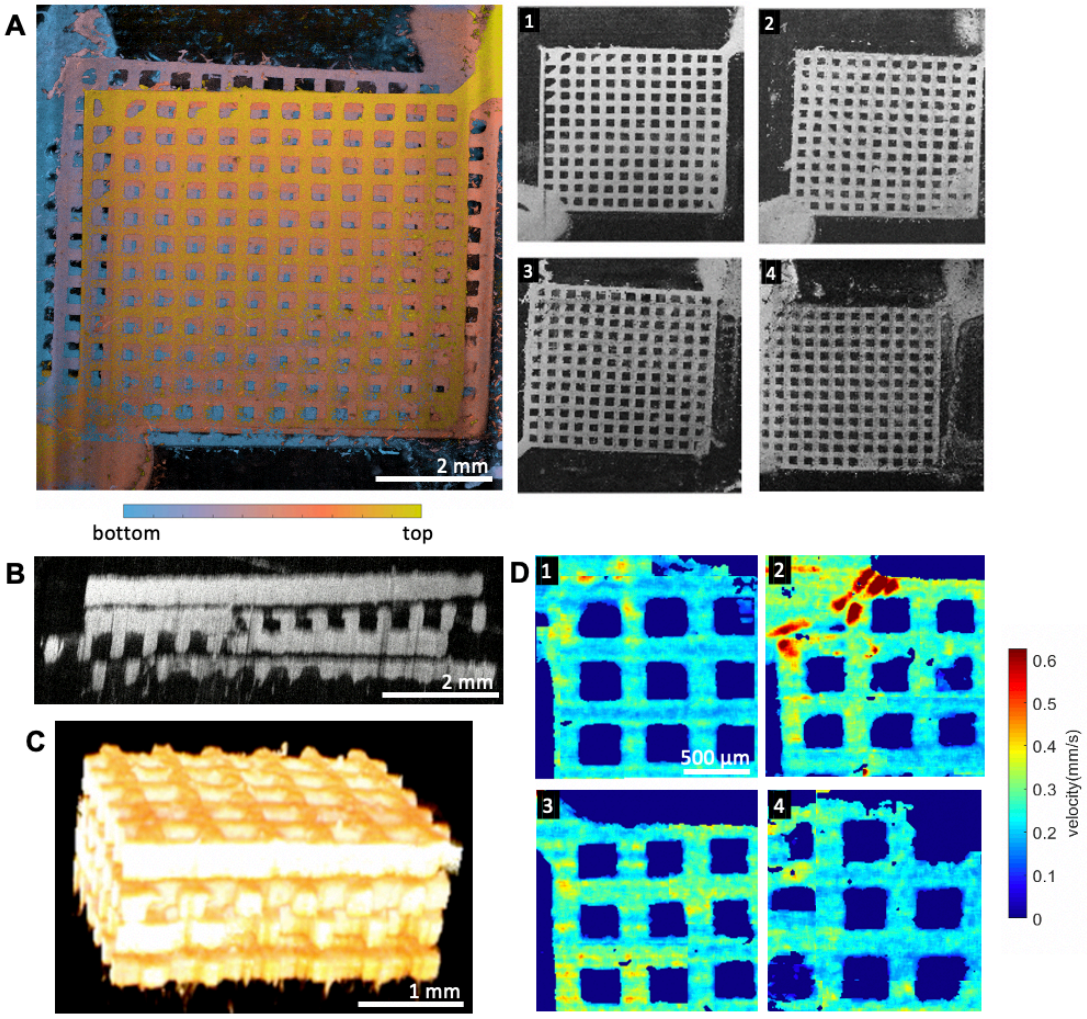

Figure 5.4 OMAG imaging of perfusion through multilayer microvessels. (A-C) Optical microangiography (OMAG) images showing perfusable area of multilayer microvessel with 4 layers. (A) Projection image with color coded depth on left, individual layers on right. Scale bar, 2 mm. (B) Cross-sectional view. Scale bar, 2 mm. (C) 3D view. Scale bar, 1 mm. (D) OMAG-based velocimetry (OMAG-V) of multilayer microvessels with 4 layers showing velocity of each layer near the inlet. Scale bar, 500 µm.

5.4.3 *Gene expression of hPSC-EC multilayer microvessels*

As human stem cell derived endothelial cells (hPSC-ECs) may be an ideal cell source for tissue engineering and regenerative medicine applications, we next generated 4-layer microvessels using hPSC-ECs. We utilized hPSC-ECs that were differentiated using a protocol to generate endocardial-like endothelial cells from RUES2 stem cells with >90% purity as indicated by CD31 expression[73,74] (**Figure 5.5A**). Similar to HUVEC multilayer microvessels, hPSC-EC multilayer microvessels could be successfully endothelialized with patent lumens in the patterned channels after multiple days of culture (**Figure 5.5B**). Addition of proangiogenic factors (VBSP) caused hPSC-EC multilayer microvessels to undergo vascular remodeling and sprout into the surrounding collagen matrix (**Figure 5.5C**).

To investigate the effect of multilayer stacking on gene expression, we performed RNAseq analysis comparing multilayer microvessels (4-layer μV), single layer microvessels (1-layer μV), and non-perfusable self-assembled constructs (SA) generated using hPSC-ECs and cultured for 4 days. We saw robust gene expression differences when comparing either multilayer microvessels or single layer microvessels to self-assembled constructs. There were 3192 significant differentially expressed genes (fold change >1.5 and FDR <0.05) between single layer microvessels and self-assembled constructs and 2797 differentially expressed genes between multilayer microvessels and self-assembled constructs (**Figure 5.6A-B**). As expected, we saw that gene expression was much more similar between multilayer and single layer microvessels with only 231 differentially expressed genes (**Figure 5.6A-B**). We next performed principal component analysis (PCA) which revealed clear separation of the self-assembled constructs from

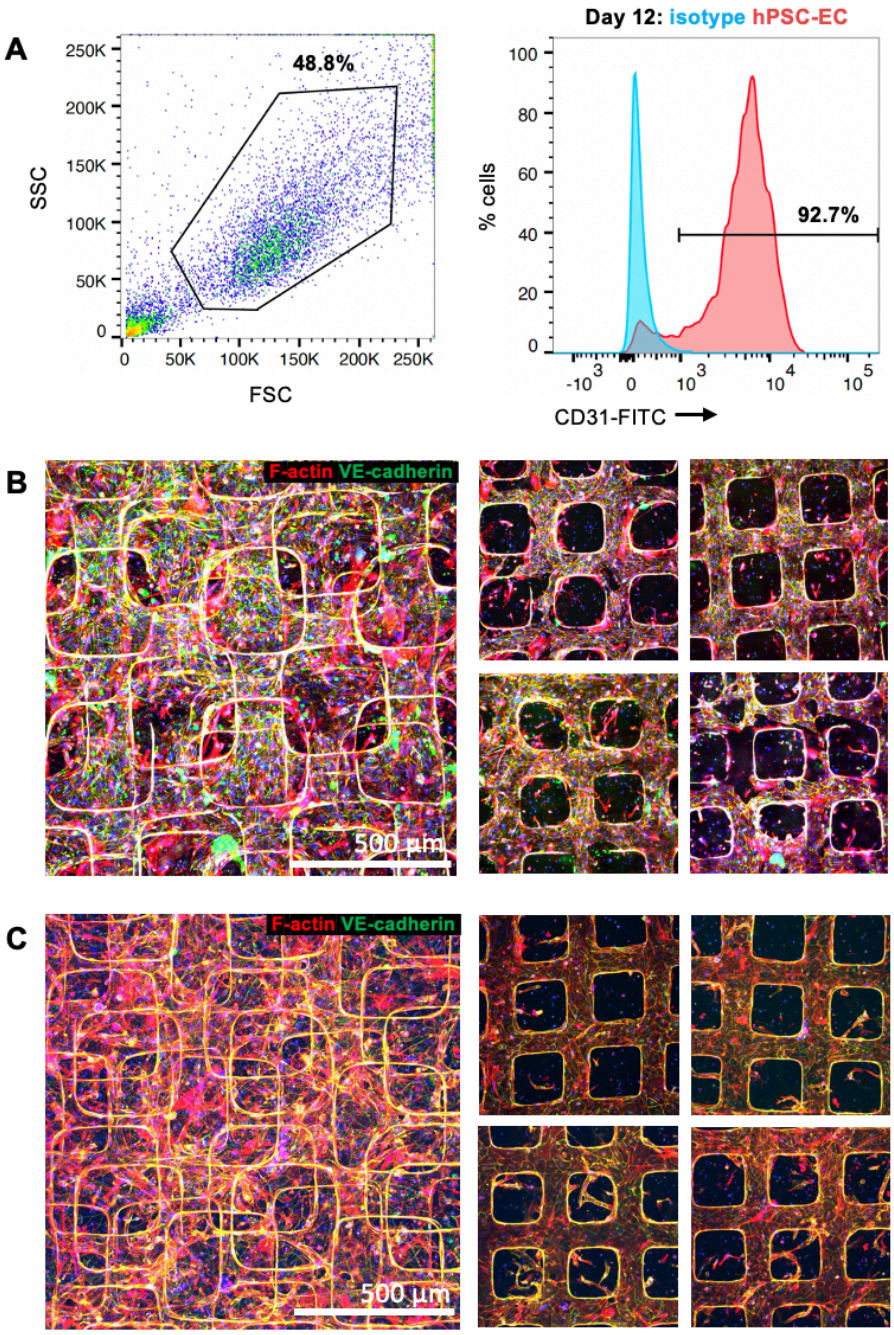

Figure 5.5 Multilayer microvessels with hPSC-ECs. (A) Flow cytometry assessment of hESC-ECs at day 12 of differentiation. Forward and side scatter used to gate main population on left, CD31 expression of hESC-ECs on right with overlay of isotype controls. (B-C) Confocal z-stacks of 4-layer hPSC-EC microvessels after 7 days of culture in hPSC-EC media (B) or VBSP media (C) stained for VE-cadherin (green) and F-actin (red). MIP of whole stack on left, MIP of individual layers on right. Scale bar, 500 µm.

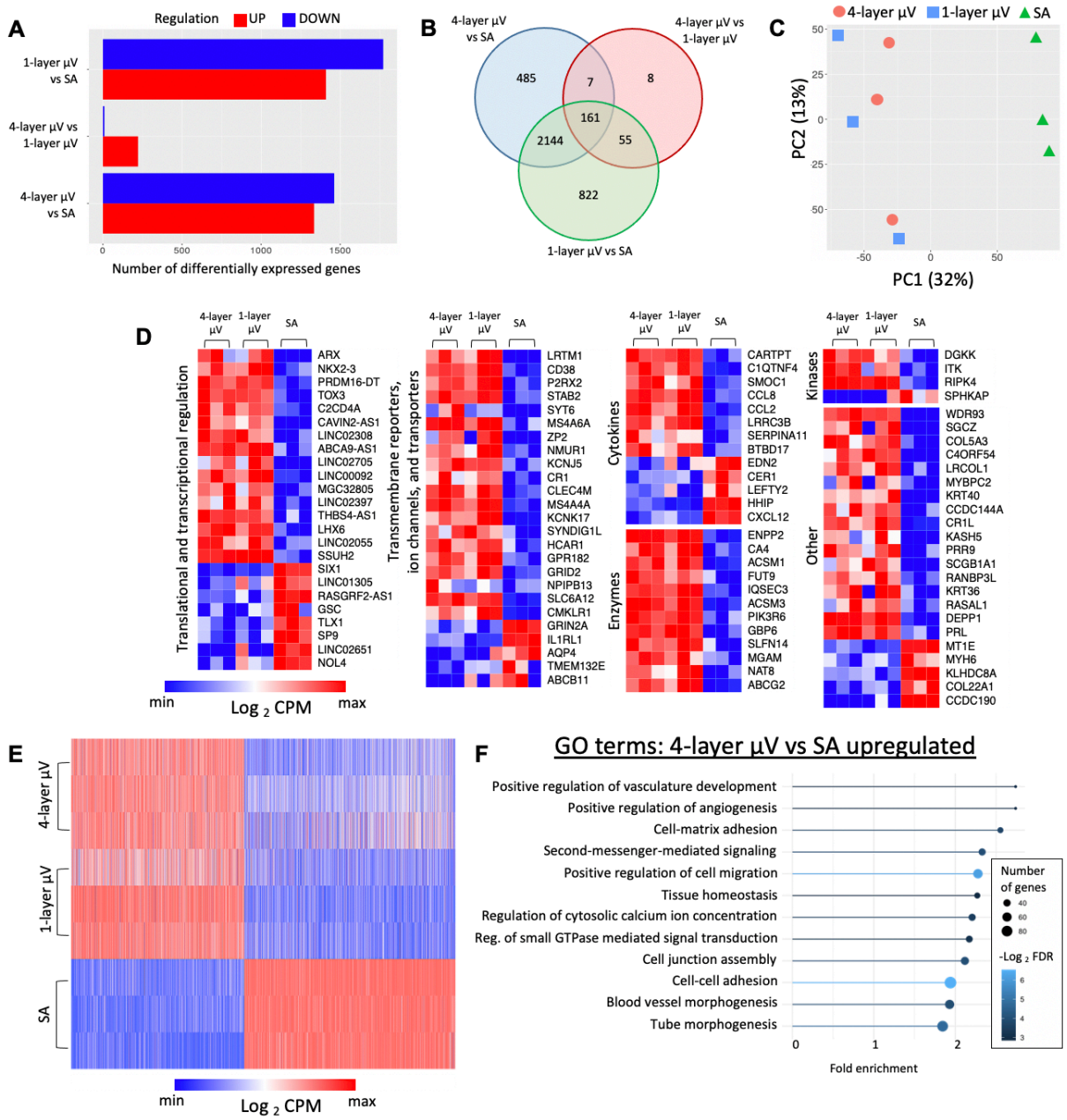

Figure 5.6 Gene expression of hPSC-EC multilayer microvessels, single layer microvessels, and self-assembled constructs. (A) Bar chart with the number of upregulated and downregulated differentially expressed genes for all pairwise comparisons from RNAseq analysis. (B) Venn-diagram with the number of differentially expressed genes. (C) Principal component analysis (PCA) plot. (D) Heat map of top 100 differentially expressed genes between multilayer microvessels and self-assembled constructs. Colormap normalized to minimum (blue) and maximum (red) expression of $\log_2$ CPM values. (E) Heat map of all genes that were differentially expressed between any two conditions. (F) Gene ontology analysis for terms upregulated in multilayer microvessels when compared to self-assembled constructs. 4-layer μV, multilayer microvessel. 1-layer μV, single layer microvessel. SA, self-assembled construct. CPM, counts per million.

both microvessel conditions, and no clear distinction between the multilayer and single layer microvessels (**Figure 5.6C**). The top differentially expressed genes between multilayer microvessels and self-assembled constructs include translational/transcriptional regulators such as *ARX* and *NKX2-3*, transmembrane proteins such as *LRTM1* and *CD38*, cytokines such as *CARTPT*, and enzymes such as *ENPP2* and *CA4* (**Figure 5.6D**). Again, we saw trends demonstrating similar expression profiles between single and multilayer microvessels for both the most differentially expressed genes and all genes that were differentially expressed between any two conditions (**Figure 5.6D-E**). Next, we performed Gene Ontology (GO) analysis and found that multilayer microvessels were upregulated for positive regulation of angiogenesis, positive regulation of vasculature development, cell-matrix adhesion, second-messenger-mediated signaling, positive regulation of cell migration and other terms related to vascular remodeling and stability (**Figure 5.6F**). When comparing multilayer and single layer microvessels, we found no significant GO terms. Taken together, these results suggest that multilayer and single layer microvessels have similar gene expression profiles and that multilayer microvessels have gene expression towards vascular development when compared to non-perfusable, self-assembled constructs.

5.4.4 *Vascular integration of multilayer microvessel grafts implanted onto infarcted rat hearts*

To determine whether multilayer microvessels would improve host vascular integration *in vivo*, we implanted 4-layer microvessel constructs and non-perfusable, self-assembled constructs onto infarcted rat hearts. Both types of constructs were

approximately 1.5 mm thick and were generated 4 days prior to implantation with mT-hPSC-ECs in the bulk collagen matrix (2.5 M/mL) and lining the lumens of the 4-layer microvessels. Constructs were sutured onto the epicardial surface of hearts in rats that had undergone temporary ligation of the left anterior descending artery to cause infarction 4 days earlier (**Figure 5.7A**). Hearts with vascular patches were harvested 5 days after implantation to detect differences in early vascular integration of the graft, as early vascularization will be critical for supporting engraftment of highly cellularized tissues (**Figure 5.7B**). Upon harvest, hearts were arrested in diastole and fixed via retrograde perfusion of fixative through the coronary vasculature to preserve the vasculature in its most open state. To evaluate the gross morphology of the heart and the graft, we performed histological analysis. Using picrosirius red and fast green, we were able to

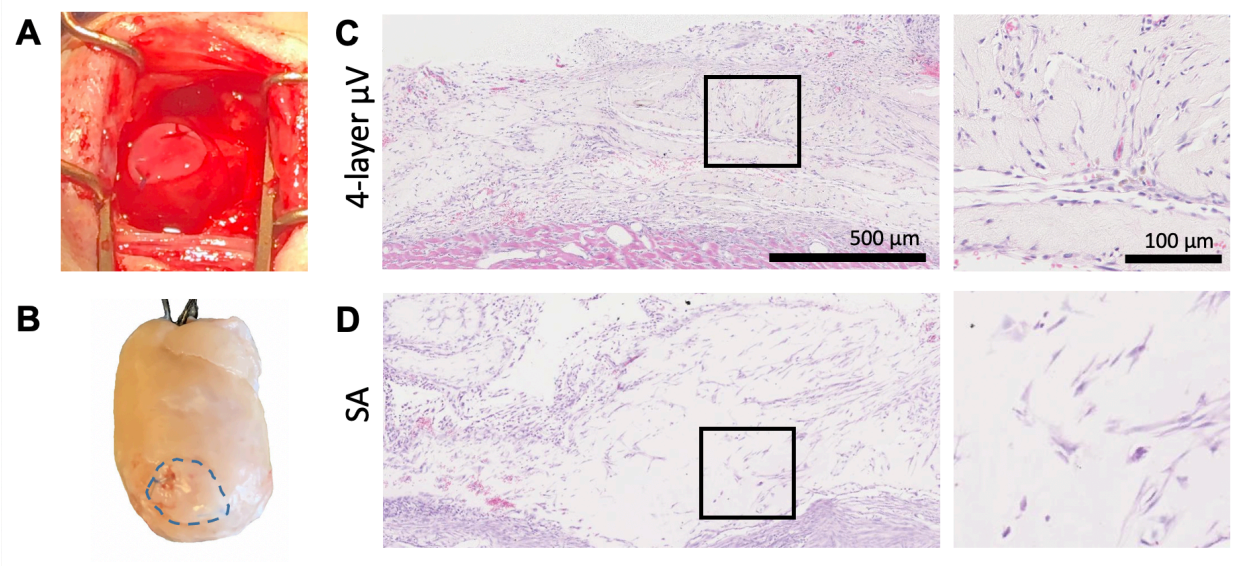

Figure 5.7 Implantation of multilayer microvessel grafts onto infarcted rat hearts. (A) Image of multilayer microvessel graft sutured onto the epicardial surface of a rat heart during implantation surgery. (B) Image of excised heart with graft outlined in blue. (C,D) Hemotoxylin and eosin histological staining of 4-layer µV (C) and SA (D) grafts. Zoomed in image of black box on right. Scale bars, 500 µm, 100 µm. 4-layer µV, multilayer microvessel. SA, self-assembled construct.

distinguish between collagenous regions including the graft and the infarct scar from the healthy myocardium and found similar infarct sizes between the 4-layer microvessel group and the self-assembled group (**Figure 5.8A-C**). Differences in the morphology of the two tissues was apparent with hemotoxylin and eosin staining. In multilayer microvessel grafts, many lines of high cellularity could be identified throughout the graft, although the 4-layer grid pattern was no longer identifiable, indicating tissue remodeling (**Figure 5.7C**). In comparison, the self-assembled tissues appeared to have more random cellular organization (**Figure 5.7D**).

To assess the vasculature within the grafts, we utilized a combination of lectin perfusion, tissue clearing, histological analysis, and optical microangiography. Prior to sectioning, we perfused lectins through the *ex vivo* whole hearts via the aorta to label perfusable vasculature that was anastomosed to the host and would have therefore been perfused with blood *in vivo*. We used fluorescein-labeled *Griffonia simplicifolia* Lectin

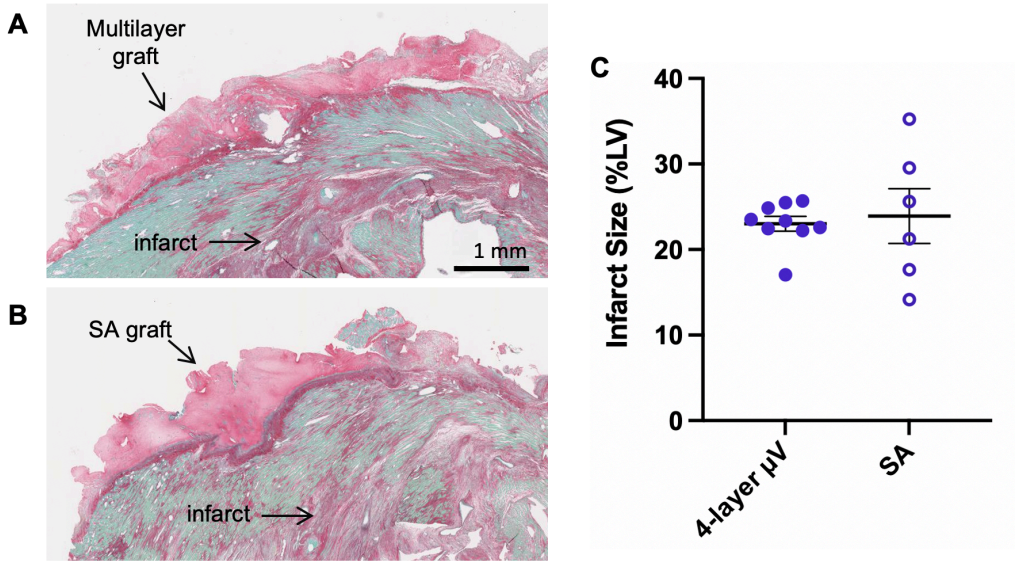

Figure 5.8 Infarct size analysis of hearts with implanted multilayer microvessel grafts. (A,B) Picrosirius red/fast green stain to 4-layer µV (A) and SA (B) grafts. Collagenous regions, such as the infarct and grafts, stain red/purple and healthy tissue regions stain green. Scale bar, 1 mm. (C) Quantification of infarct size as a percentage of left ventricle area. 4-layer µV, multilayer microvessel. SA, self-assembled construct.

(GSL) to label all perfusable vasculature from both human and rat origin and rhodamine-labeled *Ulex Europaeus* Agglutinin (UEA) to label human-specific perfusable vasculature. To visualize the three-dimensional vasculature within whole grafts, we punched out the regions of the hearts containing the grafts and optically cleared the tissues (**Figure 5.9A,B**). In both types of grafts, we found perfusable vasculature, with the multilayer microvessel grafts appearing to be more densely vascularized than the self-assembled grafts (**Figure 5.9C,D**). We noted that remodeling appeared more robust in some regions of the grafts than in others. In the multilayer microvessel grafts, we identifed some small regions that maintained the grid pattern from the initial fabrication, yet the pattern appeared to be remodeled or not perfusable throughout most of the graft (**Figure 5.9C**). Additionally, we saw that the multilayer microvessel grafts had regions with dense perfusable vasculature and other regions that were sparsely vascularized (**Figure 5.9C**).

To quantify the vascular density, we performed histological analysis with staining for GSL to identify all perfusable vasculature, UEA to identify human perfusable vasculature, and mTomato to identify human cells that survived implantation, whether perfusable or non-perfusable (**Figure 5.9E,F**). We found that multilayer microvessel grafts had significantly greater density of both GSL-positive and UEA-positive lumens (GSL+: 437.5 ± 29.2; UEA+: 170.2 ± 15.2 vessels/mm^2) when compared to self-assembled grafts (GSL+: 176.3 ± 19.6; UEA+: 64.9 ± 15.6 vessels/mm^2), indicating that multilayer microvessels resulted in higher vascular integration at early timepoints (**Figure 5.9G**). Interestingly, the density of GSL-positive lumens was significantly greater than the density of UEA-positive lumens in both types of grafts, suggesting that host vascular ingrowth significantly contributed to the vascularization of the grafts. GSL-positive lumens were

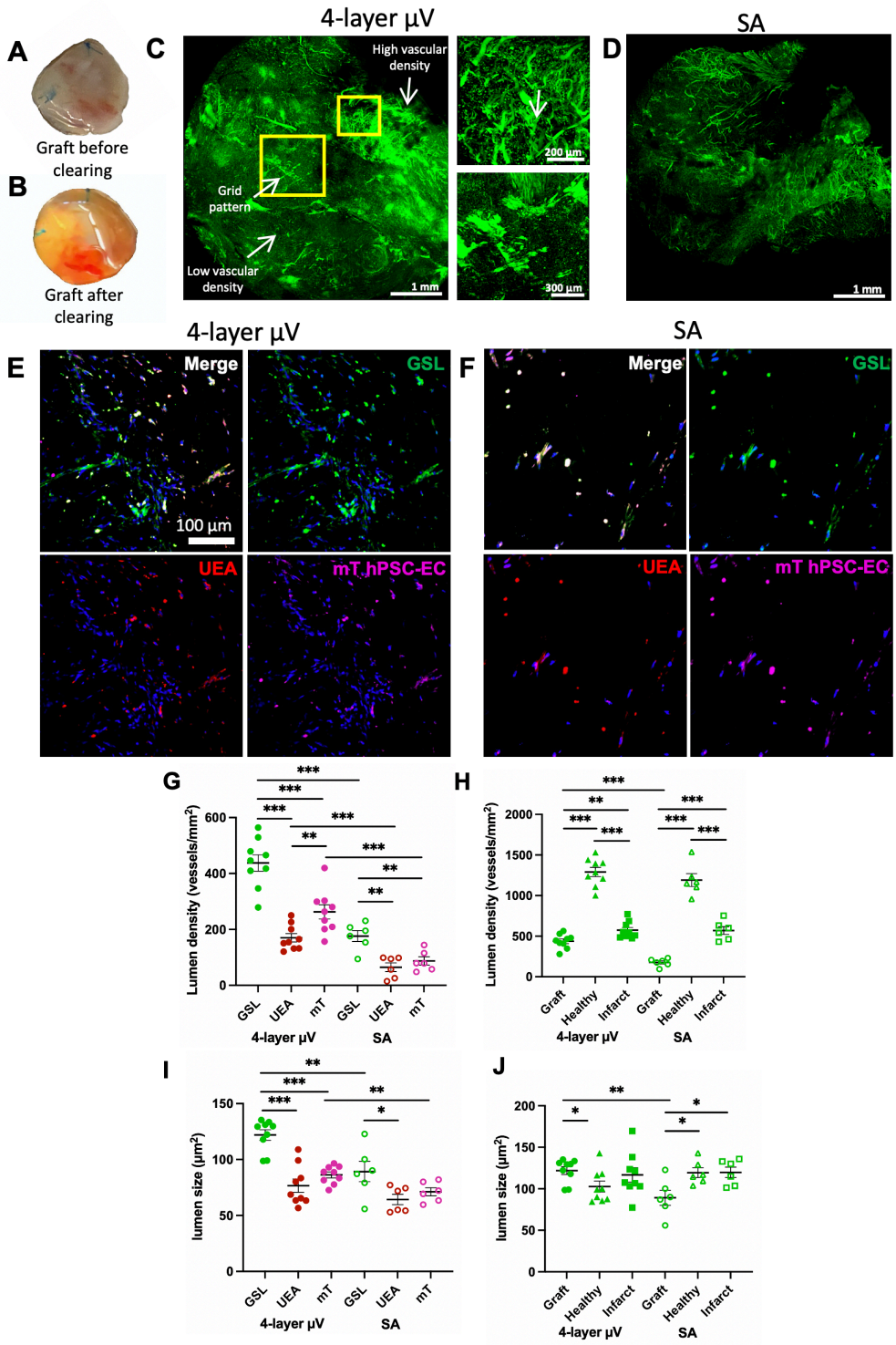

Figure 5.9 Assessment of perfusable vasculature of implanted multilayer microvessel grafts. (A,B) Excised graft before (A) and after (B) tissue clearing. (C,D) Maximal intensity projections (MIP) of cleared 4-layer µV graft (C) and SA graft (D) stained with fluorescein-labeled *Griffonia simplicifolia* Lectin (GSL). Whole patch on left. Zoomed in regions from yellow boxes showing region of highly vascularized region on top right and partial grid pattern on bottom right. Scale bars, 1 mm, 200 µm, 300 µm. (E,F) Histological analysis of 4-layer µV (E) and SA (F) grafts stained for GSL (green), UEA (red) and mTomato (magenta). Scale bar, 100 µm. (G-J) Quantification of GSL+, UEA+ and mT+ lumen density (G,H) and lumen size (I,J) in 4-layer µV and SA grafts (G,I) and in healthy and infarcted regions (H,J) based on histological analysis. Error bars, mean ± SEM. *$p < 0.05$, **$p < 0.01$, and ***$p < 0.001$ determined using two-tailed t-test.

larger on average than UEA-positive lumens in both graft types with multilayer microvessels grafts having larger GSL-positive lumens than self-assembled grafts (GSL+ 4-layer μV: 121.9 ± 4.7; GSL+ SA: 89.2 ± 9.1; UEA+ 4-layer μV: 76.6 ± 5.9; UEA+ SA: 64.3 ± 4.6 μm^2) (**Figure 5.9I**). We also found that multilayer microvessel grafts had greater density of mTomato-labeled lumens than self-assembled grafts (262.8 ± 25.5; 87.3 ± 14.8 vessels/mm^2, respectively), suggesting greater engraftment of implanted cells. We also assessed the perfusable vasculature within the infarcted and healthy myocardium of each heart. We found no differences between the vascular density or average lumen size between the hearts with multilayer microvessel or self-assembled grafts in either the infarcted or healthy tissue (healthy 4-layer μV: 1291.0 ± 56.5; healthy SA: 1191.2 ± 78.8; infarct 4-layer μV: 573.5 ± 34.3; infarct SA: 569.9 ± 48.2 vessels/mm^2) (**Figure 5.9H,J**). Additionally, the vascular density of the grafts did not reach that of the infarct for both graft types (**Figure 5.9J**).

To assess the perfusion dynamics within the hearts, we imaged the whole hearts using depth-resolved optical microangiography (OMAG) and OMAG-based velocimetry (OMAG-V) during retrograde perfusion of Intralipid at a constant pressure of 100 mmHg (**Figure 5.10A,B**). Aligning with the trends from the histological analysis, vascular area density was greater in multilayer microvessels grafts (28.1 ± 4.1 %) than in self assembled grafts (6.3 ± 2.4 %) and both types of grafts had lower vascular area density than healthy regions on the same hearts (4-layer μV: 81.6 ± 11.3; SA: 94.5 ± 3.4 %) (**Figure 5.10C**). Notably, the perfusable vasculature of the microvessel grafts appeared to span the depth of the graft, with no obvious layers as might be expected due to the initial pattern geometry (**Figure 5.10A**). In addition to vascular structure, we used OMAG-V to determine the

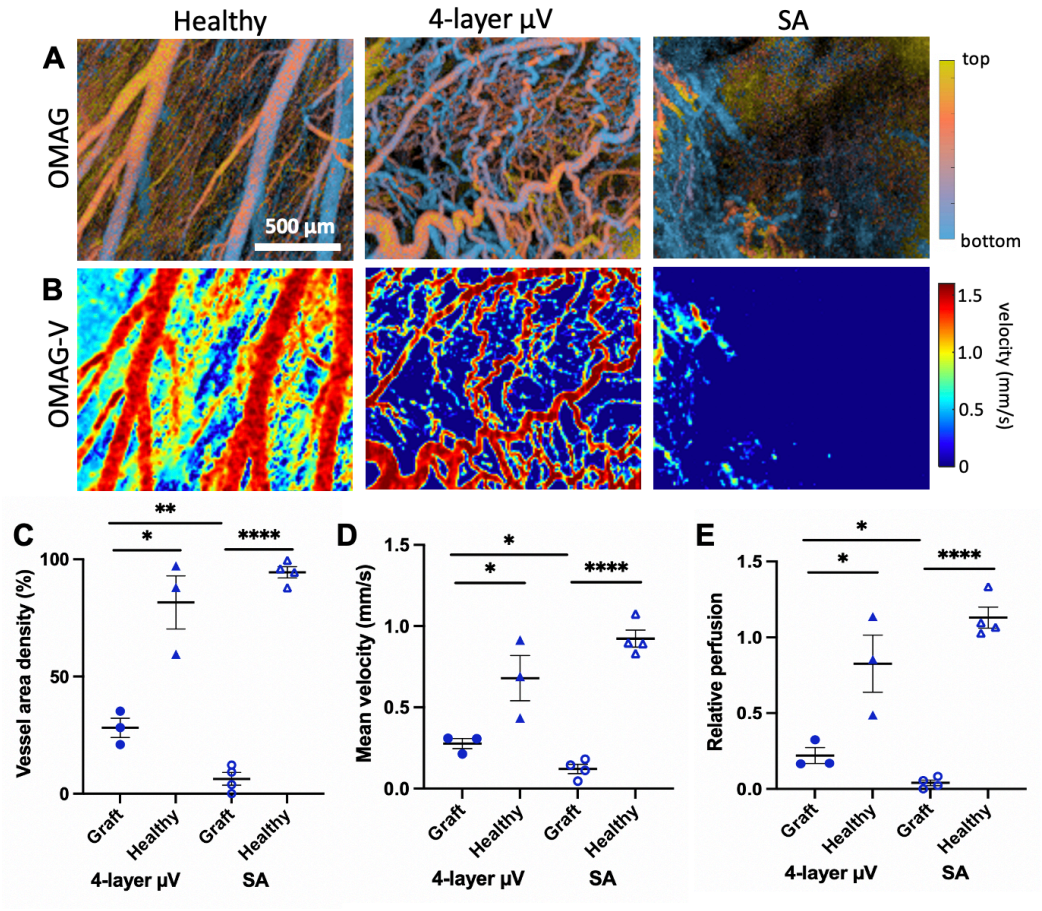

Figure 5.10 Optical microangiography of implanted multilayer microvessel grafts. (A,B) Projection images of optical microangiography (OMAG) (A) and OMAG-based velocimetry (OMAG-V) (B) of perfusable vasculature in healthy region (left), 4-layer μV graft (middle), and SA graft (right). OMAG projection image with color coded depth. OMAG-V projection image with color coded velocity. Scale bar, 500 μm. (C) Quantification of vessel area density as a percentage of the whole image area. (D) Quantification of mean velocity within the perfusable vasculature. (E) Quantification of perfusion relative to the average of the healthy regions. 4-layer μV, multilayer microvessel. SA, self-assembled construct. Error bars, mean ± SEM. *p < 0.05, **p < 0.01, and ****p < 0.0001 determined using two-tailed t-test.

velocity of the perfusate as it traveled through the vasculature. We found that multilayer microvessel grafts had greater average velocity throughout the vasculature than self-assembled grafts (0.28 ± 0.03; 0.12 ± 0.02 mm/s, respectively) (**Figure 5.10D**). However, neither graft type achieved the same average velocity as in the healthy region (4-layer μV: 0.68 ± 0.14; SA: 0.93 ± 0.07 mm/s) (Figure 4M). We additionally quantified tissue perfusion relative to the average for healthy regions and found perfusion to be greater in

the multilayer microvessel grafts (0.22 ± 0.05) than the self-assembled grafts (0.04 ± 0.02), again not reaching that of the healthy region for either condition (4-layer μV: 0.83 ± 0.19; SA: 1.13 ± 0.06) (**Figure 5.10E**). Taken together, these results indicate that incorporation of perfusable, multilayer microvessels into engineered tissue constructs can improve host vascular integration and graft perfusion at early timepoints after implantation with functional contribution from the grafted vasculature.

5.5 Discussion

Adequate vascularization and perfusion remain critical challenges in the generation of large-scale engineered tissues. While many methods for incorporating perfusable vasculature into engineered tissues have been developed, large tissues with high-density vasculature have not been achieved due to limitations of fabrication time, complexity constrains, and material selection. Here, we utilized soft lithography and multilayer stacking of collagen membranes to generate thick tissues with three-dimensional, perfusable vasculature having separation of less than 380 μm between any adjacent lumens. We demonstrated that tissues fabricated using this method can maintain structure after 1 week in culture while undergoing angiogenesis into the surrounding bulk matrix. More importantly, we showed that these tissues are highly perfusable, with consistent perfusion throughout the tissue.

In addition to achieving highly vascularized tissues *in vitro*, we implanted these tissues onto infarcted rat hearts, demonstrating the feasibility of using modularly assembled tissues for *in vivo* regenerative medicine applications. We first showed that prior to implantation, patterned, perfusable vasculature has gene expression towards

vascular remodeling and development, making these tissues suitable for vascular integration after *in vivo* implantation. Further, the gene expression is minimally affected by incorporating additional layers of perfusable vasculature, suggesting that higher levels of tissue vascularization can be achieved without changing the gene expression of the vasculature. After implantation, the patterned, perfusable constructs largely remodel and incorporate with the host vasculature more extensively at an early timepoint than non-perfusable tissues with self-assembled vasculature. This finding aligns with our previous study using constructs with single layer planar perfusable vasculature[126]. While we expected to see a more robust difference between multilayer microvessels and self-assembled constructs due to the additional perfusable vasculature, it is important to note that these tissues are thicker than the tissues in our previous study and we did see perfusable vasculature through the entire depth of the 1.5 mm thick constructs. Despite these beneficial effects, further tissue modifications, such as increasing bulk endothelial cell concentration or addition of stromal cells, may be necessary to achieve more drastic vascular integration between the implanted tissue and the host.

In our studies, we utilized a simple vasculature structure, however, our platform can be used to create vasculature with much higher complexity. For our microvessels, we selected a planar network geometry of a 13 x 13 grid with 100 μm feature height to create all patterned lumens. We generated collagen membranes that were 190 μm thick and chose to stack 4 layers of vasculature as a proof-of-concept for our assembly method. While these selected parameters demonstrated the ability to generate highly vascularized tissues using this approach, these parameters are easily tunable towards generation of larger tissues or more complex vasculature. First, larger tissues can be achieved without

loss of vascular density by simply adding additional patterned collagen membranes. Here, we fabricated tissues with 8 layers of perfusable vasculature, with consistent vascularization throughout a 6 mm x 6 mm x 1.5 mm volume. Additionally, separation of lumens in the z-direction can be altered by using thinner or thicker membranes. In fact, in a previous study, we utilized a similar collagen membrane platform and achieved unpatterned membranes with a thickness of only 30 μm[209]. Lumen separation in the xy-plane, vessel diameter, and planar morphology of the vasculature can all be modified by using a different geometry to pattern all the lumens. Further, additional modification towards vasculature complexity, such as patterning of capillary-sized vessels, could be added through collagen ablation[210].

In this study, we sought to demonstrate the feasibility of constructing large-scale, perfusable tissues from collagen using a modular approach where components are individually generated then assembled together. While the field of tissue vascularization has largely moved away from modular assembly, this is not the first such study to use this approach. In an experiment by Sekine et al., cell sheets containing endothelial cells were stacked three at a time onto a vascular bed and became perfusable after vascular remodeling[115]. However, this method required days between application of subsequent layers because the layers were not perfusable at the time of fabrication. In another study, Zhang et al. stacked perfusable biodegradable scaffolds that were generated via lithography[117]. Although these tissues were immediately perfusable and able to survive direct anastomosis *in vivo*, their choice in scaffold material limited the interactions between the vasculature and parenchymal cells. Collagen-based tissues are more ideal for tissue engineering applications due to their ability to maintain vascular structure while

facilitating remodeling of parenchymal cells embedded within the collagen matrix[211]. Yet, collagen-based approaches for generating perfusable vasculature have focused on using only one gelation step. Here, we show that collagen-based tissues can be individually gelled then assembled to create a larger tissue with perfusable vasculature.

Modular assembly has the potential to overcome previous hurdles in creation of large-scale, complex tissues. By breaking the tissue into small pieces, precision can be achieved in the fabrication of small-scale features, such as small diameter vessels. Tissue heterogeneity will also be more feasible as individual components could have different cellular or matrix composition. Additionally, modular assembly is likely beneficial for tissue survival during fabrication because there are no long periods where cells within the bulk matrix are not near a nutrient source. With modular assembly, individual components can be thin, so diffusion can provide nutrients through each component before components are brought together. Then, after a brief assembly process, tissues will be immediately perfusable through their patterned vasculature. Application of this modular assembly approach is not limited to use with soft lithography-based fabrication techniques as we used here and could be used in combination with other techniques like 3D printing to achieve superior vascularization of engineered tissues.

Overall, we successfully fabricated highly vascularized, perfusable, large-scale tissues using a soft lithography and collagen membrane stacking approach. This work lays the foundation for using modular assembly to generate highly metabolic, thick engineered tissues with the support of extensive vascularization and will facilitate previously unachieved complexity and scale in tissue engineering.

Chapter 6. Summary and Future Directions

Vascularization and adequate perfusion are critical components of living systems that are larger than millimeter scale. Inadequate perfusion of the heart during a myocardial infarction, results in massive tissue death and remodeling. Similarly *in vitro*, perfusable vasculature is necessary for the survival of large-scale engineered tissues. The above work established tools for assessing vascular perfusion and for generating dense perfusable vasculature within engineered tissues, with a focus on cardiac regeneration. In Chapter 3, optical coherence tomography-based imaging systems and processing frameworks were utilized to quantitatively compare the vascular morphology, perfusion dynamics, and fiber orientation of healthy and infarcted *ex vivo* fixed rat hearts during retrograde perfusion. In Chapter 4, cardiac tissues with perfusable microvessels in planar geometry were shown to have better host vascular integration after implantation onto infarcted rat hearts than non-perfusable, self-assembled controls. In Chapter 5, a novel method for generating thick tissues with dense, three-dimensional, perfusable vasculature was established. Together, the findings of this work can be used to facilitate the generation of large-scale implantable tissues for cardiac repair.

As this work focused on establishing technology platforms in two areas, imaging and tissue vascularization, further advances could be made in both areas. On the imaging side, we have demonstrated that optical coherence tomography (OCT)-based imaging is ideal for noninvasive assessment of intact hearts. However, we are currently limited to imaging hearts that are arrested and fixed, restricting our ability to get information about the dynamics processes during the cardiac cycle. It would therefore be highly informative to create gating and motion stabilizing algorithms that enable imaging of beating hearts.

Such algorithms would allow for assessment of perfusion and fiber orientation changes during contraction in both healthy and infarcted tissue. Additionally, the ability to image live hearts could allow for repeated imaging of the same animal over time, which could enable assessment of a continuous healing process, yet this approach may be limited by the need for repeated thoracotomies to image the heart. Another potential improvement would be to combine the imaging systems to provide both vascular and structural information from the same scans. As polarization sensitive OCT can discern between cardiomyocytes and collagenous scar through differing optical properties of the refracted light, it would be very interesting to apply such a system to visualize perfusion and fiber orientation of cardiomyocyte grafts after cell injection.

In regards to tissue vascularization, the most apparent next step would be to create thick, highly vascularized cardiac tissues using our multilayer stacking approach from Chapter 5. The work in this dissertation demonstrates that electrically coupled cardiac tissues can be fabricated using our microvessel platform with planar geometry microvessels, therefore, it would be an easy leap to make cardiac tissues with multilayer microvessels. This approach could improve the survival of cardiomyocytes within the core of the tissue and allow for generation of the thickest cardiac tissues to date. Further, it would be interesting to assess how perfusable vasculature effects cardiomyocyte maturation and tissue function *in vitro*. If superior maturation is demonstrated, this could lead to a new platform for cardiac disease modeling and drug development. As a follow up to our single layer cardiac tissue and multilayer vascular tissue implantation studies, implantation of highly vascularized, highly cellularized cardiac tissues would provide information about how perfusable patterning might benefit host vascular integration and

cardiomyocyte engraftment of thick cardiac tissue. Such a study could combine OCT-based imaging and tissue vascularization techniques developed throughout this dissertation and could address critical challenges in the application of cardiac patches for cardiac repair.

While data in this dissertation demonstrates that perfusable patterning results in increased host vascular integration of tissues implanted on the surface of the heart at early timepoints, this vascularization may not be sufficient to fully support cardiomyocyte engraftment and health within a cardiac patch. Therefore, it would be beneficial to directly anastomose the implanted tissue to the host vasculature to immediately provide blood flow to cardiac patches. It may be possible to do this through means similar to coronary bypass surgery. Although further investigation of microvessel burst pressure would be necessary, our approach to generating large, highly vascularized, perfusable tissues could be suitable for such an application, potentially increasing the therapeutic potential of cardiac patches.

References

1. Eisner, D. A., Caldwell, J. L., Kistamás, K. & Trafford, A. W. Calcium and Excitation-Contraction Coupling in the Heart. *Circ Res* **121**, 181–195 (2017).

2. Gillum, R. F. Epidemiology of resting pulse rate of persons ages 25-74--data from NHANES 1971-74. *Public Health Rep* **107**, 193–201.

3. Wang, Z. *et al.* Specific metabolic rates of major organs and tissues across adulthood: evaluation by mechanistic model of resting energy expenditure. *Am J Clin Nutr* **92**, 1369–77 (2010).

4. Reese, D. E., Mikawa, T. & Bader, D. M. Development of the coronary vessel system. *Circ Res* **91**, 761–8 (2002).

5. Hsieh, P. C. H., Davis, M. E., Lisowski, L. K. & Lee, R. T. Endothelial-cardiomyocyte interactions in cardiac development and repair. *Annu Rev Physiol* **68**, 51–66 (2006).

6. Homan, T. D., Bordes, S. & Cichowski, E. *Physiology, Pulse Pressure*. (2022).

7. Tansey, E. A., Montgomery, L. E. A., Quinn, J. G., Roe, S. M. & Johnson, C. D. Understanding basic vein physiology and venous blood pressure through simple physical assessments. *Adv Physiol Educ* **43**, 423–429 (2019).

8. Armentano, R. L. , L. J. C. Damping in the vascular wall. in *Biomechanical Modeling of the Cardiovascular System* 1–23 (2019).

9. Huo, Y. & Kassab, G. S. Pulsatile blood flow in the entire coronary arterial tree: theory and experiment. *Am J Physiol Heart Circ Physiol* **291**, H1074-87 (2006).

10. Ramanathan, T. S. H. Cononary blood flow. *Continuing Education in Anaesthesia Critical Care & Pain* **5**, 61–64 (2005).

11. Talman, V. & Kivelä, R. Cardiomyocyte-Endothelial Cell Interactions in Cardiac Remodeling and Regeneration. *Front Cardiovasc Med* **5**, 101 (2018).

12. Vestweber, D. VE-cadherin: the major endothelial adhesion molecule controlling cellular junctions and blood vessel formation. *Arterioscler Thromb Vasc Biol* **28**, 223–32 (2008).

13. Sandoo, A., van Zanten, J. J. C. S. V., Metsios, G. S., Carroll, D. & Kitas, G. D. The endothelium and its role in regulating vascular tone. *Open Cardiovasc Med J* **4**, 302–12 (2010).

14. Pober, J. S. & Sessa, W. C. Evolving functions of endothelial cells in inflammation. *Nat Rev Immunol* **7**, 803–15 (2007).

15. Lepic, E., Burger, D., Lu, X., Song, W. & Feng, Q. Lack of endothelial nitric oxide synthase decreases cardiomyocyte proliferation and delays cardiac maturation. *Am J Physiol Cell Physiol* **291**, C1240-6 (2006).

16. Zhao, Y. Y. *et al.* Neuregulins promote survival and growth of cardiac myocytes. Persistence of ErbB2 and ErbB4 expression in neonatal and adult ventricular myocytes. *J Biol Chem* **273**, 10261–9 (1998).

17. Hoch, R. v & Soriano, P. Roles of PDGF in animal development. *Development* **130**, 4769–84 (2003).

18. Krämer, B. K., Smith, T. W. & Kelly, R. A. Endothelin and increased contractility in adult rat ventricular myocytes. Role of intracellular alkalosis induced by activation of the protein kinase C-dependent Na(+)-H+ exchanger. *Circ Res* **68**, 269–79 (1991).

19. Vantler, M. *et al.* PDGF-BB protects cardiomyocytes from apoptosis and improves contractile function of engineered heart tissue. *J Mol Cell Cardiol* **48**, 1316–23 (2010).

20. Tomanek, R. J. Developmental Progression of the Coronary Vasculature in Human Embryos and Fetuses. *Anat Rec (Hoboken)* **299**, 25–41 (2016).

21. Dyer, L., Pi, X. & Patterson, C. Connecting the coronaries: how the coronary plexus develops and is functionalized. *Dev Biol* **395**, 111–9 (2014).

22. Cai, C.-L. *et al.* A myocardial lineage derives from Tbx18 epicardial cells. *Nature* **454**, 104–8 (2008).

23. Acharya, A., Baek, S. T., Banfi, S., Eskiocak, B. & Tallquist, M. D. Efficient inducible Cre-mediated recombination in Tcf21 cell lineages in the heart and kidney. *Genesis* **49**, 870–7 (2011).

24. Red-Horse, K., Ueno, H., Weissman, I. L. & Krasnow, M. A. Coronary arteries form by developmental reprogramming of venous cells. *Nature* **464**, 549–53 (2010).

25. Zhang, H. *et al.* Endocardium Minimally Contributes to Coronary Endothelium in the Embryonic Ventricular Free Walls. *Circ Res* **118**, 1880–93 (2016).

26. Wu, B. *et al.* Endocardial cells form the coronary arteries by angiogenesis through myocardial-endocardial VEGF signaling. *Cell* **151**, 1083–96 (2012).

27. Tian, X. *et al.* Vessel formation. De novo formation of a distinct coronary vascular population in neonatal heart. *Science* **345**, 90–4 (2014).

28. Bogers, A. J., Gittenberger-de Groot, A. C., Poelmann, R. E., Péault, B. M. & Huysmans, H. A. Development of the origin of the coronary arteries, a matter of ingrowth or outgrowth? *Anat Embryol (Berl)* **180**, 437–41 (1989).

29. Aghajanian, H. *et al.* Coronary vasculature patterning requires a novel endothelial ErbB2 holoreceptor. *Nat Commun* **7**, 12038 (2016).

30. Su, T. *et al.* Single-cell analysis of early progenitor cells that build coronary arteries. *Nature* **559**, 356–362 (2018).

31. Chang, A. H. *et al.* DACH1 stimulates shear stress-guided endothelial cell migration and coronary artery growth through the CXCL12-CXCR4 signaling axis. *Genes Dev* **31**, 1308–1324 (2017).

32. Virani, S. S. *et al.* Heart Disease and Stroke Statistics-2021 Update: A Report From the American Heart Association. *Circulation* **143**, e254–e743 (2021).

33. Centers for Disease Control and Prevention, N. C. for H. Statistics. *Multiple cause of death, 1999-2020.* (2020).

34. Palasubramaniam, J., Wang, X. & Peter, K. Myocardial Infarction-From Atherosclerosis to Thrombosis. *Arterioscler Thromb Vasc Biol* **39**, e176–e185 (2019).

35. Laflamme, M. A. & Murry, C. E. Heart regeneration. *Nature* **473**, 326–35 (2011).

36. Murry, C. E., Reinecke, H. & Pabon, L. M. Regeneration gaps: observations on stem cells and cardiac repair. *J Am Coll Cardiol* **47**, 1777–85 (2006).

37. Lázár, E., Sadek, H. A. & Bergmann, O. Cardiomyocyte renewal in the human heart: insights from the fall-out. *Eur Heart J* **38**, 2333–2342 (2017).

38. Sutton, M. G. & Sharpe, N. Left ventricular remodeling after myocardial infarction: pathophysiology and therapy. *Circulation* **101**, 2981–8 (2000).

39. Virag, J. I. & Murry, C. E. Myofibroblast and endothelial cell proliferation during murine myocardial infarct repair. *Am J Pathol* **163**, 2433–40 (2003).

40. Bahit, M. C., Kochar, A. & Granger, C. B. Post-Myocardial Infarction Heart Failure. *JACC Heart Fail* **6**, 179–186 (2018).

41. Konijnenberg, L. S. F. *et al.* Pathophysiology and diagnosis of coronary microvascular dysfunction in ST-elevation myocardial infarction. *Cardiovasc Res* **116**, 787–805 (2020).

42. Jürgensen, J. S. *et al.* Persistent induction of HIF-1alpha and -2alpha in cardiomyocytes and stromal cells of ischemic myocardium. *FASEB J* **18**, 1415–7 (2004).

43. Lee, S. H. *et al.* Early expression of angiogenesis factors in acute myocardial ischemia and infarction. *N Engl J Med* **342**, 626–33 (2000).

44. Frangogiannis, N. G. The inflammatory response in myocardial injury, repair, and remodelling. *Nat Rev Cardiol* **11**, 255–65 (2014).

45. Zhang, M. *et al.* CXCL12 enhances angiogenesis through CXCR7 activation in human umbilical vein endothelial cells. *Sci Rep* **7**, 8289 (2017).

46. Dubé, K. N. *et al.* Recapitulation of developmental mechanisms to revascularize the ischemic heart. *JCI Insight* **2**, (2017).

47. He, L. *et al.* Preexisting endothelial cells mediate cardiac neovascularization after injury. *J Clin Invest* **127**, 2968–2981 (2017).

48. Mouton, A. J. *et al.* Fibroblast polarization over the myocardial infarction time continuum shifts roles from inflammation to angiogenesis. *Basic Res Cardiol* **114**, 6 (2019).

49. White, P. D., Mallory, G. K. & Salcedo-Salgar, J. The Speed of Healing of Myocardial Infarcts. *Trans Am Clin Climatol Assoc* **52**, 97-104.1 (1936).

50. Han, H.-C. Twisted blood vessels: symptoms, etiology and biomechanical mechanisms. *J Vasc Res* **49**, 185–97 (2012).

51. Yanagisawa-Miwa, A. *et al.* Salvage of infarcted myocardium by angiogenic action of basic fibroblast growth factor. *Science* **257**, 1401–3 (1992).

52. Wang, B., Cheheltani, R., Rosano, J., Crabbe, D. L. & Kiani, M. F. Targeted delivery of VEGF to treat myocardial infarction. *Adv Exp Med Biol* **765**, 307–314 (2013).

53. Weinberger, F. & Eschenhagen, T. Cardiac Regeneration: New Hope for an Old Dream. *Annu Rev Physiol* **83**, 59–81 (2021).

54. Cheng, R. K. *et al.* Cyclin A2 induces cardiac regeneration after myocardial infarction and prevents heart failure. *Circ Res* **100**, 1741–8 (2007).

55. Heallen, T. *et al.* Hippo pathway inhibits Wnt signaling to restrain cardiomyocyte proliferation and heart size. *Science* **332**, 458–61 (2011).

56. Gabisonia, K. *et al.* MicroRNA therapy stimulates uncontrolled cardiac repair after myocardial infarction in pigs. *Nature* **569**, 418–422 (2019).

57. Shapiro, S. D. *et al.* Cyclin A2 induces cardiac regeneration after myocardial infarction through cytokinesis of adult cardiomyocytes. *Sci Transl Med* **6**, 224ra27 (2014).

58. Ieda, M. *et al.* Direct reprogramming of fibroblasts into functional cardiomyocytes by defined factors. *Cell* **142**, 375–86 (2010).

59. Doeser, M. C., Schöler, H. R. & Wu, G. Reduction of Fibrosis and Scar Formation by Partial Reprogramming In Vivo. *Stem Cells* **36**, 1216–1225 (2018).

60. Mahmoudi, S. *et al.* Heterogeneity in old fibroblasts is linked to variability in reprogramming and wound healing. *Nature* **574**, 553–558 (2019).

61. Liu, B. *et al.* Cardiac recovery via extended cell-free delivery of extracellular vesicles secreted by cardiomyocytes derived from induced pluripotent stem cells. *Nat Biomed Eng* **2**, 293–303 (2018).

62. Gallet, R. *et al.* Exosomes secreted by cardiosphere-derived cells reduce scarring, attenuate adverse remodelling, and improve function in acute and chronic porcine myocardial infarction. *Eur Heart J* **38**, 201–211 (2017).

63. Ibrahim, A. G.-E., Cheng, K. & Marbán, E. Exosomes as critical agents of cardiac regeneration triggered by cell therapy. *Stem Cell Reports* **2**, 606–19 (2014).

64. Gyöngyösi, M. *et al.* NOGA-guided analysis of regional myocardial perfusion abnormalities treated with intramyocardial injections of plasmid encoding vascular endothelial growth factor A-165 in patients with chronic myocardial ischemia: subanalysis of the EUROINJECT-ONE multicenter double-blind randomized study. *Circulation* **112**, I157-65 (2005).

65. Simons, M. *et al.* Pharmacological treatment of coronary artery disease with recombinant fibroblast growth factor-2: double-blind, randomized, controlled clinical trial. *Circulation* **105**, 788–93 (2002).

66. Bar, A. & Cohen, S. Inducing Endogenous Cardiac Regeneration: Can Biomaterials Connect the Dots? *Front Bioeng Biotechnol* **8**, 126 (2020).

67. Vagnozzi, R. J. *et al.* An acute immune response underlies the benefit of cardiac stem cell therapy. *Nature* **577**, 405–409 (2020).

68. Hashimoto, H., Olson, E. N. & Bassel-Duby, R. Therapeutic approaches for cardiac regeneration and repair. *Nat Rev Cardiol* **15**, 585–600 (2018).

69. Le, T. & Chong, J. Cardiac progenitor cells for heart repair. *Cell Death Discov* **2**, 16052 (2016).

70. Cheng, Y., Jiang, S., Hu, R. & Lv, L. Potential mechanism for endothelial progenitor cell therapy in acute myocardial infarction: Activation of VEGF- PI3K/Akte-NOS pathway. *Ann Clin Lab Sci* **43**, 395–401 (2013).

71. Takahashi, K. & Yamanaka, S. Induction of pluripotent stem cells from mouse embryonic and adult fibroblast cultures by defined factors. *Cell* **126**, 663–76 (2006).

72. Burridge, P. W. *et al.* Chemically defined generation of human cardiomyocytes. *Nat Methods* **11**, 855–60 (2014).

73. Palpant, N. J. *et al.* Generating high-purity cardiac and endothelial derivatives from patterned mesoderm using human pluripotent stem cells. *Nat Protoc* **12**, 15–31 (2017).

74. Palpant, N. J. *et al.* Inhibition of β-catenin signaling respecifies anterior-like endothelium into beating human cardiomyocytes. *Development* **142**, 3198–209 (2015).

75. Zhao, J. *et al.* Efficient Differentiation of TBX18+/WT1+ Epicardial-Like Cells from Human Pluripotent Stem Cells Using Small Molecular Compounds. *Stem Cells Dev* **26**, 528–540 (2017).

76. Bao, X. *et al.* Directed differentiation and long-term maintenance of epicardial cells derived from human pluripotent stem cells under fully defined conditions. *Nat Protoc* **12**, 1890–1900 (2017).

77. Iyer, D. *et al.* Robust derivation of epicardium and its differentiated smooth muscle cell progeny from human pluripotent stem cells. *Development* **142**, 1528–41 (2015).

78. Liao, Y., Zhu, L. & Wang, Y. Maturation of Stem Cell-Derived Cardiomyocytes: Foe in Translation Medicine. *Int J Stem Cells* **14**, 366–385 (2021).

79. Deuse, T. *et al.* Hypoimmunogenic derivatives of induced pluripotent stem cells evade immune rejection in fully immunocompetent allogeneic recipients. *Nat Biotechnol* **37**, 252–258 (2019).

80. Chong, J. J. H. *et al.* Human embryonic-stem-cell-derived cardiomyocytes regenerate non-human primate hearts. *Nature* **510**, 273–7 (2014).

81. Liu, Y.-W. *et al.* Human embryonic stem cell-derived cardiomyocytes restore function in infarcted hearts of non-human primates. *Nat Biotechnol* **36**, 597–605 (2018).

82. Silver, S. E., Barrs, R. W. & Mei, Y. Transplantation of Human Pluripotent Stem Cell-Derived Cardiomyocytes for Cardiac Regenerative Therapy. *Front Cardiovasc Med* **8**, 707890 (2021).

83. Gao, L. *et al.* Large Cardiac Muscle Patches Engineered From Human Induced-Pluripotent Stem Cell-Derived Cardiac Cells Improve Recovery From Myocardial Infarction in Swine. *Circulation* **137**, 1712–1730 (2018).

84. Tenreiro, M. F., Louro, A. F., Alves, P. M. & Serra, M. Next generation of heart regenerative therapies: progress and promise of cardiac tissue engineering. *NPJ Regen Med* **6**, 30 (2021).

85. Reis, L. A., Chiu, L. L. Y., Feric, N., Fu, L. & Radisic, M. Biomaterials in myocardial tissue engineering. *J Tissue Eng Regen Med* **10**, 11–28 (2016).

86. Zimmermann, W. H. *et al.* Three-dimensional engineered heart tissue from neonatal rat cardiac myocytes. *Biotechnol Bioeng* **68**, 106–14 (2000).

87. Ronaldson-Bouchard, K. *et al.* Advanced maturation of human cardiac tissue grown from pluripotent stem cells. *Nature* **556**, 239–243 (2018).

88. Bielawski, K. S., Leonard, A., Bhandari, S., Murry, C. E. & Sniadecki, N. J. Real-Time Force and Frequency Analysis of Engineered Human Heart Tissue Derived from Induced Pluripotent Stem Cells Using Magnetic Sensing. *Tissue Eng Part C Methods* **22**, 932–940 (2016).

89. Ramade, A., Legant, W. R., Picart, C., Chen, C. S. & Boudou, T. Microfabrication of a platform to measure and manipulate the mechanics of engineered microtissues. *Methods Cell Biol* **121**, 191–211 (2014).

90. Lemoine, M. D. *et al.* Human iPSC-derived cardiomyocytes cultured in 3D engineered heart tissue show physiological upstroke velocity and sodium current density. *Sci Rep* **7**, 5464 (2017).

91. Correia, C. *et al.* 3D aggregate culture improves metabolic maturation of human pluripotent stem cell derived cardiomyocytes. *Biotechnol Bioeng* **115**, 630–644 (2018).

92. Richards, D. J. *et al.* Nanowires and Electrical Stimulation Synergistically Improve Functions of hiPSC Cardiac Spheroids. *Nano Lett* **16**, 4670–8 (2016).

93. Godier-Furnémont, A. F. G. *et al.* Physiologic force-frequency response in engineered heart muscle by electromechanical stimulation. *Biomaterials* **60**, 82–91 (2015).

94. Leonard, A. *et al.* Afterload promotes maturation of human induced pluripotent stem cell derived cardiomyocytes in engineered heart tissues. *J Mol Cell Cardiol* **118**, 147–158 (2018).

95. Li, R. K. *et al.* Survival and function of bioengineered cardiac grafts. *Circulation* **100**, II63-9 (1999).

96. Stevens, K. R., Pabon, L., Muskheli, V. & Murry, C. E. Scaffold-free human cardiac tissue patch created from embryonic stem cells. *Tissue Eng Part A* **15**, 1211–22 (2009).

97. Stevens, K. R. *et al.* Physiological function and transplantation of scaffold-free and vascularized human cardiac muscle tissue. *Proc Natl Acad Sci U S A* **106**, 16568–73 (2009).

98. Jackman, C. P. *et al.* Engineered cardiac tissue patch maintains structural and electrical properties after epicardial implantation. *Biomaterials* **159**, 48–58 (2018).

99. Shadrin, I. Y. *et al.* Cardiopatch platform enables maturation and scale-up of human pluripotent stem cell-derived engineered heart tissues. *Nat Commun* **8**, 1825 (2017).

100. Gerbin, K. A., Yang, X., Murry, C. E. & Coulombe, K. L. K. Enhanced Electrical Integration of Engineered Human Myocardium via Intramyocardial versus Epicardial Delivery in Infarcted Rat Hearts. *PLoS One* **10**, e0131446 (2015).

101. Lovett, M., Lee, K., Edwards, A. & Kaplan, D. L. Vascularization strategies for tissue engineering. *Tissue Eng Part B Rev* **15**, 353–70 (2009).

102. Tulloch, N. L. *et al.* Growth of engineered human myocardium with mechanical loading and vascular coculture. *Circ Res* **109**, 47–59 (2011).

103. Sekine, H. *et al.* Endothelial cell coculture within tissue-engineered cardiomyocyte sheets enhances neovascularization and improves cardiac function of ischemic hearts. *Circulation* **118**, S145-52 (2008).

104. Giacomelli, E. *et al.* Human-iPSC-Derived Cardiac Stromal Cells Enhance Maturation in 3D Cardiac Microtissues and Reveal Non-cardiomyocyte Contributions to Heart Disease. *Cell Stem Cell* **26**, 862-879.e11 (2020).

105. Garzoni, L. R. *et al.* Dissecting coronary angiogenesis: 3D co-culture of cardiomyocytes with endothelial or mesenchymal cells. *Exp Cell Res* **315**, 3406–18 (2009).

106. Coulombe, K. L. K. & Murry, C. E. Vascular Perfusion of Implanted Human Engineered Cardiac Tissue. *Proc IEEE Annu Northeast Bioeng Conf* **2014**, (2014).

107. Baranski, J. D. *et al.* Geometric control of vascular networks to enhance engineered tissue integration and function. *Proc Natl Acad Sci U S A* **110**, 7586–91 (2013).

108. Brady, E. L. *et al.* Guided vascularization in the rat heart leads to transient vessel patterning. *APL Bioeng* **4**, 016105 (2020).

109. Dvir, T. *et al.* Prevascularization of cardiac patch on the omentum improves its therapeutic outcome. *Proc Natl Acad Sci U S A* **106**, 14990–5 (2009).

110. Ben-Shaul, S., Landau, S., Merdler, U. & Levenberg, S. Mature vessel networks in engineered tissue promote graft-host anastomosis and prevent graft thrombosis. *Proc Natl Acad Sci U S A* **116**, 2955–2960 (2019).

111. Nguyen, D.-H. T. *et al.* Biomimetic model to reconstitute angiogenic sprouting morphogenesis in vitro. *Proc Natl Acad Sci U S A* **110**, 6712–7 (2013).

112. Chung, S. *et al.* Cell migration into scaffolds under co-culture conditions in a microfluidic platform. *Lab Chip* **9**, 269–75 (2009).

113. Hsu, Y.-H., Moya, M. L., Hughes, C. C. W., George, S. C. & Lee, A. P. A microfluidic platform for generating large-scale nearly identical human microphysiological vascularized tissue arrays. *Lab Chip* **13**, 2990–8 (2013).

114. Moya, M., Tran, D. & George, S. C. An integrated in vitro model of perfused tumor and cardiac tissue. *Stem Cell Res Ther* **4 Suppl 1**, S15 (2013).

115. Sekine, H. *et al.* In vitro fabrication of functional three-dimensional tissues with perfusable blood vessels. *Nat Commun* **4**, 1399 (2013).

116. Vollert, I. *et al.* In vitro perfusion of engineered heart tissue through endothelialized channels. *Tissue Eng Part A* **20**, 854–63 (2014).

117. Zhang, B. *et al.* Biodegradable scaffold with built-in vasculature for organ-on-a-chip engineering and direct surgical anastomosis. *Nat Mater* **15**, 669–78 (2016).

118. Skylar-Scott, M. A. *et al.* Biomanufacturing of organ-specific tissues with high cellular density and embedded vascular channels. *Sci Adv* **5**, eaaw2459 (2019).

119. Lee, A. *et al.* 3D bioprinting of collagen to rebuild components of the human heart. *Science* **365**, 482–487 (2019).

120. Grigoryan, B. *et al.* Multivascular networks and functional intravascular topologies within biocompatible hydrogels. *Science* **364**, 458–464 (2019).

121. Kinstlinger, I. S. *et al.* Generation of model tissues with dendritic vascular networks via sacrificial laser-sintered carbohydrate templates. *Nat Biomed Eng* **4**, 916–932 (2020).

122. Hann, S. Y. *et al.* Recent advances in 3D printing: vascular network for tissue and organ regeneration. *Transl Res* **211**, 46–63 (2019).

123. Roberts, M. A., Kotha, S. S., Phong, K. T. & Zheng, Y. Micropatterning and Assembly of 3D Microvessels. *J Vis Exp* (2016) doi:10.3791/54457.

124. Zheng, Y. *et al.* In vitro microvessels for the study of angiogenesis and thrombosis. *Proc Natl Acad Sci U S A* **109**, 9342–7 (2012).

125. Roberts, M. A. *et al.* Stromal Cells in Dense Collagen Promote Cardiomyocyte and Microvascular Patterning in Engineered Human Heart Tissue. *Tissue Eng Part A* **22**, 633–44 (2016).

126. Redd, M. A. *et al.* Patterned human microvascular grafts enable rapid vascularization and increase perfusion in infarcted rat hearts. *Nat Commun* **10**, 584 (2019).

127. Majmudar, M. D. & Nahrendorf, M. Cardiovascular molecular imaging: the road ahead. *J Nucl Med* **53**, 673–6 (2012).

128. Dobrucki, L. W. & Sinusas, A. J. PET and SPECT in cardiovascular molecular imaging. *Nat Rev Cardiol* **7**, 38–47 (2010).

129. Nehrhoff, I. *et al.* 3D imaging in CUBIC-cleared mouse heart tissue: going deeper. *Biomed Opt Express* **7**, 3716–3720 (2016).

130. Das, S. *et al.* A Unique Collateral Artery Development Program Promotes Neonatal Heart Regeneration. *Cell* **176**, 1128-1142.e18 (2019).

131. Merz, S. F. *et al.* Contemporaneous 3D characterization of acute and chronic myocardial I/R injury and response. *Nat Commun* **10**, 2312 (2019).

132. Wu, J. J. N. T. K. Speed scaling in multiphoton fluorescence microscopy. *Nature Photonics* **15**, 800–812 (2021).

133. Matsuura, R., Miyagawa, S., Kikuta, J., Ishii, M. & Sawa, Y. Intravital Imaging of the Heart at the Cellular Level Using Two-Photon Microscopy. *Methods Mol Biol* **1763**, 145–151 (2018).

134. Wang, R. K. *et al.* Three dimensional optical angiography. *Opt Express* **15**, 4083–97 (2007).

135. Zhang, Q., Wang, J. & Wang, R. K. Highly efficient eigen decomposition based statistical optical microangiography. *Quant Imaging Med Surg* **6**, 557–563 (2016).

136. An, L. & Wang, R. K. In vivo volumetric imaging of vascular perfusion within human retina and choroids with optical micro-angiography. *Opt Express* **16**, 11438–52 (2008).

137. Zhi, Z., Jung, Y., Jia, Y., An, L. & Wang, R. K. Highly sensitive imaging of renal microcirculation in vivo using ultrahigh sensitive optical microangiography. *Biomed Opt Express* **2**, 1059–68 (2011).

138. Wojtkowski, M. *et al.* Ultrahigh-resolution, high-speed, Fourier domain optical coherence tomography and methods for dispersion compensation. *Opt Express* **12**, 2404–22 (2004).

139. Song, S., Xu, J. & Wang, R. K. Long-range and wide field of view optical coherence tomography for in vivo 3D imaging of large volume object based on akinetic programmable swept source. *Biomed Opt Express* **7**, 4734–4748 (2016).

140. Xu, J., Wei, W., Song, S., Qi, X. & Wang, R. K. Scalable wide-field optical coherence tomography-based angiography for in vivo imaging applications. *Biomed Opt Express* **7**, 1905–19 (2016).

141. Baran, U., Qin, W., Qi, X., Kalkan, G. & Wang, R. K. OCT-based label-free in vivo lymphangiography within human skin and areola. *Sci Rep* **6**, 21122 (2016).

142. An, L., Qin, J. & Wang, R. K. Ultrahigh sensitive optical microangiography for in vivo imaging of microcirculations within human skin tissue beds. *Opt Express* **18**, 8220–8 (2010).

143. Yousefi, S., Qin, J. & Wang, R. K. Super-resolution spectral estimation of optical micro-angiography for quantifying blood flow within microcirculatory tissue beds in vivo. *Biomed Opt Express* **4**, 1214–28 (2013).

144. Wang, R. K. Optical Microangiography: A Label Free 3D Imaging Technology to Visualize and Quantify Blood Circulations within Tissue Beds in vivo. *IEEE J Sel Top Quantum Electron* **16**, 545–554 (2010).

145. Yousefi, S., Zhi, Z. & Wang, R. K. Eigendecomposition-based clutter filtering technique for optical micro-angiography. *IEEE Trans Biomed Eng* **58**, (2011).

146. Wang, R. K., Zhang, Q., Li, Y. & Song, S. Optical coherence tomography angiography-based capillary velocimetry. *J Biomed Opt* **22**, 66008 (2017).

147. Qin, W. *et al.* Depth-resolved 3D visualization of coronary microvasculature with optical microangiography. *Phys Med Biol* **61**, 7536–7550 (2016).

148. Tang, P. *et al.* Polarization sensitive optical coherence tomography with single input for imaging depth-resolved collagen organizations. *Light Sci Appl* **10**, 237 (2021).

149. Fuster, V., Kelly, B. B. & Vedanthan, R. Global cardiovascular health: urgent need for an intersectoral approach. *J Am Coll Cardiol* **58**, 1208–10 (2011).

150. Mozaffarian, D. *et al.* Heart disease and stroke statistics--2015 update: a report from the American Heart Association. *Circulation* **131**, e29-322 (2015).

151. Wu, X., Reboll, M. R., Korf-Klingebiel, M. & Wollert, K. C. Angiogenesis after acute myocardial infarction. *Cardiovasc Res* **117**, 1257–1273 (2021).

152. Heusch, G. Myocardial ischaemia-reperfusion injury and cardioprotection in perspective. *Nat Rev Cardiol* **17**, 773–789 (2020).

153. Badimon, L. & Borrell, M. Microvasculature Recovery by Angiogenesis After Myocardial Infarction. *Curr Pharm Des* **24**, 2967–2973 (2018).

154. Gkontra, P. , Ż. M. M. , N. K. A. , S. A. , P. A. S. , & A. A. G. A 3D Fractal-Based Approach towards Understanding Changes in the Infarcted Heart Microvasculature. *International Conference on Medical Image Computing and Computer-Assisted Intervention* 173–180 (2015).

155. Gkontra, P. *et al.* Deciphering microvascular changes after myocardial infarction through 3D fully automated image analysis. *Sci Rep* **8**, 1854 (2018).

156. Bernucci, M. T., Merkle, C. W. & Srinivasan, V. J. Investigation of artifacts in retinal and choroidal OCT angiography with a contrast agent. *Biomed Opt Express* **9**, 1020–1040 (2018).

157. Baumann, B. *et al.* Swept source/Fourier domain polarization sensitive optical coherence tomography with a passive polarization delay unit. *Opt Express* **20**, 10229–41 (2012).

158. Li, E., Makita, S., Hong, Y.-J., Kasaragod, D. & Yasuno, Y. Three-dimensional multi-contrast imaging of in vivo human skin by Jones matrix optical coherence tomography. *Biomed Opt Express* **8**, 1290–1305 (2017).

159. Nam, A. S. *et al.* Wide-Field Functional Microscopy of Peripheral Nerve Injury and Regeneration. *Sci Rep* **8**, 14004 (2018).

160. Tuchin, V. v. Polarized light interaction with tissues. *J Biomed Opt* **21**, 71114 (2016).

161. Fan, C. & Yao, G. Imaging myocardial fiber orientation using polarization sensitive optical coherence tomography. *Biomed Opt Express* **4**, 460–5 (2013).

162. Li, Q., Sampson, D. D. & Villiger, M. In vivo imaging of the depth-resolved optic axis of birefringence in human skin. *Opt Lett* **45**, 4919–4922 (2020).

163. Walther, J. *et al.* Depth-resolved birefringence imaging of collagen fiber organization in the human oral mucosa in vivo. *Biomed Opt Express* **10**, 1942–1956 (2019).

164. Sakai, S., Yamanari, M., Lim, Y., Nakagawa, N. & Yasuno, Y. In vivo evaluation of human skin anisotropy by polarization-sensitive optical coherence tomography. *Biomed Opt Express* **2**, 2623–31 (2011).

165. Hervas, A. *et al.* Inhomogeneity of collagen organization within the fibrotic scar after myocardial infarction: results in a swine model and in human samples. *J Anat* **228**, 47–58 (2016).

166. Wang, R. K. , X. X. , T. V. V. , & E. J. B. Concurrent enhancement of imaging depth and contrast for optical coherence tomography by hyperosmotic agents. *JOSA B* **18**, 948–953 (2001).

167. Xu, X. & Wang, R. K. Synergistic effect of hyperosmotic agents of dimethyl sulfoxide and glycerol on optical clearing of gastric tissue studied with near infrared spectroscopy. *Phys Med Biol* **49**, 457–68 (2004).

168. Song, S., Xu, J., Men, S., Shen, T. T. & Wang, R. K. Robust numerical phase stabilization for long-range swept-source optical coherence tomography. *J Biophotonics* **10**, 1398–1410 (2017).

169. Yin, X., Chao, J. R. & Wang, R. K. User-guided segmentation for volumetric retinal optical coherence tomography images. *J Biomed Opt* **19**, 086020 (2014).

170. Zhang, Q. *et al.* Projection artifact removal improves visualization and quantitation of macular neovascularization imaged by optical coherence tomography angiography. *Ophthalmol Retina* **1**, 124–136.

171. Chu, Z. *et al.* Quantitative assessment of the retinal microvasculature using optical coherence tomography angiography. *J Biomed Opt* **21**, 66008 (2016).

172. Chen, C.-L. *et al.* Peripapillary Retinal Nerve Fiber Layer Vascular Microcirculation in Eyes With Glaucoma and Single-Hemifield Visual Field Loss. *JAMA Ophthalmol* **135**, 461–468 (2017).

173. Chen, C.-L. *et al.* Optic nerve head perfusion in normal eyes and eyes with glaucoma using optical coherence tomography-based microangiography. *Quant Imaging Med Surg* **6**, 125–33 (2016).

174. Longo, A. *et al.* Assessment of hessian-based Frangi vesselness filter in optoacoustic imaging. *Photoacoustics* **20**, 100200 (2020).

175. Li, Y. *et al.* Aging-associated changes in cerebral vasculature and blood flow as determined by quantitative optical coherence tomography angiography. *Neurobiol Aging* **70**, 148–159 (2018).

176. Watson, A. B. Perimetric complexity of binary digital images: Notes on calculation and relation to visual complexity. *The Mathematica Journal* **14**, (2011).

177. Furuhashi, Y. , K. Y. , & Y. H. Higher order structural analysis of stereocomplex-type poly (lactic acid) melt-spun fibers. *Journal of Polymer Science Part B: Polymer Physics* **45**, 218–228 (2007).

178. Ariga, R. *et al.* Identification of Myocardial Disarray in Patients With Hypertrophic Cardiomyopathy and Ventricular Arrhythmias. *J Am Coll Cardiol* **73**, 2493–2502 (2019).

179. Wang, Y. *et al.* Histology validation of mapping depth-resolved cardiac fiber orientation in fresh mouse heart using optical polarization tractography. *Biomed Opt Express* **5**, 2843–55 (2014).

180. Bullitt, E., Gerig, G., Pizer, S. M., Lin, W. & Aylward, S. R. Measuring tortuosity of the intracerebral vasculature from MRA images. *IEEE Trans Med Imaging* **22**, 1163–71 (2003).

181. MacNeil, S. Progress and opportunities for tissue-engineered skin. *Nature* **445**, 874–80 (2007).

182. Atala, A. Engineering organs. *Curr Opin Biotechnol* **20**, 575–92 (2009).

183. Atala, A., Kasper, F. K. & Mikos, A. G. Engineering complex tissues. *Sci Transl Med* **4**, 160rv12 (2012).

184. Ogle, B. M. *et al.* Distilling complexity to advance cardiac tissue engineering. *Sci Transl Med* **8**, 342ps13 (2016).

185. Laflamme, M. A. & Murry, C. E. Heart regeneration. *Nature* **473**, 326–35 (2011).

186. Coulombe, K. L. K. & Murry, C. E. Vascular Perfusion of Implanted Human Engineered Cardiac Tissue. *Proc IEEE Annu Northeast Bioeng Conf* **2014**, (2014).

187. Baiguera, S. & Ribatti, D. Endothelialization approaches for viable engineered tissues. *Angiogenesis* **16**, 1–14 (2013).

188. Montgomery, M., Zhang, B. & Radisic, M. Cardiac Tissue Vascularization: From Angiogenesis to Microfluidic Blood Vessels. *J Cardiovasc Pharmacol Ther* **19**, 382–393 (2014).

189. Shiba, Y. *et al.* Human ES-cell-derived cardiomyocytes electrically couple and suppress arrhythmias in injured hearts. *Nature* **489**, 322–5 (2012).

190. Gantz, J. A. *et al.* Targeted genomic integration of a selectable floxed dual fluorescence reporter in human embryonic stem cells. *PLoS One* **7**, e46971 (2012).

191. Laflamme, M. A. *et al.* Cardiomyocytes derived from human embryonic stem cells in pro-survival factors enhance function of infarcted rat hearts. *Nat Biotechnol* **25**, 1015–24 (2007).

192. Kim, D. *et al.* TopHat2: accurate alignment of transcriptomes in the presence of insertions, deletions and gene fusions. *Genome Biol* **14**, R36 (2013).

193. Anders, S., Pyl, P. T. & Huber, W. HTSeq--a Python framework to work with high-throughput sequencing data. *Bioinformatics* **31**, 166–9 (2015).

194. Robinson, M. D., McCarthy, D. J. & Smyth, G. K. edgeR: a Bioconductor package for differential expression analysis of digital gene expression data. *Bioinformatics* **26**, 139–40 (2010).

195. Liberzon, A. *et al.* The Molecular Signatures Database (MSigDB) hallmark gene set collection. *Cell Syst* **1**, 417–425 (2015).

196. Mackie, A. R. & Losordo, D. W. CD34-positive stem cells: in the treatment of heart and vascular disease in human beings. *Tex Heart Inst J* **38**, 474–85 (2011).

197. Zhang, M. *et al.* Cardiomyocyte grafting for cardiac repair: graft cell death and anti-death strategies. *J Mol Cell Cardiol* **33**, 907–21 (2001).

198. Asahara, T. *et al.* Isolation of putative progenitor endothelial cells for angiogenesis. *Science* **275**, 964–7 (1997).

199. Koffler, J. *et al.* Improved vascular organization enhances functional integration of engineered skeletal muscle grafts. *Proc Natl Acad Sci U S A* **108**, 14789–94 (2011).

200. Madden, L. R. *et al.* Proangiogenic scaffolds as functional templates for cardiac tissue engineering. *Proc Natl Acad Sci U S A* **107**, 15211–6 (2010).

201. Chiu, L. L. Y., Montgomery, M., Liang, Y., Liu, H. & Radisic, M. Perfusable branching microvessel bed for vascularization of engineered tissues. *Proc Natl Acad Sci U S A* **109**, E3414-23 (2012).

202. Juhas, M., Engelmayr, G. C., Fontanella, A. N., Palmer, G. M. & Bursac, N. Biomimetic engineered muscle with capacity for vascular integration and functional maturation in vivo. *Proc Natl Acad Sci U S A* **111**, 5508–13 (2014).

203. Ivanov, K. P., Kalinina, M. K. & Levkovich YuI. Blood flow velocity in capillaries of brain and muscles and its physiological significance. *Microvasc Res* **22**, 143–55 (1981).

204. Arfors, K. E., Bergqvist, D., Intaglietta, M. & Westergren, B. Measurements of blood flow velocity in the microcirculation. *Ups J Med Sci* **80**, 27–33 (1975).

205. Mandrycky, C., Phong, K. & Zheng, Y. Tissue engineering toward organ-specific regeneration and disease modeling. *MRS Commun* **7**, 332–347 (2017).

206. Shafiee, A. & Atala, A. Tissue Engineering: Toward a New Era of Medicine. *Annu Rev Med* **68**, 29–40 (2017).

207. Miller, J. S. *et al.* Rapid casting of patterned vascular networks for perfusable engineered three-dimensional tissues. *Nat Mater* **11**, 768–74 (2012).

208. Li, W., Germain, R. N. & Gerner, M. Y. High-dimensional cell-level analysis of tissues with Ce3D multiplex volume imaging. *Nat Protoc* **14**, 1708–1733 (2019).

209. Rayner, S. G. *et al.* Reconstructing the Human Renal Vascular-Tubular Unit In Vitro. *Adv Healthc Mater* **7**, e1801120 (2018).

210. Rayner, S. G. *et al.* Multiphoton-Guided Creation of Complex Organ-Specific Microvasculature. *Adv Healthc Mater* **10**, e2100031 (2021).

211. Liu, J., Zheng, H., Poh, P. S. P., Machens, H.-G. & Schilling, A. F. Hydrogels for Engineering of Perfusable Vascular Networks. *Int J Mol Sci* **16**, 15997–6016 (2015).